Solar RRL
www.solar-rrl.com

Next-Generation Solar-Powering: Photonic Strategies for Earth and Space Systems

Ivan M. Santos, Miguel Alexandre, António T. Vicente, Cristina Teixeira, Eva Almeida, Elvira Fortunato, Rodrigo Martins,* Hugo Águas, and Manuel J. Mendes*

Escalating environmental and energy supply concerns, coupled with an increasing interest in space exploration, are driving the development of advanced energy harvesting systems and the adoption of cutting-edge photovoltaic (PV) technologies. Photonics allows precise light manipulation in a multitude of ways, empowering PV with the means to tackle the multifaceted challenges inherent to the harsh space environment, with great potential to concomitantly spin off to on-Earth systems, prioritizing efficiency and reliability. This review thus synthesizes the key insights from the latest experimental and simulation R&D outcomes to inform the design and implementation of advanced photonic strategies for various PV applications. The state-of-the-art performance and foreground of photonic-managed thick- (single-junction crystalline silicon, c-Si, and perovskite-on-silicon tandem) and thin-film (hydrogenated amorphous silicon, a-Si:H, and perovskite) PV devices are assessed by comparison with theoretical ideal light-trapping scenarios (single-, double-pass, and Lambertian absorption models), looking also at the potential of photonic coolers as an emergent platform for effective thermal management. Finally, this work examines novel photonic approaches for spectrum modification, emphasizing the relevance of illumination-tailoring for outer space systems.

1. Introduction

The mature silicon-based photovoltaic (PV) technology serves as a pivotal driver for the ongoing expansion of the global PV market. In fact, crystalline silicon (c-Si) solar cells dominate the PV industry with a market share of ≈95%,[1] due to its unparalleled stability (already exceeding 3 decades), cost-effectiveness (currently <0.25 \$ Wp^{-1}),[2] and high efficiency (≈27%) nearing the Shockley–Queisser single-junction limit of ≈34%.[3] This technology is compatible with mass production at reduced costs and is usually coupled with classic photonic approaches via high-throughput chemical etching processes.[4] However, these harsh texturization processes, used for etching the top and bottom surfaces of c-Si slabs, undermine an optoelectronic trade-off between the optical enhancement and electrical performance deterioration.[5] The enhancement of optical performance stems from improved antireflection and light scattering, whereas the deterioration of the electrical performance is due to undesirable mechanisms linked to charged carrier trapping or recombination.

A persistent challenge in thin PV devices is to balance the carrier generation and collection. Essentially, thicker absorbers, required for light absorption and efficiency maximization counterbalance the benefits of thinner absorbers that mitigate bulk recombination and facilitate carrier collection.[6–8] Pioneering light trapping (LT) mechanisms play a pivotal role in compensating absorption losses for PV devices with reduced material thicknesses between 0.2 and 1 μm (e.g., thin-film hydrogenated amorphous silicon, a-Si:H, ultrathin c-Si, and perovskite solar cells, PSCs). The present review delves into effective LT strategies capable of substantially enhancing the performance of such thin devices, essential to overcome this optoelectronic trade-off.[5,9–12]

Conventional solar cell technologies utilized in space applications include c-Si,[13] gallium arsenide (GaAs),[14] and multijunction solar cells.[15] In contrast, certain emergent technologies such as organic photovoltaics, dye-sensitized solar cells, and a-Si are generally less suitable due to limitations related to reduced power density, radiation resistance, and long-term stability, crucial for long-term missions in the harsh conditions of space.[16–18] C-Si solar cells continue to be widely deployed for budget-constrained space missions,[16,19] due to their proven reliability and cost-effectiveness. GaAs solar cells, on the other hand, are known for their relatively high efficiency and radiation resistance, making them suitable for missions facing challenging radiation environments. Yet, multijunction solar cells continue to be the preferred power source for various satellites and spacecrafts, due to their high radiation and temperature tolerances and high efficiency. Despite theoretical efficiency potentials up to

I. M. Santos, M. Alexandre, A. T. Vicente, C. Teixeira, E. Almeida,
E. Fortunato, R. Martins, H. Águas, M. J. Mendes
CENIMAT/I3N
Departamento de Ciência dos Materiais
Faculdade de Ciências e Tecnologia (FCT)
Universidade Nova de Lisboa, and CEMOP/UNINOVA
2829-516 Caparica, Portugal
E-mail: imi.santos@campus.fct.unl.pt; rfpm@fct.unl.pt

The ORCID identification number(s) for the author(s) of this article can be found under https://doi.org/10.1002/solr.202400666.

DOI: 10.1002/solr.202400666

65% under 1 Sun irradiance,[20] multijunction cells have reached 39.2% of efficiency for a 6-junction III–V inverted metamorphic solar cell, while facing scalability limitations due to their small-area epitaxial growth processes.[21,22] With the increasing interest of private companies in space, cost-effectiveness is becoming another main requirement and more affordable PV solutions (yet guaranteeing high efficiency, robustness, and minimum weight) are now strongly demanded. In fact, an increase in space PV installation is expected in the low-Earth orbit (LEO), from a current installation of a few MW to ≈1 GW, over the next decade.[23,24] As such, rather than relying on the costly multijunction technology, thin-film solar cells, like copper indium gallium selenide (CIGS) and PSCs, are gaining popularity, due to their lightweight, flexible nature, and cost-effectiveness.[25–27] Moreover, contrastingly to multijunction solar cells, thin-film cells provide design versatility, scalability advantages, and can be integrated into flexible substrates that can be conformally adapted to spacecraft surfaces. This enables innovative and compact configurations of PV systems in space missions, as of large-area and roll-out solar arrays, as first introduced by the National Aeronautics and Space Administration.[28,29] Among these thin-film technologies, PSCs have been launched to near-Earth space[17,30] or have been bombarded with electrons, protons, gamma radiation, and neutrons to mimic the space irradiation on Earth installations.[18,30–36] This article uniquely emphasizes the potential of integrating lightweight, scalable photonic strategies into thin-film PV technologies, offering a viable path to reduce costs while maintaining high efficiencies necessary for emerging space applications.[35,36]

Perovskite-on-Si tandem solar cells (PSTSCs) are regarded as a hot-research topic aimed at achieving high-performance PV devices (>30% of power conversion efficiency [PCE]) suitable for terrestrial and extraterrestrial applications. This concept capitalizes on the maturity of the well-established c-Si PV technology together with the cost-effectiveness and bandgap tunability of PSCs, equipping highly efficient devices with flexibility and lightweight.[37,38] For that, distinct tandem configurations have been proposed for PSTSCs. Experimental reports have showcased efficiencies reaching ≈34% for series-connected two-terminal (2T) monolithic configurations. The 2T configuration is more adequate when assessing technical (installation/system) aspects and efficiency potentials than the four-terminal (4T) tandem configuration.[39–41] More specifically, 2T tandems require fewer electronic components (e.g., inverters, wires), and its potential efficiency is higher than that of four-terminal (4T) tandems, which is hindered by parasitic absorption in the two intermediate transparent conductive oxides (TCOs) required for the 4T configuration. As such, this review provides a thorough summary of 2T-PSTSCs, where efficiency and large-scale processing compatibility are key performance indicators (KPIs).[13,42]

Solar irradiance is another important aspect to consider when designing solar cells adapted for terrestrial or extraterrestrial applications. Outer space has a higher density of UV photons, when compared to the spectrum at the Earth's surface. Still, most of this energy is lost in the solar cells through reflection, parasitic absorption, or thermalization of hot carriers. Conversely, up to 52% of the solar radiation reaching the Earth's surface is of the infrared range ($\lambda > 700$ nm), largely unutilized by PV devices due to the optical bandgap of the absorber layers. This variability in light incidence prompts a discussion on "spectrum modification" approaches, including down-shifting (DS), up-, and down-conversion (UC and DC). DS utilizes a luminescent layer to absorb more energetic UV photons and re-emit them as longer-wavelength photons, to which a semiconductor is more responsive.[43–50] DC converts high-energy photons into two lower fractional energy photons, while UC encompasses the absorption of two sub-bandgap energy photons to yield a higher-energy photon. By coupling one or more of these approaches, both Earth and space PV installations can expect higher powering capabilities. This underscores the need for a comprehensive review of the latest "spectrum modification" approaches integrated into thick and thin solar cells for on-Earth applications, and their anticipated integration in upcoming space endeavors, as addressed here.

Another pressing challenge for PV systems and the design of spacecrafts is the extreme thermal fluctuations (from −200 to 130 °C). An illustrative thermal analysis revealed that space solar panels must withstand thermal cycles between −100 and 100 °C every 45 min in LEO,[51] due to the absence of heat transfer mechanisms like conduction or convection. Therefore, radiative cooling emerges as a predominant mechanism for effective heat dissipation. Traditional planar thick coatings, exceeding 50 μm in thickness, composed of materials such as poly(ethylene terephthalate) (PET), poly(ethylene naphthalate) (PEN) foils, Parylene C, or polyimide (PI), are employed to manage thermal dissipation PV devices in the mid-IR-to-IR wavelengths.[52–57] However, the weight and brittleness associated with their high thickness render standard rigid radiative coolers unsuitable for space applications. Contrastingly, thin radiative cooling coatings/schemes align with the requirements of thin solar cells, offering high stability, flexibility, and optimal performance with minimal weight.[53,58–60] Recent studies indicate that thin radiative coolers, with a thickness of less than 5 μm, can significantly enhance thermal resistance.[52,59,61] Understanding how radiative coolers can protect ultrathin solar cells fabricated with/on thermal sensitive materials is a crucial topic that will be examined in this review. This review presents a critical evaluation of how photonic radiative cooling techniques can be integrated into PV technologies for space missions, offering lightweight and effective solutions to mitigate thermal challenges faced by both terrestrial and extraterrestrial PV systems.

The multifaceted challenges posed by Earth's and space's environments demand innovative approaches for optimal energy harvesting and thermal management. By recognizing KPIs characteristic of each context (**Figure 1**), we provide a solid foundation for extrapolating insights that can guide the design and implementation of emergent photonics technologies. In Section 2, we present a detailed examination of the optical benefits arising from advanced LT strategies on thick c-Si slabs, along with electrical generation profiles when integrated into interdigitated backcontact (IBC) solar cells. In Section 3, a benchmark of thin/ultrathin solar cells (USCs) composed by a-Si:H, c-Si, or perovskite absorbers is presented. In Section 4, we evaluate the performance of emerging PSTSCs endowed with novel photonic strategies. Then, we present a review of the integration of photonic radiative coolers on thin solar cells based on sensitive materials via photonic schemes in Section 5. Lastly, the assessment of photonics for PV extends to the state-of-the-art

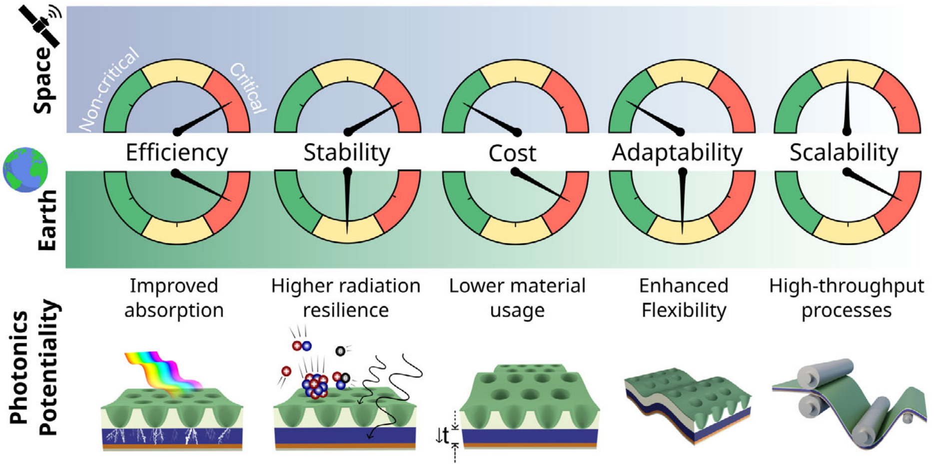

Figure 1. KPIs for space or Earth photovoltaic systems and the photonic means to improve them. Schematic illustration of the critical KPIs—efficiency, stability, cost, adaptability, and scalability—for photovoltaic systems in both space (top) and terrestrial (bottom) contexts. The color-coded scales represent the necessity of prioritizing each KPI within each specific scope (Earth or space) during system design and/or deployment: green indicates low need for consideration, where the KPI is less critical; yellow signifies moderate need; and red denotes high need, where addressing the KPI is crucial for optimal performance. For example, cost is highly critical for Earth-based systems but less so for space applications. The photonic structures illustrated along the bottom row highlight innovations tailored to enhance each KPI, showcasing how photonic strategies can meet unique challenges across Earth and space environments.

"spectrum modification" approaches integrated into both thick and thin solar cells, considering their applications in on-Earth scenarios and their near-future integration in space endeavors. This review addresses a critical gap in the literature by offering a comprehensive, experimentally validated analysis of photonic strategies tailored to solar-powering applications across both Earth and space environments. Our focus on such dual-context performance metrics, including LT efficiency, spectral modification, and thermal stability, provides a unique framework for guiding future PV technology development. By grounding our analysis in empirical data, we present actionable insights that bridge theoretical advancements with practical design considerations, establishing a foundational resource for optimizing PV systems to meet the specific challenges of both application environments.

2. Optically Improved Silicon-Based PV

In both terrestrial and extraterrestrial applications, addressing the delicate balance between optical gains and electrical performance is crucial for the optimal device performance.[51] This section explores advanced photonics-based schemes, beginning with optical enhancements for thick c-Si absorbers and their translation to electrical efficiency, particularly for the case of IBC solar cells. In closing, a concise discussion on the radiation resistance of c-Si cells is provided.

2.1. Thick and Thin Crystalline-Silicon Solar Cells

2.1.1. Absorption Gains Aiming Toward Lambertian Limits

Conventional LT strategies aimed to approach the Lambertian limits in c-Si solar cells involve the texturization of the c-Si absorber to form pyramids via standard alkaline wet-etching processes.[62–64] Usually, these strategies are first evaluated on c-Si wafers. That is the case of the work of Scheul et al.[65] that incorporated random pyramids on the front surface of a c-Si wafer. Beyond diminishing the total reflectance in the vis–NIR range via improved index matching, the high-refractive index pyramids scattered the incident photons toward the absorber (see diagram of **Figure 2**a). In average, up to 90% of the total reflected photons were diffuse (Figure 2b). There are alternative methods to create nanotextures, such as dry etching (reactive ion etching [RIE]), to produce the so-called black silicon (b-Si), and nanoimprint lithography (NIL). For instance, Addonizio et al.[66] varied the etching time of the nanotexturization process between 3 and 25 min. The largest amount of light antireflection (5.4% of total average reflectance in the range of 300–1000 nm) was observed for the highest average inclination angle (51°, lowest RIE), whereas an intermediate average inclination angle (39°) corresponded to 99.9% of Haze factor (Figure 2c). Thus, it was proven that the average inclination of the surface nanotextures was the main contributor to the average reflection and light scattering (Figure 2d). Alternatively, the pyramids may be integrated on the rear surface of a c-Si slab. Yet, this is still a controversial topic; for instance, Zhiqiang et al.[67] claims that the inclusion of both front and rear pyramids may be counterproductive. In this work, the absorption profile convoluted with the AM1.5 G solar spectrum of a double-side nanotextured wafer matched with that of a front-side nanotextured wafer, thus demonstrating no benefits from the texturization of both sides of a c-Si slab. On the other side, authors like Ingenito et al.[68] defend the nanotexturization of both top and rear surfaces of c-Si slabs. In this latter work, silicon slabs with both surfaces nanotextured were compared with front-side nanotextured slabs (from ≈20–185 μm). Both top and rear Si surfaces were conformally covered with thermal silicon oxide layers to counterbalance

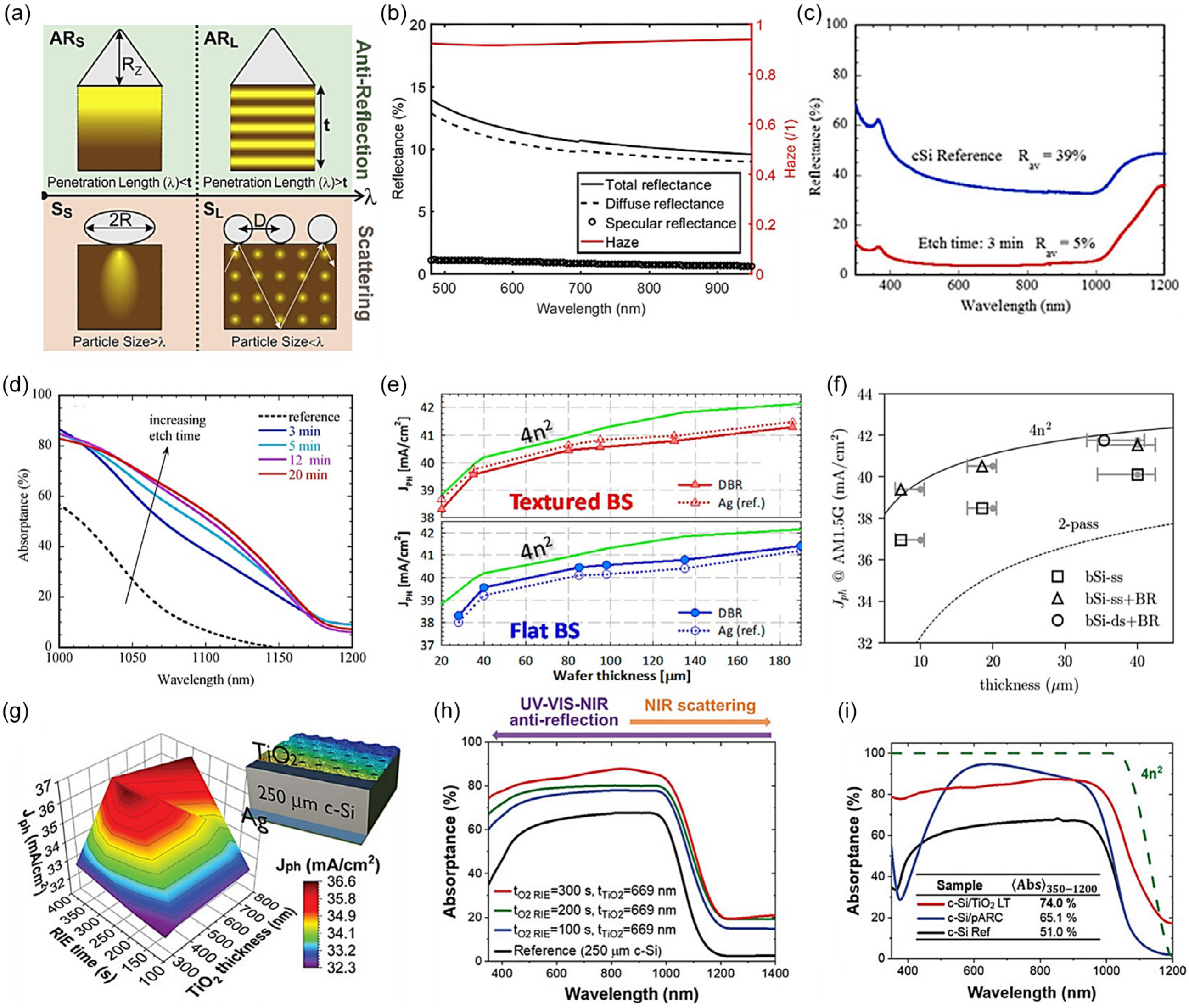

Figure 2. LT mechanisms and resulting optical improvements attained with photonic approaches integrated on c-Si devices. a) Diagram illustrating four characteristic E-field profiles from wave-optical front LT structures on thin-film solar cells with a back reflector. Black arrows indicate the main parameter influencing absorption enhancement in each profile. A transition (dashed line) in the solar spectral range separates the profiles produced by antireflection (AR) and scattering (S) effects. Reprinted with permission.[5] Copyright 2020, Elsevier. b) Total (full line), diffuse (dashed line), and specular (empty circles) reflectance (black) and haze factor spectra (red) for the pyramidal textured c-Si wafer. Reprinted with permission.[65] Copyright 2020, John Wiley and Sons. c) Reflectance spectra optimal wafer with 3 min of texturing time and planar counterpart. d) Absorptance spectrum of c-Si wafers submitted to different etching times. Reprinted with permission.[66] Copyright 2019, Elsevier. e) Photocurrent density, J_{PH}, calculated between 400 and 1200 nm for AM1.5 illumination as a function of distinct c-Si wafer thicknesses in the case of textured (top) and flat backside (BS, bottom). Reprinted with permission.[68] Copyright 2014, American Chemical Society. f) Comparison of ideal J_{PH} for ultrathin black silicon (b-Si) substrates of varying thicknesses and backside configurations under AM1.5 G solar spectrum. bSi-ss denotes black silicon with a nanotextured front surface and a polished back surface, while bSi-ds refers to c-Si wafers with nanotextured surfaces on both sides. The double-pass absorption (2 pass) spectrum is included for reference. Reprinted with permission.[70] Copyright 2023, John Wiley and Sons. g) Absorptance spectra and h) 3D plots of integrated J_{PH} of representative batches of c-Si wafers coated with TiO_2 photonic nanostructured coatings corresponding to different O_2 reactive ion etching time ($t_{O2\ RIE}$) and with the thicknesses (t_{TiO2}) fabricated on top of 250 µm-thick c-Si wafers. i) Absorptance spectra comparison between the best-performing samples with nanostructured coatings (c-Si/TiO_2 LT), a planar counterpart (c-Si with a front optimized planar antireflection coating, c-Si/pARC), and a bare c-Si wafer. The $4n^2$ spectrum represents the ideal absorption profile as determined by Lambertian formalism, included for reference. Reprinted with permission.[10] Copyright 2023, John Wiley and Sons.

the recombination induced by the nanotexturization. As shown in Figure 2e, the gap between the J_{ph} predicted by the $4n^2$ absorption limit and that determined from the measured absorptance is smaller for thinner absorbers with front and rear nanotextures than front-side nanotextured absorbers. The 35 µm double-side nanotextured Si slab attained ≈99% of the photocurrent density of the classic Lambertian limit, whereas the thickest slab with 185 µm reached ≈98%. This work defines 35 µm as the c-Si wafer thickness threshold below which any additional backward scattering effects provided by the rear pyramids start to undermine the forward scattering effects provide by the front textures. This is in accordance to the previous simulations of Kowalczewski et al.[9] that stated that decreasing the thickness below 40 μm is counterproductive, as it significantly reduces the maximum achievable efficiency. This stems from limited light absorption and pronounced surface recombination, even when proper LT approaches are implemented to maximize the light absorption within such thin absorbers. In that case, it is paramount to simultaneously improve the quality of the contacts, which reduces contact recombination, to improve the performance of the solar cell beyond what is possible solely via LT, especially as we reduce the Si absorber thickness below 20 μm.[69] Later, Garín et al.[70] combined front-side nanotextured c-Si wafers (10–40 μm) with a rear distributed Bragg reflector (rDBR) that covered the rear surface of the slabs. The front nanotextures were designed via cryogenic deep RIE (cDRIE) that minimized the Si etching and damage. From Figure 2f, it is seen that the photocurrent of front-side nanotextured slabs of thicknesses <10 μm coupled with rDBRs surpassed those defined by the $4n^2$ (Lambertian) absorption limit, as a result of reflection mitigation and pronounced light-scattering toward the absorber. These findings demonstrate how b-Si nanotexturization can be excellent for LT purposes. Texturizing just the front surface could efficiently reduce front reflectance and boost absorption in the NIR range for standard c-Si-based solar cells.

Recent advances in the field of wave optics have introduced a novel class of photonic nanostructured coatings to circumvent the traditional optoelectronic compromise associated with PV absorber texturization processes.[5] These wavelength-sized structures were first proposed by Santos et al.[10] that endowed both standard (250 μm) and thin (90 μm) c-Si wafers with a TiO_2 front photonic nanocoating and a Ag rear mirror, as illustrated in Figure 2g. These structures were directly fabricated on the Si wafers via nanosphere lithography (NSL), a soft-lithography technique employing self-assembled micro- or nanospheres to create periodic nanostructures. The nanocoatings, atop flat c-Si wafers, provided a gradual index matching toward the absorber (see diagram of Figure 2a, domain AR_s), significantly enhancing absorption across the UV–vis–NIR spectrum (Figure 2h). However, due to incomplete coverage of the front surface, substantial reflection losses in the UV–vis range limited the J_{ph} to only up to 84% of the classical $4n^2$ Lambertian limit (Figure 1i). This corresponds to ≈36 and 37 mA cm^{-2} for the 90 and 250 μm c-Si wafers. The absorption profile of these optically enhanced devices surpassed the Lambertian limit for NIR wavelengths beyond 1150 nm. This improvement stems from intense forward scattering of the incident photons, which introduced interference effects that are not accounted for in the geometric ray optics domain inherent to the Lambertian formalism. While this novel approach holds promise, ongoing research should aim to augment its optical performance to further align with that demonstrated by traditional methods.

2.1.2. Photonic-Enhanced Silicon-Based Solar Cells

Standard texturization methods are routinely used to improve the optoelectronic performance of commercial c-Si-based solar cells. The IBC solar cell, a leading architecture in commercial c-Si technology, is poised to yield exceptional PCEs approaching the practical limit of ≈29%.[63,71,72] It minimizes shading, maximizes charges collection and the exposure of the top surface area to incident light, while effectively mitigating recombination and resistive losses.[10,70,73] This architecture was initially proposed in 1977 by Lammert and Shwartz et al.[74] with the first corresponding paper published by Swanson et al.[75] who modeled a 23% efficient IBC cell in 1984. With both contacts on the cell's rear side, this architecture is the ideal platform to integrate LT nanocoatings on its fully exposed top surface. Typically, n-type c-Si wafers are favored for such devices given their proven lower susceptibility to light-induced degradation and higher quality compared to p-type ones.[76] Masuko et al.[77] fabricated IBC solar cells with front microtextures conformally covered with a passivation layer to sustain the deposition of a silicon nitride (SiN) antireflection coating (ARC) (**Table 1**). This design yielded up to 25.6% of PCE and 41.8 mA cm^{-2} of J_{SC}, which corresponded to 97.2% of the corresponding Lambertian J_{ph} value (determined for the same c-Si absorber thickness). Later, Adachi et al.[78] reported an IBC solar cell that allied front random texturing techniques with plasma-enhanced chemical vapor deposition (PECVD) to respectively fabricate front random textures for antireflection and a passivation intrinsic a-Si:H layer. The minority carrier recombination at the surface of the textured wafer was suppressed by adding the a-Si:H layer, leading to a high open-circuit voltage (V_{OC}) and a fill factor (FF) of 83.5%. Thereafter, Yoshikawa et al.[63] demonstrated a 26.3% efficient IBC cell with up to 1% of optical loss (absolute efficiency loss of the theoretical limit, 29%) due to front reflection of UV photons and NIR photons (>1000 nm) escaping, as shown in **Figure 3**a. The remarkable optoelectronic performance arises from the front-side random pyramids that provide a soft index matching path to the UV–vis–NIR photons with small current losses (minimized to 0.5%) by adding a front intrinsic a-Si:H layer. Moreover, two other ARCs were applied to minimize reflection losses, resulting in an ultimate J_{SC} of 42.3 mA cm^{-2} (Figure 3b), which corresponds to 98.2% of the respective Lambertian photocurrent limit.

Alternatively, nanotexturing the front surface of c-Si wafers may be transferred to IBC solar cells rather than submitting the c-Si wafer to standard texturing methods. However, the first few attempts that integrated b-Si into IBC cells have reported efficiencies <20% due to significant charged carriers recombination at the front nanostructured surface.[79,80] The first successful work that reported front-side nanotextured IBC cells with high efficiency (≈22.1%) was published in 2015 by Savin et al.[81] They deposited a conformal alumina (Al_2O_3) chemical/electrical passivation film via atomic layer deposition over the b-Si fabricated via cDRIE, as suggested by Otto et al.[82] Even with relatively thick (≈280 μm-thick absorber) devices, the integration of this conformal thin passivation layer overcame the surface recombination issues that were limiting the efficiency of previously reported devices.[79,80] The resulting b-Si provided an effective index matching to UV photons (<500 nm) that were reflected by the respective standard front microtextured counterpart (Figure 3c), achieving up to 42.2 mA cm^{-2} of J_{SC}, which corresponds to 97% of the respective Lambertian photocurrent. Moreover, such nanotextures have proven to be independent

Table 1. Summary of optical performance of c-Si solar cells endowed with distinct LT approaches reported in the past decade. The power-to-weight ratio accounts for the weight of the solar cells, with detailed calculations and data available in the Supporting Information. (*Thickness of the full cell; da-designated area; ap-aperture area; ta-total area; sc-single-crystal).

#	Ref/Year	LT strategy	Wafer thickness [μm]	Silicon wafer type	Solar cell type	Area [cm^2]	Power-to-weight ratio [$W\,g^{-1}$]	Improved Optical Mechanisms	Initial J_{sc} [$mA\,cm^{-2}$]	Final J_{sc} [$mA\,cm^{-2}$]	Initial PCE [%]	Final PCE [%]	$\frac{J_{sc}}{J_{sc}^{Lamb}}$ [%]
1	[77]/2014	Front random micropyramids	150	n-type	IBC	143.7 (da)	0.73	Antireflection	–	41.8	–	25.6	97.2
2	[88]/2015	Front random micropyramids + NWs	200	p-type	DTSE	10.8 (ta)	0.40	Antireflection	36.7	37.3	17.2	17.9	86.3
3	[81]/2015	Front Nanopyramids	280*	p-type	IBC	9.0 (ta)	0.34	Antireflection	42.0*[a)]	42.2	22.0*[a)]	22.1	97.0
4	[78]/2015	Front random microtextures	160	n-type	IBC	151.9 (ta)	0.67	Antireflection	–	40.8	–	25.1	94.8
5	[383]/2016	Front random nanopyramids	200	p-type	LDSE	6.3 (ta)	0.38	Antireflection + Scattering	–	36.3	–	18.1	84.0
6	[62]/2016	Front random micropyramids	154	n-type	IBC	153.5 (ta)	–	Antireflection	–	41.3	–	25.2	96.0
7	[89]/2016	Front random micropyramids + NWs	525	p-type	MAEE, BSF*[b)]	1.0 (ap)	0.07	Antireflection	22.2	28.2	7.2	10.3	64.2
8	[73]/2017	Front random micropyramids	280	n-type	IBC	9.0 (da)	0.24	Antireflection	–	42.3	–	26.3	98.2
9	[63]/2017	Front random micropyramids	165	n-type	IBC	180.4 (ta)	0.69	Antireflection + Scattering	34.5	41.0	15.7	20.1	94.3
10	[384]/2018	Front random micropyramids	160	p-type	Simulated cell*[c)]	49.0 (da)	–	Antireflection	–	42.4	–	22.2	98.5
11	[385]/2018	Front random micropyramids	180	n-type	HJ-TOPCon	1.0 (ta)	0.47	Antireflection + Scattering	31.1	37.1	–	19.1	86.0
12	[386]/2018	Inverted front random micropyramids	200	p-type	sc-Si cell*[d)]	247.0 (ta)	–	Antireflection	38.3	38.5	20.0	20.2	89.0
13	[90]/2019	Front random micropyramids + NWs	–	p-type	sc-Si cell*[d)]	161.0 (ta)	–	Antireflection	37.0	37.7	18.2	18.8	–
14	[387]/2020	Front ordered micropyramids	200	p-type	pc-Si*[e)]	16.0 (da)	–	Antireflection	32.4	35.8	14.1	14.8	83.0
15	[388]/2020	Concave front random pyramids	165*[f)]	p-type	PERC	–	–	Antireflection	37.74	37.7	20.7	20.9	87.5
16	[389]/2021	Front ordered inverted pyramids	180	p-type	PERC	246.5 (ta)	0.43	Antireflection	39.8	41.3	21.1	22.6	95.7
17	[390]/2021	Front random nanopyramids	–	p-type	mc-Si	246.5 (ta)	–	Antireflection	36.0	36.7	18.0	18.5	–
18	[391]/2022	Front random micropyramids	180	p-type	PERC	246.5 (da)	–	Antireflection	41.9	42.4	22.3	22.7	98.3
19	[392]/2022	Front random micropyramids	160	n-type	TOPCon	441.0 (ta)	–	Antireflection + Scattering	41.3	41.5	24.8	24.81	96.4
20	[10]/2023	Front ordered nanovoids	180	n-type	IBC	4.4 (ta)	0.35	Antireflection + Scattering	24.9	31.9	10.7	13.9	73.9
21	[70]/2023	Front random nanopyramids	40	n-type	IBC	20.3 (ta)	–	Antireflection + Scattering	27.1	35.4	11.5	16.4	85.2
22	[393]/2024	Front random micropyramids	180	p-type	IBC	–	–	–	–	40.4	–	20.4	93.6

[a)] *Relative to a reference cell with front random textures. [b)] *Solar cell with BSF and front micropyramids covered with Si-NWs. No solar cell architecture is mentioned in the respective article. [c)] *Simulated device considering the implied V_{OC} and the reflection spectrum. [d)] *Cell architecture composed of textured wafers coated with a front SiN_x ARC. The top and rear contacts were screen printed. [e)] *Standard cell architecture composed of polycrystalline-silicon (pc-Si) textured wafers coated with a front SiN_x ARC. The top and rear contacts were screen printed. [f)] *Simulated cell structure.

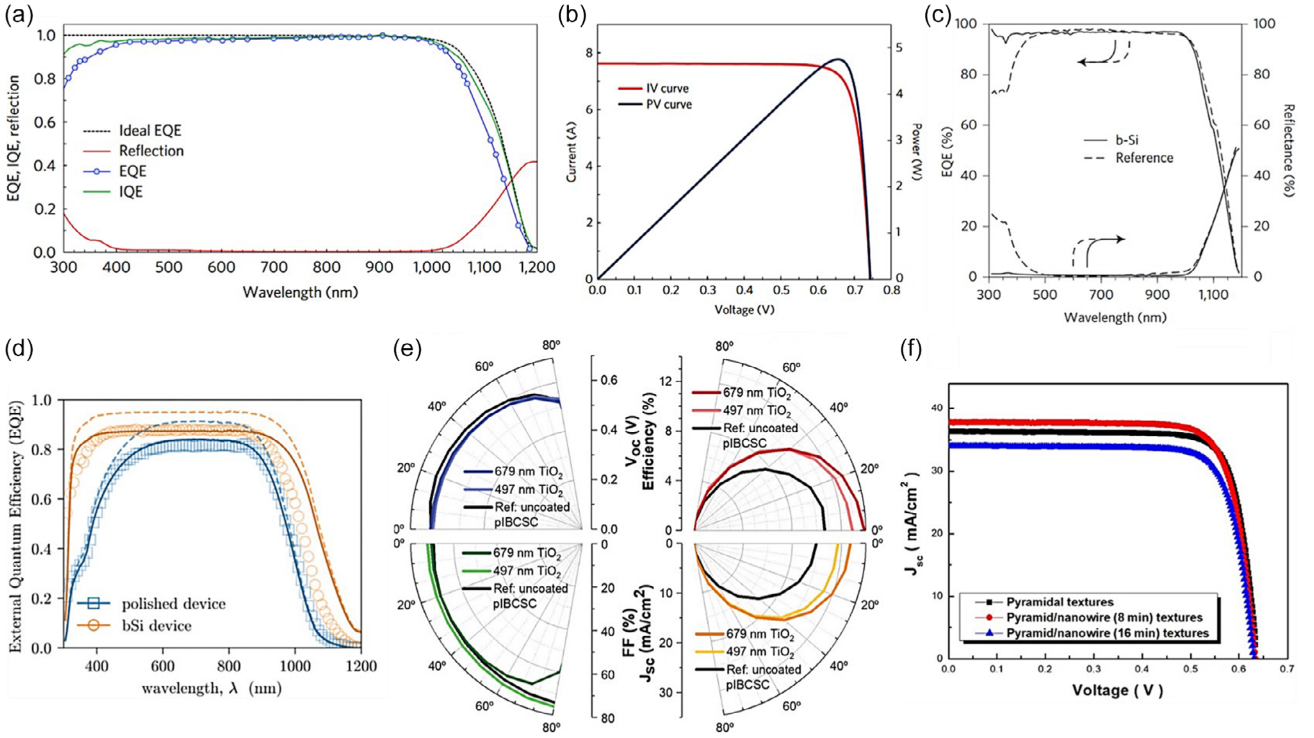

Figure 3. Optoelectronic (including angular acceptance) performance improvements attained with photonic approaches integrated on c-Si devices. a) Ideal and measured EQE respectively in black dashed and full green line, internal quantum efficiency reflection spectra and b) the current–voltage (*I*–*V*) curve and power–voltage curves of the optimal heterojunction IBC (HJ-IBC) solar cells are represented by full red and dark blue lines, respectively. Reprinted with permission.[63] Copyright 2017, Springer Nature. c) EQE and reflectance spectra obtained for the optimal black silicon (b-Si) solar cell (solid lines) and the corresponding randomly texturized cells (dashed lines). Reprinted with permission.[81] Copyright 2015, Springer Nature. d) EQE spectra of polished (blue) and black silicon (b-Si) (orange line) devices. Experimental values are represented by empty symbols, while theoretical calculations are depicted by full lines. The calculated maximum EQE curves, assuming no electrical losses, are shown in dashes. Reprinted with permission.[70] Copyright 2023, John Wiley and Sons. e) Polar plots presenting the angular dependence of V_{OC} (blue), FF (green), efficiency (red), and J_{SC} (orange). Reprinted with permission.[10] Copyright 2023, John Wiley and Sons. f) *J*–*V* curve of c-Si solar cells with textured absorber with or without nanowires prepared for distinct texturization times. Reprinted with permission.[90] Copyright 2019, Elsevier.

of the incoming light direction, even for high angles of light incidence (<75°), contrary to the standard counterpart, which suffered from major optical losses from front reflection of UV photons. The improved angular acceptance resulted in a 3% increase in daily energy production when compared with a reference cell with similar efficiency. The benefits of b-Si become more prominent when thinning the c-Si absorber. Garín et al.[70] further applied the b-Si concept on IBC solar cells with a 40 μm c-Si slab. Analogous to the previously discussed work of Savin et al.[81] the nanotextures were passivated with a conformal Al_2O_3 layer, which supported the deposition of a SiC ARC. The device was then encapsulated with traditional epoxy and glass layers. This architecture yielded a PCE of 16.4%, corresponding to ≈43% efficiency gain relative to a reference cell with a c-Si polished front surface. The device's electrical output capitalized on the improved LT through enhanced index matching and intense forward scattering, respectively of the impinging low- and high-energy photons, as corroborated by the external quantum efficiency (EQE) profile shown in Figure 3d. These breakthroughs show the feasibility of b-Si in industrial production, while also aiming for even higher efficiencies. Rather than texturing the Si absorber, Santos et al.[10] implemented a novel class of photonic nanostructured coatings on planar IBC solar cells, enhancing the efficiency up to 30% (compared to an uncoated reference cell) and reaching an absolute PCE of ≈14%. The high aspect ratio of the TiO_2 nanocoating showcased a combination of antireflection and light scattering for longer wavelengths (>900 nm), resulting in over 150% enhancement of the EQE for wafers with 679 nm-thick TiO_2 front features (Figure 2d). Figure 3e emphasizes the enhanced angular acceptance (<80°) of these curved features, even under extreme angles of light incidence. This characteristic is valuable for solar devices lacking sun-tracking mechanisms and is especially crucial for thin or ultrathin solar cells.[83,84] The feasibility of this concept, across various solar cell technologies, underscores its importance, providing both optical and electrical enhancements through an industrially friendly approach.

Other surface morphology modification approaches have been developed to enhance the optical performance of Si-based solar cells. In particular, metal-assisted chemical etching (MACE) has proven effective in producing Si nanowire (NW) arrays with low reflectance and strong broadband optical absorption.[85–87] For instance, Kim et al.[88] employed MACE to fabricate Si NWs on random micropyramids, utilizing Ag nanoparticles (NPs) as a mask for electroless etching for double-textured selective emitter (DTSE) solar cells. The Si NWs significantly enhanced light absorption within the Si absorber, primarily through improved UV–vis–NIR antireflection effects. For a 45 s MACE process, the lowest average reflectance reached a minimum of 6.2% in the useful range of 300–1100 nm. The incorporation of a selective emitter on the top surface of the double-textured reference cells improved the PCE by ≈4.0% to achieve 17.9%, comparatively to the reference cell without the selective emitter. The resultant J_{SC} of 37.3 mA cm^{-2} equated to 86.3% of the respective Lambertian photocurrent. Later, Huang et al.[89] employed metal-assisted electroless etching (MAEE) to fabricate Si-NWs on random micropyramids. The resulting NW/micropyramids cells minimized reflectivity to ≈1.1%, regarding the entire "useful" wavelength spectrum of Si. The optimal devices displayed respective V_{OC} and J_{SC} enhancements of ≈3.8% (final V_{OC} of 540 mV) and 27% (final J_{SC} of 28.2 mA cm^{-2}) over reference cells with front random micropyramids. Consequently, Si-NWs/micropyramids features led to superior photovoltaic characteristics, boasting the PCE up to ≈10.3%, which corresponds to a ≈43% improvement. More recently, Putra et al.[90] followed a MACE process to create similar LT features. The PCE values demonstrate a comparable efficiency (≈0.6% absolute difference) after the formation of the Si-NWs on top of the random pyramids (Figure 3f). However, the increase of the etching time was followed by a proportional increase of the series resistance (R_S), which was ≈2.7 times larger than that of the pyramid-only solar cells for the highest etching time (24 min) and hindered the devices' efficiency. Despite the promising features of the two-scale approaches, the obtained efficiencies remain noncomparable to those attained through standard one-step texturing and DRIE processes.

2.1.3. Radiation Resistance of Silicon-Based Solar Cells

The Vanguard 1, launched in 1958 to LEO, was the first solar-powered satellite by single-crystal Si-based solar cells (1 W of maximum power point and PCE = 10% at 28 °C). It remained in operation uninterruptedly for 6 years, enduring the harsh conditions of space.[91,92] For the next two decades, c-Si solar cells were the preferred power source for space applications. Presently, c-Si solar cells are primarily chosen for low-power space missions, given their cost-effectiveness (costing 6–9 times less than III–V multijunction solar cells), lower weight, and a less harmful manufacturing process that avoids the use of toxic gases.[16,93] The historical usage of c-Si solar cells in space applications underscores their reliability and resilience against ionizing radiation, which is paramount to the success of prolonged space missions.[94,95]

The first breakthrough in Si photovoltaics for space applications occurred in 1972 with the pioneering work of Lindmayer et al.[96] (**Table 2**). The introduction of "violet cells" marked a breakthrough due to their improved quantum yield to short-wavelength photons. These cells integrated a back surface field (BSF) design with a shallow 0.1 μm diffused junction and novel grid pattern to efficiently collect current from this shallow region. More importantly, it couples a Ta_2O_5 ARCARC to minimize reflection losses of high-energy photons, resulting in a 17% increase in efficiency of the "violet cells" compared to previous state-of-the-art c-Si solar cells, achieving around 13.0% efficiency. Even after irradiation with 1 MeV electrons at a fluence of 3×10^{14} particles per cm (p cm^{-2}), the efficiency reduced by only ≈15%, still surpassing state-of-the-art c-Si cells. The resistance of "violet cells" to proton irradiation, evaluated by Ardnt[97] in 1974, demonstrated a superior FF retention compared to standard c-Si cells when subject to proton bombardment (2 and 4 MeV at a 10^{13} p cm^{-2} fluence, for 250 μm-thick "violet cells"). While the FF of state-of-the-art Si cells reduced from 0.74 to 0.32, that of the "violet cells" only decreased from 0.77 to 0.74. Further advancements by Matsutani et al.[98] in 1982 with 50 μm c-Si cells, using a BSF design with a back surface reflector (BSR) on a front-texturized BSFR cell, exhibited an electrical performance and radiation resistance under 1 MeV electron irradiation comparable to those observed by Lindmayer et al.[96]

Table 2. Summary of radiation testing for c-Si solar cells endowed with LT approaches, showing decreases in V_{OC}, I_{SC}, and PCE, determined with respect to the beginning of life (BOL) and end of life. The power-to-weight ratio accounts for the weight of the solar cells, with detailed calculations and data available in the Supporting Information (*BSF).

#	Ref/Year	LT strategy	Wafer thickness [μm]	Solar cell type	Area [cm^2]	Power-to-weight ratio [W g^{-1}]	Irradiation energy [MeV]	Fluence particle [cm^{-2}]	V_{OC}^{BOL} [mV/$\Delta_{V_{OC}}$, %]	I_{SC}^{BOL} [mA/ΔI_{sc}, %]	PCE^{BOL}/ Δ_{PCE} [%]
1	[96]/1972	T_2O_5 ARC	150	BSF*	4 (ta)	0.55	1	3×10^{14}	592/−4.4%	160.0/−12.5%	13.5%/−14.8%
2	[98]/1982	Front random pyramids + ARC	50	BSFR*a)	4 (ta)	2.11	1	–	585	155.0	13.6
3	[75]/1986	Front inverted pyramids + double ARC	–	PERL	–	–	1	–	–	–	20.8
4	[99]/1994	Front inverted random pyramids + ARC	100	NRS/LBSF	4 (ta)	1.05	1	3×10^{14}	637/−11.0%	194.0/−11.9%	18.0
5	[99]/1994	Front inverted random pyramids + ARC	100	NRS/BSF	4 (ta)	0.99	1	3×10^{14}	625/−10.4%	191.0/−10.0%	17.0
6	[107]/2000	Deep holes + front ARC	200	"Trench"	–		1	3×10^{15}	619/−19.4%	43.8*b)/−18.3%	15.6/−35.3%
7	[108]/2001	Front random texturing	70	BJ	4 (ta)	1.41	1	1×10^{15}	621/−17.4%	189.7/−1.3%	16.4/−18.9%

a)*BSF together with BSR; b)*short-current density J_{SC}; ta-total area.

(585 mV of V_{OC}, 155 mA of I_{SC}, and 13.6% of efficiency). The next jump in efficiency was achieved by Kawasaki et al.[99] in 1994, with the introduction of nonreflective surface/localized BSF (NRS/LBSF) and NRS/BSF Si-based solar cells, both featuring SiO_2 front and rear passivation layers. Under AM0 irradiation, the NRS/LBSF cells reached 637 mV of V_{OC}, 194 mA of I_{SC}, and 18% efficiency, while the NRS/BSF devices presented a slightly lower electrical performance (625 mV of V_{OC}, 191 mA of I_{SC}, and 17% of efficiency). However, the NRS/BSF cells demonstrated a higher resistance to electron irradiation (V_{OC} and I_{SC} respectively diminished by 10.4% and 10.0%) than the NRS/LBSF cells (11.0% and 11.9% reduction for V_{OC} and I_{SC}, respectively). The decrease in V_{OC} and I_{SC} in both cells, attributed to the irradiation of high-energy particles causing defects in the Si lattice and reducing the minority carrier lifetime in both emitter and base regions, was more pronounced in the NRS/LBSF cells. This is a consequence of the higher susceptibility of the nondiffused Si and thermal-grown SiO_2 (Si/SiO_2) back interface of the NRS/LBSF cells to electron irradiation, leading to an increase of the recombination rate and diode saturation current. In contrast, the boron diffused silicon and silicon dioxide back interface exhibited greater resilience. Following research, such as that by Zhao et al.[100] introduced a novel solar cell design resembling the present-day passivated emitter and rear locally diffused (PERL) cells. This approach integrated approaches like BSF, BSR, inverted pyramid LT structures, and double-layer ARC to minimize surface reflection and enhance sunlight absorption. By the late 1990s, PERL cells achieved efficiencies of up 20.8% under space irradiation.[101] In 1996, Yamaguchi et al.[102] evaluated the lifetime of Si-based solar cells by irradiating them with 1 MeV energy electrons at fluences of 10^{14}–10^{17} p cm^{-2}. The study revealed a gradual reduction in I_{SC}, V_{OC}, and P_{max} for fluences below 2×10^{16} p cm^{-2}. Interestingly, for intermediate electron fluences (from 2×10^{16} to 5×10^{16} p cm^{-2}), the I_{SC} increased while V_{OC} decreased due to the broadening of the depletion layer, a phenomenon later corroborated by Hisamatsu et al.[103] Additionally, Karazhanov[104] attributed the increase in I_{SC} to the conversion of the conductivity type of the base layer from p- to n-type, along with an increase in the minority carrier lifetimes compared to the majority carriers' lifetime, thus disproving his first proposed model.[105] In a more recent work by Hamache et al.[106] electrical modeling, via the (simulation tool)-solar cell capacitance simulator-1D program, of an n^+pp^+ silicon solar cell under 1 MeV electron irradiation, revealed that minority carriers in the p-type base were responsible for the type inversion.[95] However, for higher electron fluences ($>5 \times 10^{16}$ p cm^{-2}, high-fluence region), the devices failed, attributed to an abrupt increase in the series resistance of the Si layer arising from the -type base layer and a reduction in carrier concentration.[94] A similar trend was observed for irradiation with 10 MeV protons at fluences ranging from 10^{11} and 2×10^{14} p cm^{-2}.

Alternatively to conventional texturing processes, Presting et al.[107] fabricated c-Si solar cells with 100 μm-deep holes within the absorber using DRIE and then irradiated them with 1 MeV electrons with different doses ranging from 10^{14} p cm^{-2} to 3×10^{15} p cm^{-2}. At the highest dose, the efficiency of the c-Si cell with the densest hole configuration decreased by ≈35%, while that of a standard planar counterpart (w/o deep holes) decreased by ≈38% at the end of the devices' lifespan. The authors stress the need for effective LT structures, which were not considered in their work, to match the efficiency of the fabricated devices (≈15%) with those previously reported (>17%). Later, Tonomura et al.[108] fabricated both-side junction (BJ) c-Si solar cells using thin (≈70 μm) c-Si wafers and irradiated them with 1 MeV electrons at doses up to 1×10^{15} p cm^{-2}. At the highest dose, the decrease in minority carrier lifetime caused by space irradiation was counterbalanced by an increase in the charge collection probability from the front and rear p–n junctions. Consequently, the BJ cells, with an efficiency of 16.4% (AM0, 28 °C), demonstrated greater radiation resistance compared to traditional front-junction and rear-junction c-Si solar cells; while the efficiency of standard textured cells dropped by ≈27%, that of the BJ cells only reduced by ≈19%. The electric parameter most affected by the 1 MeV irradiation was the V_{OC}, which decreased by ≈17% due to a pronounced decrease of the carrier's lifetime. Overall, these findings underscore the importance of integrating appropriate LT approaches and solar cell designs to stabilize the optoelectronic performance of space cells under extreme irradiation doses.[13,94,109–111]

3. Wave-Optical Elements for Thin Solar Cells

Thin and USCs, driven by environmental sustainability concerns, promise reduced material usage and production costs. Despite their potential for flexible applications and reduced power-to-weight ratio for aerospace applications, the lower power generation due to incomplete light absorption and pronounced bulk and surface recombination poses serious obstacles.[9] As discussed below, such challenges can be addressed by adopting efficient LT strategies assisted by adequate passivation schemes.[5,112–118]

In the upcoming subsections, the LT efficiency of each photonic approach is assessed by first plotting the respective J_{SC}, determined experimentally or numerically. These J_{SC} values are then compared with three reference models: single-pass absorption, double-pass absorption, and the exact Lambertian absorption limits[119] and simultaneously compared to the J_{SC} of the planar counterpart (a cell with an optimized front planar ARC and rear mirror, representing the double-pass absorption limit). Given the fact that both J_{SC} and respective enhancement (as seen in the first and second plots) vary with the absorber thickness, the equivalent thickness of a planar absorber, with the same volume, was adopted for structured absorbers (e.g., textured surfaces, NWs) for comparison purposes. Due to the early stages of some of the elected studies, this review focuses on the optoelectronic characterization of single-junction solar cells under standard AM1.5G solar illumination. The complete dataset used in this analysis is provided in the Supporting Information. For c-Si absorbers, the dataset provided by Massiot et al.[76] was extended to include the latest available literature.

3.1. Silicon Absorbers

a-Si:H solar cells are characterized by their disordered structure, offering unique advantages appealing to low-power consumer-oriented applications while leveraging flexibility. However, a-Si:H is also a well-known detector material for its radiation resistance, accentuating its usability in solar panels for space applications, for example, beam flux, particles, or X-Ray radiation detectors.[120,121] Despite their efficiency plateauing at around 14% since 2016,[22] which considerably lags behind the record of c-Si PV (≈27%) and the theoretical limit for single-junction cells (≈34%) according to Shockley–Queisser,[3] effective light management (LM) is of significant importance to advanced optically thick a-Si:H solar cells suitable for space applications.

The pioneering work of Sanchez et al.[83] introduced front-wavelength-sized structures for a-Si:H thin absorbers, employing NSL to nanostructure the front indium zinc oxide (IZO) electrode, as depicted in **Figure 4**a. These optimized photonic elements demonstrated strong antireflection properties in the visible–near infrared (vis–NIR) range and induced light-scattering effects in NIR (Figure 4b), resulting in a 27% J_{SC} improvement, under normal light incidence. Under oblique light incidence (70°), J_{SC} and efficiency enhancements reached up to ≈53% and ≈52%, respectively. Building upon this foundation, Mendes et al.[7] further investigated and modeled the LT phenomena in a-Si:H solar cells with absorber thicknesses of 100 and 300 nm (Figure 4c), to optimize front titanium dioxide (TiO_2) voids and domes. This approach led to a significant 37% enhancement in photocurrent, with domes demonstrating particularly intense antireflection effects, including a lens effect. In summary, while a-Si:H solar cells may not be ideal for high-power space missions, they hold promise for low-power and autonomous applications where flexibility, lightweight construction, and cost-effectiveness are paramount. Furthermore, the integration of a-Si:H cells with other technologies, such as microstrip slot array antennas[122] or three-terminal heterojunction bipolar transistor solar cells,[123] offers opportunities for compact, reliable, and long-term power generation in space, with potential advantages in terms of space-saving design, minimal interference, and enhanced radiation tolerance.

Despite the advantages offered by a-Si:H thin film solar cells, c-Si solar cells are unmatched in efficiency and reliability. Research increasingly focuses on thin c-Si solar cell, with wafer thickness slightly above 100 μm, driven by cost competitiveness and economies of scale.[5] Future advancements are expected to leverage high-quality materials and thin-film technologies for even thinner monocrystalline Si layers. Proper LT schemes are crucial for maximizing NIR photon collection, particularly beneficial for c-Si due to its indirect bandgap. Thus, thin and ultrathin (micrometer-thick) c-Si cells serve as test bed to integrate LT schemes for highly efficient PV devices.[76,124,125] The reported J_{SC} values of thin c-Si solar cells predominantly fall between the reference curves of single- and double-pass absorption (**Figure 5**a), clustered by fabrication processes and thickness range. The respective J_{SC} enhancements determined with respect to the double-pass absorption models are plotted in Figure 5b.

Recent papers report on c-Si absorbers with thicknesses ≥10 μm, often fabricated by CVD or exfoliation from thick wafers. These cells commonly employ the dual-step LT approach, combining an optimized ARC with front microscale random upright pyramids and a metal back reflector. Notably, Balaji et al.[126] achieved 37.2 mA cm^{-2} of J_{SC} with a 40 μm-thick absorber by depositing intrinsic and n/p-doped a-Si:H layers via PECVD. This formed i-p/c-Si/i-n stack that passivated the top and rear surfaces of the Si wafer. Moreover, the front textures were coated with a stack of SiO_2:ITO, that decoupled both antireflection and conductive properties that are usually concentrated in a thick layer of TCO.[124] The thin ITO layer was deposited to minimize UV parasitic absorption, while providing the necessary carrier transport and Ohmic contact, while the SiO_2 layer complemented the stack with proper antireflective properties and minimum parasitic absorption. Furthermore, Hilali et al.[127] reported ≈36.0 mA cm^{-2} of J_{SC} with a ≈25 μm-thick solar device, incorporating a rear Si_3N_4 layer between the double-side textured Si absorber and the rear metallic mirror, enhancing back reflectance to ≈95% and the optical path length of NIR photons by 5.8%. The J_{SC} (≈36.0 mA cm^{-2}) of the fabricated devices approaches that of standard thick (≈180 μm) c-Si solar cells.

More sophisticated and efficient LT methods are needed for c-Si absorber thicknesses below 10 μm. Silicon-on-insulator, albeit costly, is commonly employed for proof-of-concept devices in this range of thickness, due to its minimal impact on capacitance (hence highly efficient devices).[76] However, attention

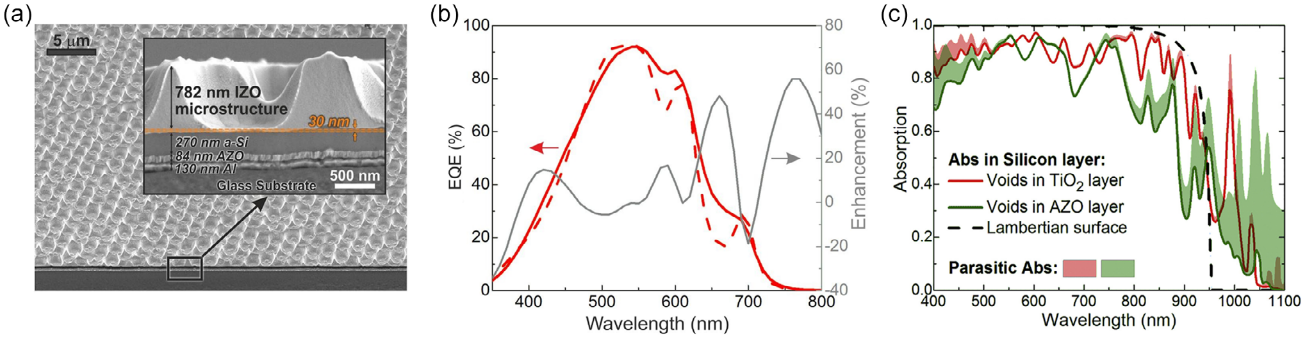

Figure 4. Morphology and optoelectronic (experimental and theoretical) performance of photonic honeycomb structures coated on a-Si:H solar cells. a) Scanning electron microscopy (SEM) cross sections of devices with a microstructured IZO layer acting as both transparent front contact and LT coating on the a-Si:H absorber. b) EQE spectrum (solid red line) obtained for the a-Si:H cell with a 190 nm flat IZO layer separating the photonic-structured IZO from the absorber, and the respective enhancement (in gray) determined regarding the optimized planar counterpart (dashed red line). Reprinted with permission.[83] Copyright 2020, Elsevier. c) Simulated absorption spectra of optimized hexagonal voids array composed of different metal-oxides, compared to the theoretical Lambertian formalisms, for 300 nm-thick a-Si absorbers. Reprinted with permission.[123] Copyright 2018, Elsevier.

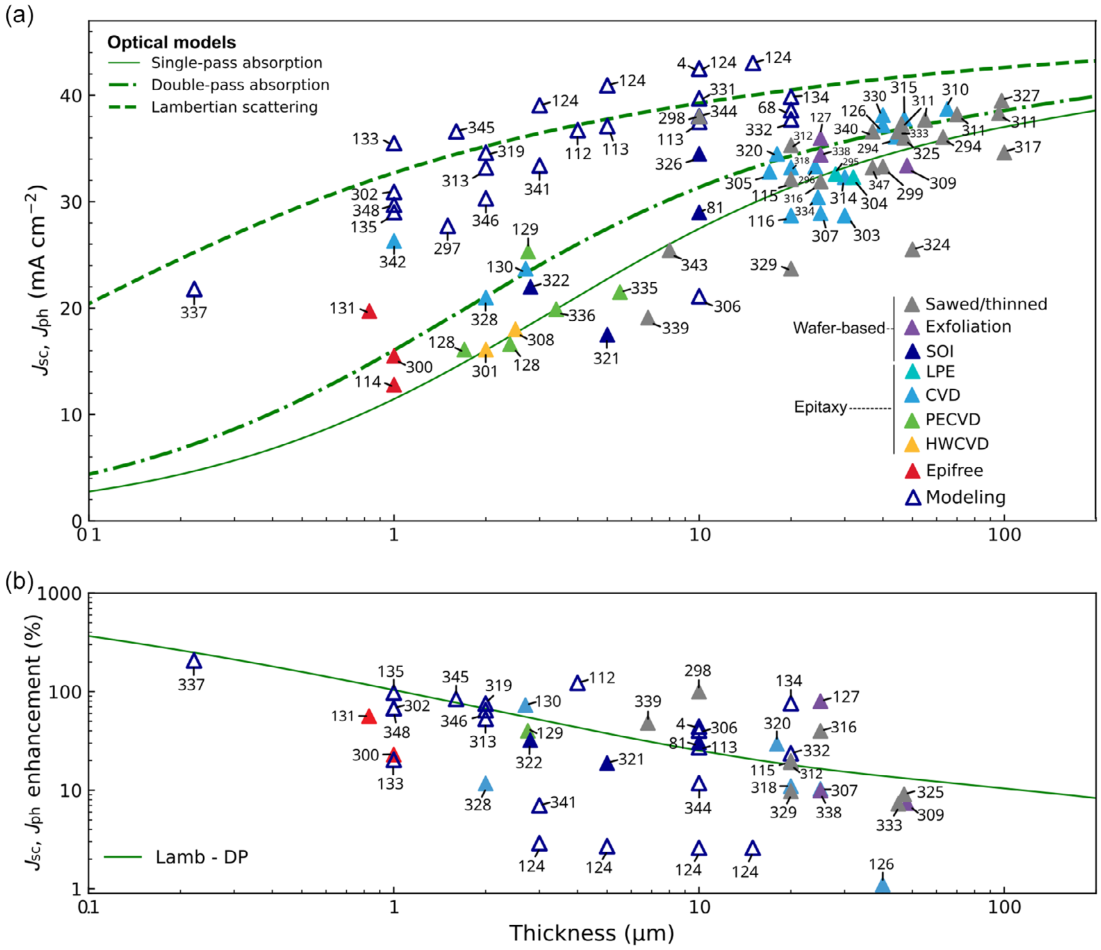

Figure 5. Overview of photocurrent values of Si-based solar cells improved with photonic schemes, reported by key contributions referenced in the plotted labels, in terms of measured short-circuit current density (J_{SC}) or simulated optical photocurrent (J_{PH}). a) J_{SC}, J_{PH} of thin ($20\,\mu m \leq t \leq 100\,\mu m$), and ultrathin (<20 μm) c-Si solar cells as a function of the absorber thickness. Results are represented by filled colored triangles, categorized based on the growth method (wafer-based, epitaxy, or others).[4,68,80,112–116,124,126–131,133–135,294–349] Open triangles denote J_{SC} and J_{PH} values obtained from numerical calculations and absorption measurements. All reported values are compared to the reference models defined in the Supporting Information: single-pass, double-pass, and Lambertian scattering models, represented by dash-dot, dash, and solid lines, respectively. We extended the data provided by Massiot et al.[76] to the present. b) The relative enhancements of J_{SC} and J_{PH}, compared to planar counterparts (based on the double-pass absorption model), are plotted as a function of the thickness of the c-Si absorber. These values are compared to the relative enhancement defined by the Lambertian scattering and double-pass absorption models (depicted by the full line, labeled as Lamb DP).

should also be given to cost-effective fabrication techniques combined with submicrometric textures featuring novel geometries. For instance, PECVD allows the fabrication of thinner absorbers, as shown by Cariou et al.[128] This work reports c-Si heterojunction cells whose c-Si thickness range between 1 and 2.4 μm. Besides a planar optimized ITO front ARC layer and an Al back reflector, no other LT schemes were employed in the device architecture. Consequently, the device with the highest absorber thickness (2.4 μm) attained 16.6 mA cm^{-2} of J_{SC} and 7.0% of efficiency. A subsequent work of Gaucher et al.[129] reported solar devices with an absorber thickness of 2.8 μm, where the c-Si absorber was epitaxially grown by low-temperature PECVD and transferred onto a glass substrate via anodic bonding and mechanical cleavage. These devices featured 2D periodic arrays of submicrometric inverted pyramids fabricated through NIL and wet etching (**Figure 6**a). The inverted nanopyramids minimized reflection via index matching between the air medium and the Si absorber and increased the path length of low-energy absorbed photons, which resulted in a J_{SC} of 25.3 mA cm^{-2} (Figure 6b) corresponding to a 40% J_{SC} gain (Figure 5b) relative to the double-pass absorption, underscoring the potential of this approach to improve the optical performance of ultrathin devices. However, it is worth mentioning the J_{SC} was hampered by the lack of proper optimization of both front and back TCO layers that increased the series resistance. Alternatively, the c-Si absorber can be fabricated via epitaxial growth, as reported by Xue et al.[130] In this work, a 2.7 μm–thick ultrathin c-Si cell integrated a front array of inverted nanopyramids for LT in conjunction with a NiO_x hole-selective layer (HTL) to reduce contact recombination. The resulting 23.7 mA cm^{-2} of

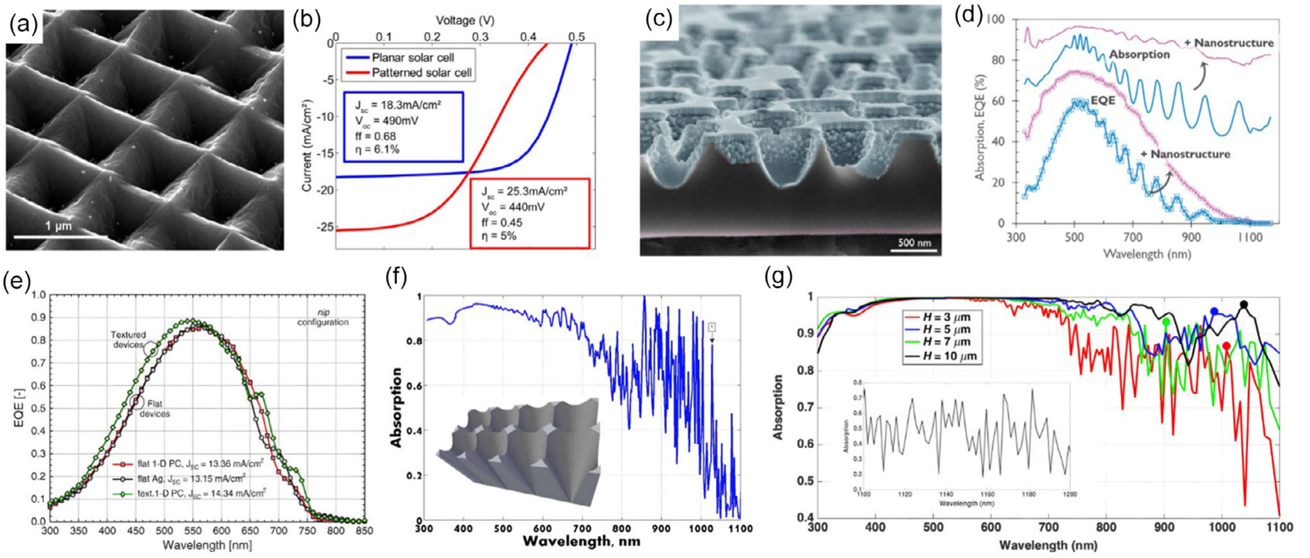

Figure 6. Morphology and optoelectronic performance of state-of-the-art thin c-Si solar cells (<10 μm of absorber) coupled with front photonic elements. a) SEM images showing the array of inverted pyramids fabricated via UV–NIL and wet etching. b) *J–V* curve of a 3 μm thick planar (blue) and patterned (red) c-Si solar cells on glass under one AM1.5 G illumination, with photovoltaic characteristics (J_{SC}, V_{OC}, fill factor, and PCE) in the inset. Reprinted with permission.[131] Copyright 2016, American Chemical Society. c) Tilted cross-sectional SEM view of a 1.1 μm monocrystalline Si solar cell with nanostructured front side covered with ITO ARC/contact. d) EQE (with symbols) and absorption spectra of optimal cells, highlighting the optical improvement brought forth by the nanostructures with arrows with respect to the planar counterparts (with optimized front ITO ARC). Reprinted with permission.[133] Copyright 2017, IOP Publishing Ltd. e) Measured EQE of the champion flat and textured n–i–p devices with the dielectric diffuse Bragg reflector (denoted 1-D PC, denoting 1D photonic crystal) and Ag back reflectors. The respective J_{SC} values are calculated from the EQE via convolution with the AM1.5 G irradiance spectrum. Reprinted with permission.[134] Copyright 2012, Elsevier. f) Absorption coefficient for slanted conical air pores in a free-standing bulk silicon film (with air above and below) for radius equals to 500 nm and pitch equals to 850 nm. A top view of the structure is shown in the inset. Reprinted with permission.[135] Copyright 2013, with permission from AIP Publishing. g) Absorption spectra of c-Si inverted-pyramid PC solar cells with height (*H*) indicated in the inset. The inset shows the computed absorption of the 10 μm-thick PC cell. Reprinted with permission.[126] Copyright 2019, American Physical Society.

J_{SC} approaches that of the work of Gaucher et al. (25.3 mA cm^{-2}). On the other hand, arrays of periodically arranged front parabolic voids present an alternative to conventional upright pyramids, as shown by Depauw et al.[131] Figure 6c illustrates the combination of submicrometric texturization, efficient passivation, and antireflection layers, resulting in enhanced LT toward the absorber and a 57% J_{SC} enhancement over the double-pass absorption model. Ultimately, the 0.83–μm-thick devices showed 19.7 mA cm^{-2} of J_{SC} and 8.6% of PCE, capitalizing on the absorption gains provided by the front textured surface, as shown in the EQE spectra of Figure 6d.

Despite extensive research efforts, a notable gap persists between effective LT in experimental studies and predictions from Lambertian models for thin/ultrathin devices, largely due to pronounced front reflection losses and parasitic absorption in the textured rear mirror. An advance approach to effectively overcome the rear parasitic absorption is to deposit a stack of alternating layers of materials with different refractive indices onto thin/ultrathin devices, in addition to reflect all nonabsorbed photons back to the absorber for potential absorption, thereby improving solar cell efficiency. This technique relies on constructive interference generated by the interaction of reflected longer wavelengths and the rDBR acting as a high-quality reflector, effectively preventing rear parasitic absorption.[76] Ingenito et al.[68] coupled double-side textured c-Si wafers with rDBRs, achieving up to 99.8% of the Lambertian absorption limit, marking the state of the art for such technology. However, while rDBRs proved beneficial for Si solar cells with flat back surfaces, they were found to be detrimental for solar cells with rear textures, where a simple silver rear mirror was preferred. This observation aligns with previous research findings[132] (Figure 6e), suggesting that while rDBRs offer potential for minimizing rear parasitic absorption, further investigation is needed to justify their integration into LT schemes.

Potential LT architectures for ultrathin c-Si devices, designed to surpass Lambertian model limits, are primarily explored through numerical simulations. These innovative designs encompass various structures, such as slanted cones,[133] inverted pyramids,[124,134] or quasirandom structures,[135] targeting c-Si absorber thicknesses between 1 and 10 μm. For instance, Eyderman et al.[133] demonstrated how a 1 μm ultrathin c-Si photonic crystal (PC) with slanted conical pores (represented in the inset of Figure 6f), paired with a silver rear mirror, resulted in ≈20% J_{SC} enhancement compared to the planar counterpart. The periodicity of these photonic elements induces intense resonant modes that increase the absorption in such thin absorbers. Consequently, the efficacy of Si slanted cones solar cell architecture is grounded on the combination of antireflection and LT properties. A later work of the same authors[4] proposed a near-perfect LT scheme for the wavelength range of 400–1100 nm, consisting of square lattices of inverted c-Si pyramidal textures, with a pitch of 1.3–2.5 μm. For a 10 μm c-Si slab, the J_{ph} reached 42.5 mA cm^{-2}, which is close to the J_{ph} maximum defined by the Lambertian limit (43.5 mA cm^{-2}). Similarly, Bhattacharya et al.[124] achieved PCEs ranging between 29% and 30% with thin c-Si solar cells endowed with inverted c-Si pyramidal textures (Figure 6g). Interestingly, the J_{ph} reported in this work exceeds those of the Lambertian limit for each absorber thickness, because of wave interference-based LT effects not accounted in the geometric optics domain of the Lambertian absorption model. When accounting for electrical losses, including sheet resistance and surface recombination, an inverted micropyramidal c-Si cell with an optimized absorber thickness of 10 μm, incorporating bulk light doping and heavy doping near the Si top and rear surface, exhibited 29.7% of efficiency, V_{OC} of 0.80 mV, J_{SC} of 45.5 mA cm^{-2}, and FF of 0.87. The attained efficiency is comparable to a hypothetical 110 μm Lambertian LT cell with 29.6% of efficiency.[72] It is noteworthy to consider that employing the simplified cell architecture as utilized in the aforementioned simulations may potentially lead to an overestimation of the predicted short-circuit current. Nevertheless, research guided by numerical methods not only paves the way for new investigation lines, but also helps to minimize material and processing costs while setting upper boundaries for attainable J_{SC} values and extending our understanding of optical mechanisms induced by advanced LT approaches.

3.2. Perovskite Absorbers

Over the past decade, PSCs have shown remarkable potential to offset or complement Si-based PV, by consistently setting high-efficiency records and offering potential advantages such as enhanced power-to-weight ratio and tunable bandgap. This potential has sparked interest in integrating them into tandem systems alongside established PV technologies, such as c-Si solar cells. In fact, motivated by various factors affecting their environmental stability on Earth atmospheric conditions, there has recently been an increasing interest in testing their performance in space environment. Their integration into the space sector is currently supported by: 1) recent economic predictions that foresee massive cost reductions ($10–$20 billion USD) if perovskite PVs contribute to the incoming LEO PV market growth[27] and 2) increasing radiation tolerance, as recently reported.[27,31–34,51,94,136–140] Yet, PSCs face high-priority challenges, such as reduced environmental stability, that hinder their competitiveness with standard PV technologies, and pronounced bulk recombination, primarily given by its polycrystalline film structure, whose grain boundaries constitute recombination sites.[141–143] For that, advanced LT schemes enable the creation of physically thinner yet optically denser devices, which can minimize recombination losses in the perovskite grains, while also endowing PSCs with greater mechanical flexibility, hence broadening their market applicability.

The benchmark of the J_{SC} values of photonic-managed single-junction PSCs is shown in **Figure 7**a. This includes single-pass, double-pass, and Lambertian absorption models based on standard methylammonium lead iodide ($CH_3NH_3PbI_{3(1-x)}Cl_{3x}$, MAPI), *n*, and *k* spectra (provided in Supporting Information) for further analysis. Figure 7b illustrates the relative J_{SC} enhancements with respect to a PSC coupling a front optimized ARC and rear reflector against its planar counterpart—double-pass absorption model, as a function of the perovskite layer thickness. In addition, these enhancements are also juxtaposed with predictions by the Lambertian absorption model over the double-pass model (Lamb DP). The majority of J_{SC} values for the optically enhanced single-junction PSCs lie close or below those of the single-pass absorption model, showcasing minimal absolute J_{SC} (Figure 7a) or J_{SC} improvements (Figure 7b) from the integration of such LT schemes. This underscores the necessity for advanced and electrically harmless LT schemes.[7,144,145]

Distinct photonic strategies have been proposed to improve LT in single-junction PSCs. These include, for instance, microlens or nanocone arrays,[146] nano- and micropatterned charge transport layers,[147,148] fiber array-based antireflection front electrodes,[149] nanophotonic front[150] and back electrodes,[151] and randomly structured[152] or corrugated substrates.[153] Additionally, surface plasmon resonance strategies, such as integrating plasmonic NPs[154,155] or light grating-coupled plasmons,[156] have been reported. These approaches circumvent texturization processes that can increase carrier recombination, thus preserving the performance of these layers. Vasilopoulou et al.[157] reported ultrathin-film PSCs with photonic nanostructures mimicking the adaxial epidermis of flower petals (**Figure 8**a) for $(CsPbI_3)_{0.05}[(FAPbI_3)_{0.83}(MAPbBr_3)_{0.17}]_{0.95}$ PSCs. These biomimetic LT structures, fabricated via UV–NIL on glass, demonstrated a correlation between antireflection effect plus transmittance and the aspect ratio of the nanostructures. Higher aspect ratios (tested up to 0.8, corresponding to 360 nm of height and 450 nm of basis diameter) reduced the reflectivity measured at 80° incidence angle of bare glass substrates from ≈38% down to ≈4%, and provided the highest broad transmittance (250–1100 nm). Moreover, the biomimetic nanostructures exhibited hydrophobicity on the top glass surface, conferring water repellency to the ultrathin devices. Aging tests showed a slight absolute decrease in PCE of ≈5% for the flower-based devices and ≈15% for the plain cells (unencapsulated) after 1000 h under a nitrogen atmosphere, as evidenced in Figure 8b. The ultimate J_{SC} of the flower-based cells capitalized mainly on the high-quality of the perovskite absorber layer, since only ≈6% of J_{SC} was contributed by the integration of the biomimetic nanostructures. Wei et al.[151] also took advantage of NIL to incorporate moth-eye nanostructures into the rear metal electrode (Figure 8c). Compared to the flat reference cell with a methylammonium lead halide perovskite ($CH_3NH_3PbI_{3-x}Cl_x$) absorber, the moth-eye-patterned devices achieved a 14.3% improvement in J_{SC}, achieving in a PCE of ≈16.3% without decreasing V_{OC} and FF (Figure 8d). The integration of the moth-eye LT schemes contributed an increase up to 14.3% in J_{SC} due to strong light scattering, independent of light polarization (Figure 8e). Lastly, the pioneering work of Kim et al.[158] showcased record J_{SC} improvements, aligning with Lamb–DP enhancement predictions (see Figure 7b). Utilizing front hemisphere TiO_2 PCs (Figure 8f) as an electron transport layer (ETL) in mesoscopic MAPI PSCs for a superstrate configuration yielded significant optoelectronic gains, with a 15.2% PCE (50% improvement compared to the planar ETL reference) and ≈48% J_{SC} enhancement. The EQE spectra of Figure 8g

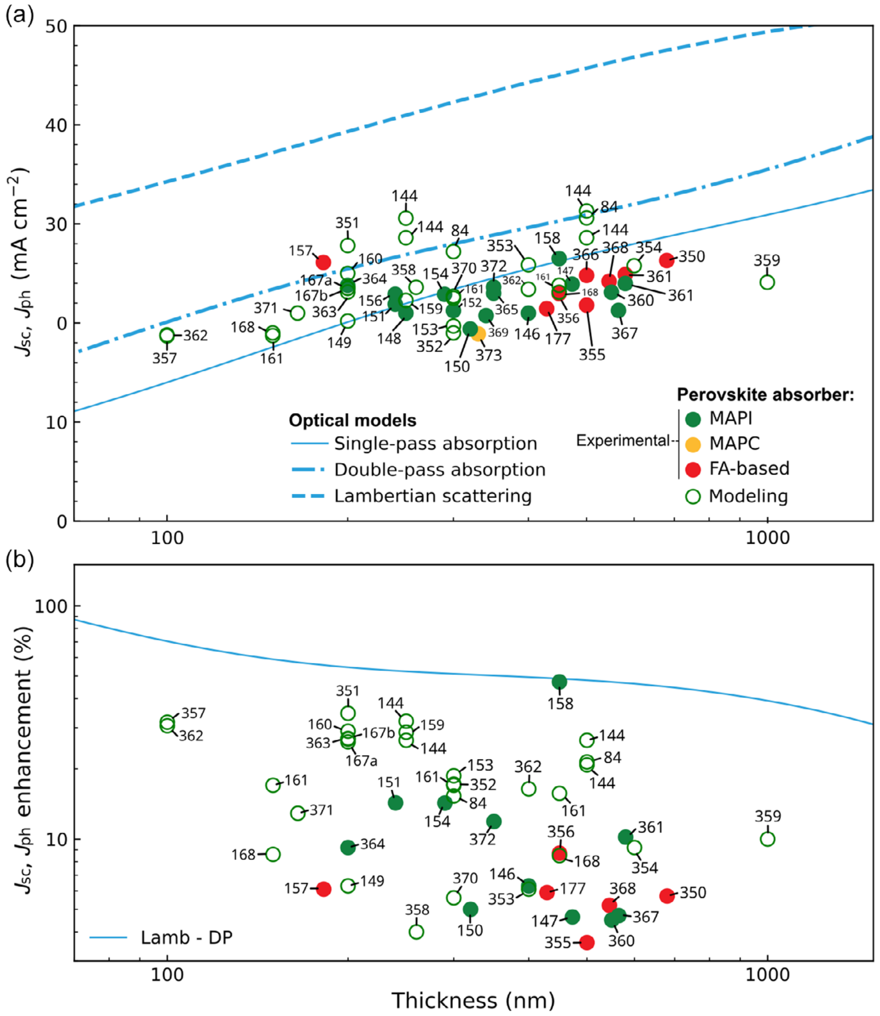

Figure 7. Overview of photocurrent values of PSCs improved with photonic schemes, reported by key contributions referenced in the plotted labels, in terms of measured short-circuit current density (J_{SC}) or simulated optical photocurrent (J_{PH}). a) J_{SC}, J_{PH} of thin PSCs as a function of the absorber thickness. Experimental results are represented by filled colored triangles, organized by perovskite absorber type, including methylammonium lead iodide (MAPI), methylammonium lead iodide chloride-doped (MAPC), and formamidinium (FA)-based ones.[84,144,146–154,156–161,167,168,177,350–373] Open circles denote J_{SC} and J_{PH} values obtained from numerical calculations and absorption measurements. All data points are compared against reference models outlined in the Supporting Information, with standard MAPI n and k spectra considered in this analysis. b) Respective J_{SC}, J_{PH} relative enhancements determined with respect to the planar counterparts (double-pass absorption model) as a function of the perovskite absorber thickness. All values are compared to the relative enhancement of the Lambertian scattering and double-pass absorption models (Lamb DP, full line).

depict the adjustment of the photon path by simultaneously scattering light and providing a smoother optical path (in terms of refractive index) to the vis–NIR photons toward the perovskite absorber. Moreover, these photonic elements facilitated the movement of the generated charges from the perovskite layer to the ETL (Figure 8h).

Luo et al.[153] combined NSL with RIE to fabricate corrugated glass substrates for the subsequent deposition of MAPI PSCs (Figure 8i). Maintaining the corrugated morphology up to the HTL/perovskite interface resulted in higher shunt resistance for the optically enhanced devices compared to the planar ones, leading to increased V_{OC}, FF, and J_{SC} as seen in the respective J–V curve of Figure 8j. Also, considering the improved broad antireflection effect (Figure 8k), the PCE rose from 8.7% of the planar devices to ≈13.0% for the corrugated ones.

Numerical simulations play a central role in benchmarking thin photonic-managed devices and providing crucial insights into the performance of complex LT schemes for PSCs. One such example is demonstrated in the work of Jangjoy et al.[159] where metallic Au, Cu, Ag, or Al clusters of NPs with various geometries were embedded in conventional PSCs with 250 nm MAPI absorbers (**Figure 9**a). Optimal cluster designs, coated with a thin SiO_2 dielectric for enhanced chemical and thermal stability, exhibited a notable gain of 28.7% in J_{ph}, compared to perovskite pristine solar cells, reaching 22.3 mA cm^{-2}. This enhancement stemmed from intense resonant modes surrounding the NPs within the absorber, particularly benefiting wavelengths at 350, 440, and 510 nm (Figure 9b). Accounting for parasitic absorption, the resulting V_{OC}, FF, and PCE were respectively 1.0 V, 0.87, and 20.79 mA cm^{-2}. Subsequent research by

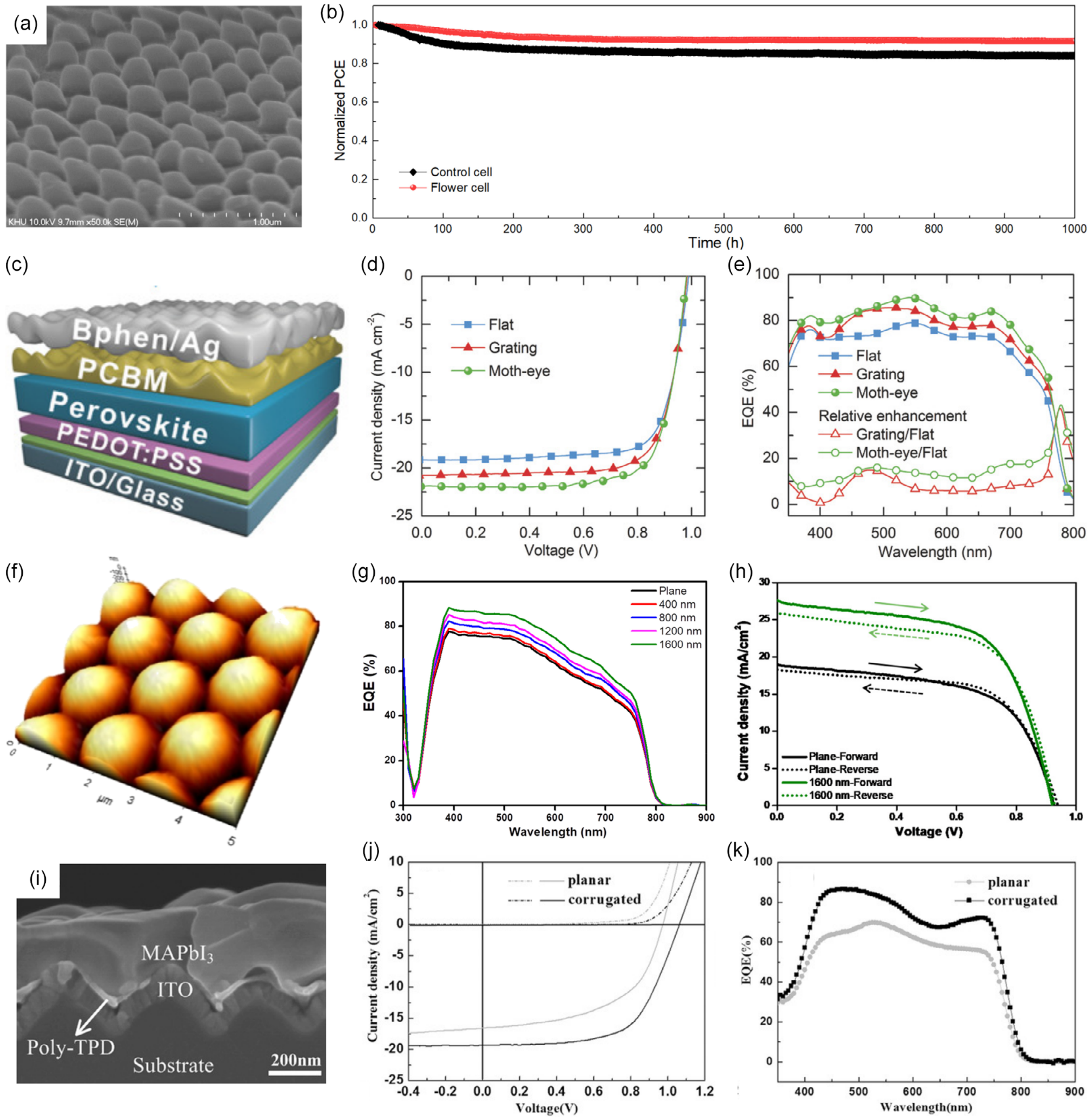

Figure 8. Optoelectronic performances of PSCs coupled with photonic LT approaches. a) Top view (top) and tilted (bottom) SEM images show the petal's adaxial epidermal layer test cells of wild *Ammi majus* in UV-curing adhesive (DYM 6-621). b) Stability study of PCEs of unencapsulated PSC devices over 1,000 h under a nitrogen atmosphere. Reprinted with permission.[159] Copyright 2022, Elsevier. c) Schematic of the fabrication process of nano-patterned $CH_3NH_3PbI_{3-x}Cl_x$ PSCs. d) *J*–*V* curves of flat, grating, and moth-eye patterned PSCs recorded under AM 1.5G illumination. e) EQE spectra of PSCs, and relative enhancement relative to the planar counterpart. Reprinted with permission.[153] Copyright 2017, John Wiley and Sons. f) AFM images of the TiO_2 mesoporous layer with 1600–nm sized pattern. g) The EQE spectra of PSCs with five different pattern size. h) *J*–*V* curves of forward scan and reverse scan for the PSC of flat and the optimal PSC with 1600 nm sizes ETL. Reprinted with permission.[160] Copyright 2019, John Wiley and Sons. i) Cross-section SEM images of perovskite film on corrugated substrates. j) *J*–*V* curves, and k) EQE spectra of planar and corrugated PSC test devices. Reprinted with permission.[155] Copyright 2016, John Wiley and Sons.

Jangjoy et al.[160] introduced $SiO_2/Au/SiO_2$ or $SiO_2/Ag/SiO_2$ triple core-shell spherical plasmonic NPs into a 200 nm MAPI PSC (Figure 9c). This study revealed a 29% increase in J_{ph} for PSCs embedded with $SiO_2/Au/SiO_2$ (2.5 times greater than that generated by purely metallic NPs), emphasizing significant resonance modes within the "useful" wavelength range of the MAPI

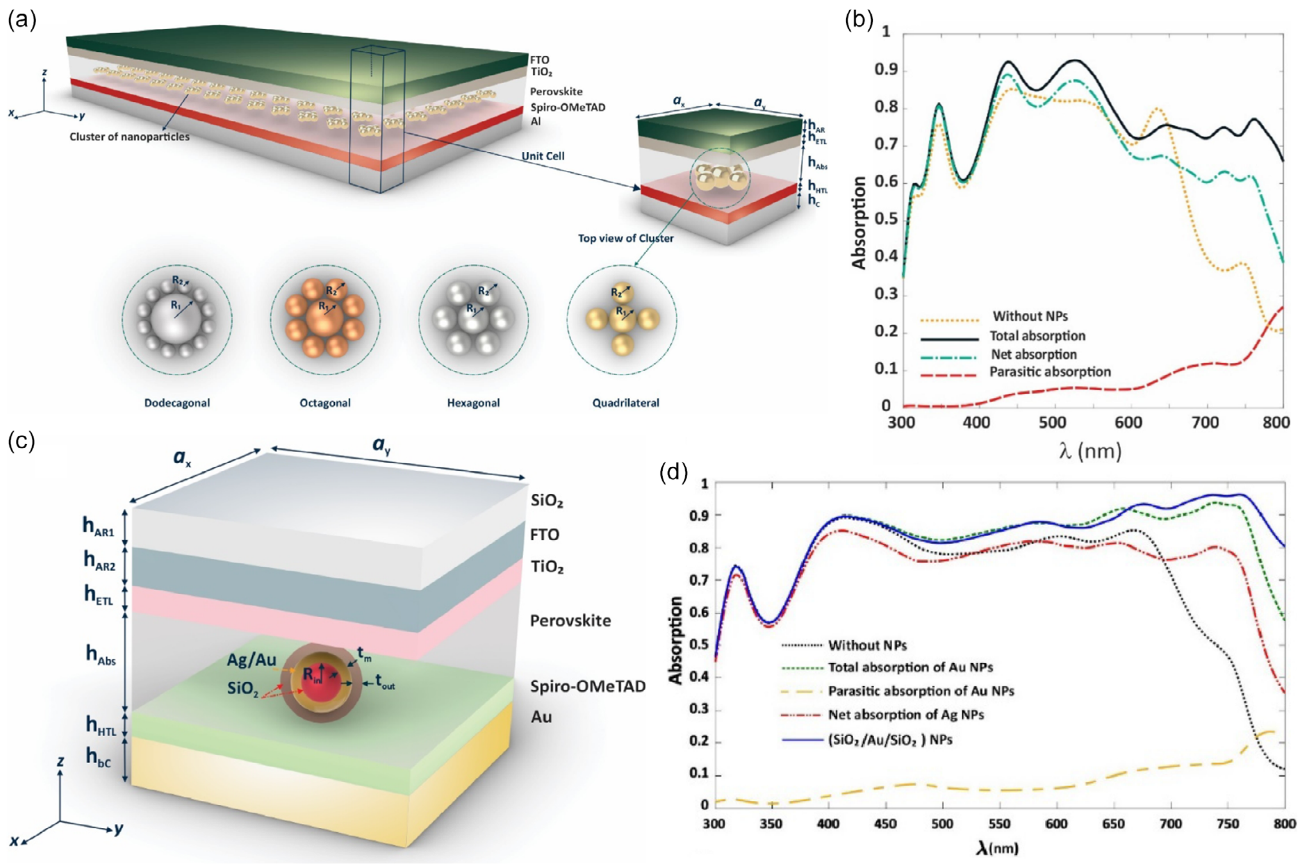

Figure 9. LT performance of PSCs embedded with NPs. a) Schematic of PSC architecture with four different NP arrangement: dodecagonal, octagonal, hexagonal, and quadrilateral. b) Total, net, and parasitic absorption diagram for PSCs endowed with Al cluster NPs with optimal quadrilateral arrangement, with respect to the pristine counterpart (without embedded NPs). Reprinted with permission.[159] Copyright 2022, Elsevier. c) 3D schematic of proposed ultrathin-film halide PSC embedded with core/shell/shell NPs. d) Absorption spectra of perovskite absorber with Ag or Au spherical NPs and core/shell NPs, with respect to the pristine counterpart (without embedded NPs). Reprinted with permission.[160] Copyright 2023, Optica Publishing Group.

PSCs, Figure 9d). Electrical simulations of PSCs embedded with optimal $SiO_2/Au/SiO_2$ yielded 1.06 V V_{OC}, 25.0 mA cm^{-2} J_{ph}, 0.87 FF, and 23.0% PCE. The negligible contribution of the very thin (40–60 nm) metallic layer to parasitic absorption warranted its exclusion from the J_{ph} assessment.

Semispherical structures with long-range periodicities have emerged as promising strategies to enhance light harvesting in thin-film PSCs. Hossain et al.[161] evaluated the optoelectronic performance of MAPI PSCs with absorber thicknesses ranging from 150 to 450 nm, featuring front multilayered nanodomes or nanoholes (**Figure 10**a). As a result of light incoupling and light scattering effects, arising from the front $MgF_2/TCO/TiO_2$ nanodomes (Figure 10b), the PCE increased by ≈14% for the nanoholes scheme, closely mirroring the gain in J_{SC} (≈16%). The J_{SC} remained approximately constant under light incidence angles ranging between 0° (normal light incidence) and 40° (oblique light incidence). In the study of S. Haque et al.[144] standard MAPI PSCs with 500 and 250 nm thin perovskite absorber layers, coupled with front TiO_2 photonic structures (voids or semispheroidal domes) conformally covered by an ITO front contact (Figure 10c), demonstrated enhanced light absorption for wavelengths above 600 nm[162,163] and effective UV light blocking (300–400 nm, Figure 10d–e). This architecture, mitigating photocatalytic activity at the ETL (TiO_2)/perovskite interface, suggests prolonged device stability and potential applicability for perovskite-based space PVs due to its resilience to incident UV radiation.[164–166] A subsequent work of S. Haque et al.[84] validated that photonic-structured PSCs (300 and 500 nm-thick perovskites) with a superstrate configuration (Figure 10f) effectively translate optical gains into power generation (Figure 10g). Structuring all interfaces led to an increase in J_{ph} from 19.7 mA cm^{-2} for the planar configuration to 24.8 mA cm^{-2} for the proposed configuration, corresponding to a relative enhancement of ≈25.9% (Figure 10h). Tooghi et al.[167] proposed a similar all-structured MAPI PSC (Figure 10i) to maximize efficiency. The simulated convex nanostructures reduced front reflection via effective index matching, trapped incoupled photons within the device, mainly for wavelengths >500 nm (Figure 10j), and facilitated carrier extraction, thereby increasing light absorption within the absorber. Moreover, the electromagnetic field was found to be further concentrated in the absorber due to intense surface plasmon resonance modes induced by the structured Au contact. As such, the J_{ph} increased from 18.3 mA cm^{-2} for the planar counterpart to 23.5 mA cm^{-2}

(≈26% of increase) for the proposed all-structured PSC. Ultimately, a PCE increase of ≈34% (from 14.6% to 19.5%) was observed due to the additional increase in V_{OC} (≈4%). This work underscores the benefit of structuring all layers, including the metallic contact; however, a contrasting perspective is presented by Qarony et al.[168] In their work, the authors compared the optoelectronic performance of three different LT designs: a) ZnO-structured PSCs, b) all-structured PSCs, and

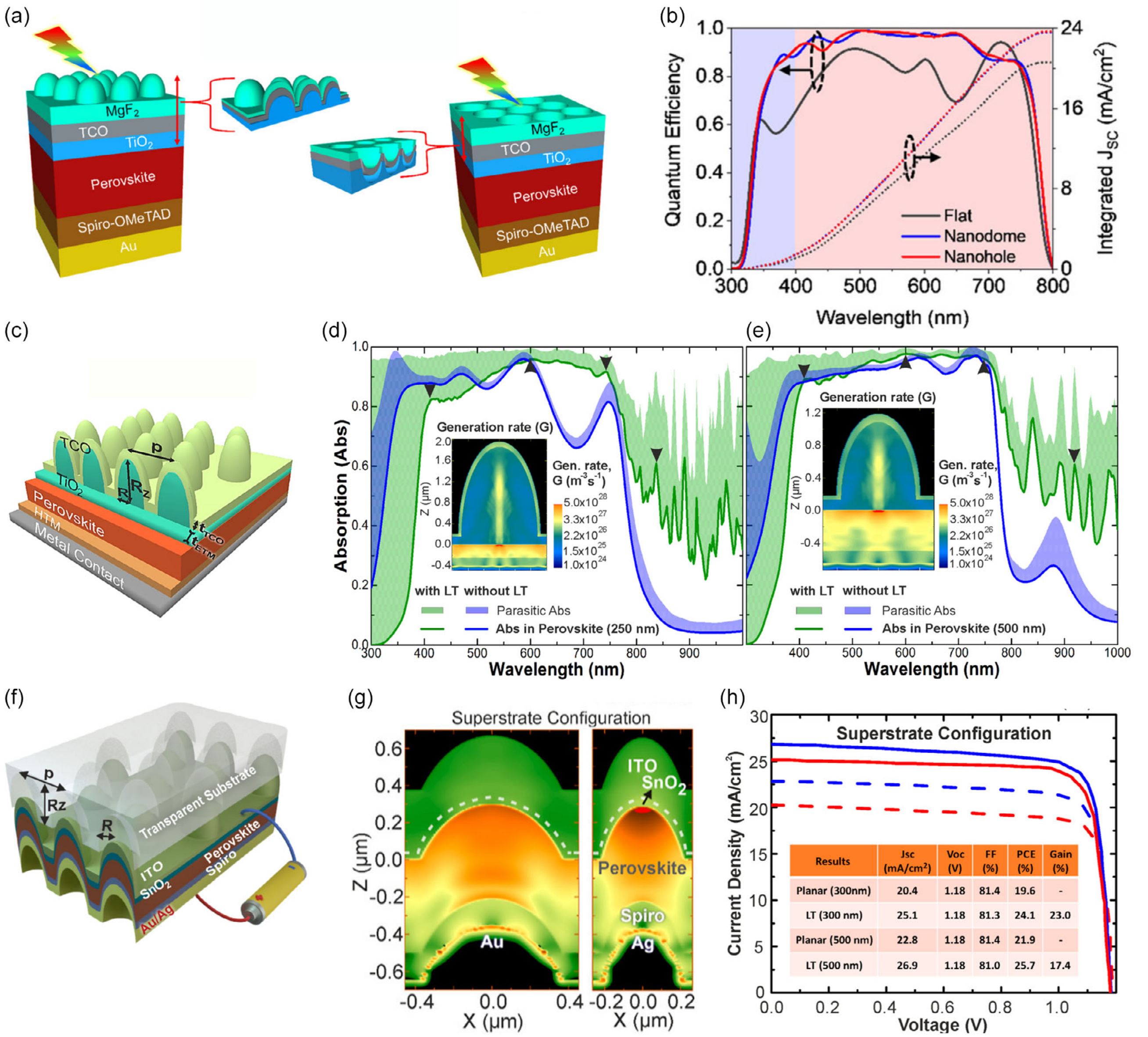

Results	Jsc (mA/cm²)	Voc (V)	FF (%)	PCE (%)	Gain (%)
Planar (300nm)	20.4	1.18	81.4	19.6	-
LT (300 nm)	25.1	1.18	81.3	24.1	23.0
Planar (500 nm)	22.8	1.18	81.4	21.9	-
LT (500 nm)	26.9	1.18	81.0	25.7	17.4

Figure 10. Analysis of the optoelectronic performance of PSCs coupled with cutting-edge photonic elements. a) Schematic of MgF_2, TCO, and TiO_2 structured layers, with LT domes (left) and voids (right). b) Spectra of QE (external) and integrated J_{SC} between planar and textured PSCs for the 150 nm-thick perovskite absorber. Reprinted with permission.[163] Copyright 2021, John Wiley and Sons. c) Sketch of PSCs endowed with LT features composed of hexagonally arranged TiO_2 domes conformally covered with a TCO. Geometrically, the radii are denoted by R, along the in-plane direction, and R_Z, along illumination axis, pitch is denoted by p, and tTCO and tETL respectively denote the thickness of the TCO and of the ETL. d,e) Absorption spectra of the optimized LT domes, composed of half-spheroidal domes (green), and of a cell with an optimized planar ARC (blue), for perovskite absorber layers with thicknesses of d) 250 nm and e) 500 nm. Reprinted with permission.[146] Copyright 2019, Elsevier. f) Schematic of all-structured PSCs in superstrate configuration with Au/Ag metal contacts. g) Total generation rate, G, along the xz cross-sectional plane of the structures. h) Simulated J–V curves of the photonic-structured PSCs with the conventional 500 nm-thick perovskite layers for superstrate configurations, with respective photovoltaic characteristics (J_{SC}, V_{OC}, FF, PCE, and J_{SC} gain determined with respect to the planar counterpart). Reprinted with permission.[84] Copyright 2022, American Chemical Society. i) Schematic of the proposed LT structures (left) and normalized electric field and respective color bar for at the wavelength of 800 nm (right). j) Normalized absorption spectra of the active layer in the ultrathin HTL structure with and without nanostructures (all-structured design). Reprinted with permission.[350] Copyright 2020, Springer Nature. k) QE spectra for the proposed PSC design: Structure A) ZnO-structured PSCs, Structure B) all-structured PSCs, and Structure C) PSCs with structured layers except for the rear reflector. Reprinted with permission.[351] Copyright 2018, John Wiley and Sons.

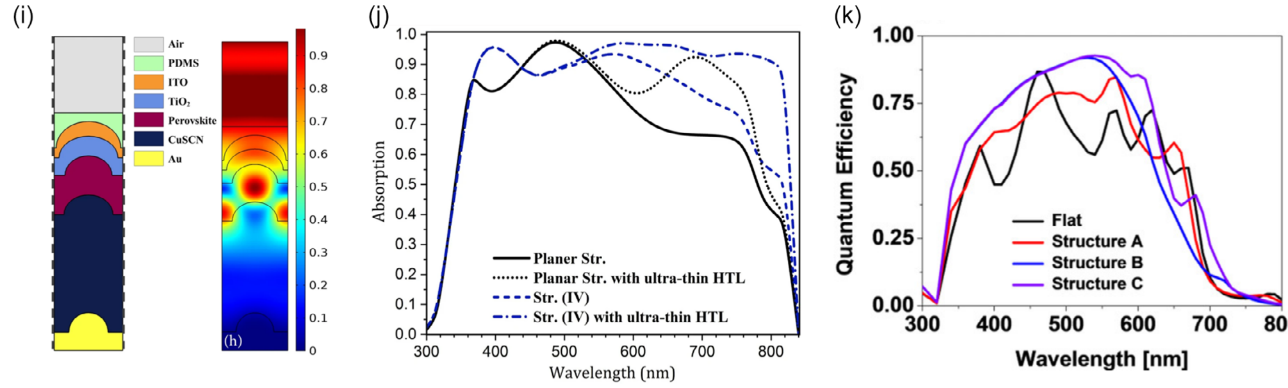

Figure 10. Continued.

c) PSC with structured layers except for the rear reflector. The all-structured design exhibited intense parasitic absorption in the rear HTL (NiO_2). These parasitic losses due to plasmonic resonances outweighed the increase in light incoupling, ultimately limiting the J_{ph} and PCE of the proposed device (Figure 10k). The other proposed cell designs performed similarly, achieving an absolute J_{ph} increase of 1.5 mA cm^{-2} (≈9% of relative enhancement) from 17.5 mA cm^{-2} for the planar counterpart and 19.0 mA cm^{-2} for each remaining design.

3.2.1. Photonic-Enhanced Flexibility of Perovskite Solar Cells

Ensuring the optimal balance between mechanical flexibility and lightweight properties is another crucial aspect for deploying PSCs in space applications. Despite extensive coverage of flexible and high-efficiency PSCs in recent reviews, there is a clear lack of emphasis on optimizing LT schemes for photon absorption maximization.[169–176] The prevailing focus remains on technological aspects like fabrication method refinement and compatibility testing. However, to fully leverage the potential of thin and flexible devices, efforts must address the critical trade-off of reduced power output associated with thinner absorbers.

Several recent studies have proposed approaches that ally flexibility with advanced LT schemes. One strategy involves structuring the rear ETL or HTL. For instance, Cong et al.[177] proposed bendable p–i–n PSCs with a NiO_x HTL coupled with nanopillar arrays, as represented in **Figure 11**a. These nanopillars served as nucleation sites, promoting the growth of larger, well-defined perovskite grains, scattering in-coupled photons, and facilitating hole transport and collection (Figure 11b). Consequently, the devices exhibited increased electrical power output, given the reduced series resistance. Mechanical characterizations revealed no cracking after 500 bending cycles, with the devices retaining 80% of their initial PCE. Ultimately, these unique bendable devices showcased 22.2 mA cm^{-2} of J_{SC} (Figure 11c) and ≈17% of efficiency. Rather than including NiO_x nanopillars, Wu et al.[178] deposited TiO_2 nanopillar arrays directly onto a planar TiO_2 layer (Figure 11d) using glancing angle deposition to avoid intermediate high-temperature sintering or lithographic processes. These nanopillars strongly adhered to the TiO_2 layer and facilitated electron extraction and collection. Interestingly, this approach also improved the mechanical flexibility of the PSCs, achieving 23.0 mA cm^{-2} of J_{SC} and 17.3% of maximum PCE, with ≈90% retention of PCE after 500 bending cycles (Figure 11e).

Another avenue involves structuring the metallic electrodes of PSCs, where the efficiency improvement of these devices hinges on a delicate balance between optical transparency and conductivity. Sun et al.[179] fabricated a front Ag periodic mesh (APM) for MAFACsPbIBr PSCs by NSL (Figure 11f). PSCs deposited on glass with a 20 nm flat Ag front electrode showed 8.0 mA cm^{-2} and ≈8.0% of PCE. By enhancing the transmittance of "useful" photons toward the perovskite absorber (Figure 11g), the PSCs with 14 nm-thick Ag meshes on PET achieved up to 20.2 mA cm^{-2} and ≈16.5% of PCE, retaining around 90% of the original efficiency. In a different approach, Li et al.[180] covered a front UV resin/Ag mesh hybrid electrode with PH1000, a PEDOT:PSS-based conductive polymer (Figure 11h). Not only the MAPI PSC with Ag/PH1000 electrode yielded a PCE of 14%, but also endured 5000 bending cycles, maintaining 95% of its initial efficiency. The performance of the PSCs with PET/Ag-mesh/PH1000 was found to be dependent on thermal annealing, benefiting the most from a 2 min annealing at 130 °C (with an absolute PCE increase from ≈7 to ≈13%). Additionally, the photocurrent decay time at short-circuit condition decreased from 0.65 ms, for a PSC with glass/ITO rigid substrate, down to 0.42 ms for the flexible device, indicating a reduction of the charge carrier extraction time of 1.5 times (Figure 11i). Furthermore, Li et al.[181] fabricated Cu nanostructured meshes on PET substrates as an alternative to Ag meshes. The cells with Cu/PH1000 electrodes achieved a maximum PCE of 13.6%, retaining 90% of the initial PCE after 1000 bending cycles at a bending radius of 5 mm. In turn, Jin et al.[182] fabricated Cr/Au grids embedded on EG-doped PEDOT:PSS matrices onto a colorless polyimide-coated NOA63 substrate. The cells with front structures electrode achieved a PCE of 12.7%, maintaining 93% of the original PCE after 2000 bending cycles at a bending radius of 1.5 mm.

4. Light-Trapping Schemes for Perovskite-on-Silicon Tandem Solar Cells

Two-terminal perovskite-on-silicon tandem solar cells (2T-PSTSCs) are regarded as a promising competitor to other

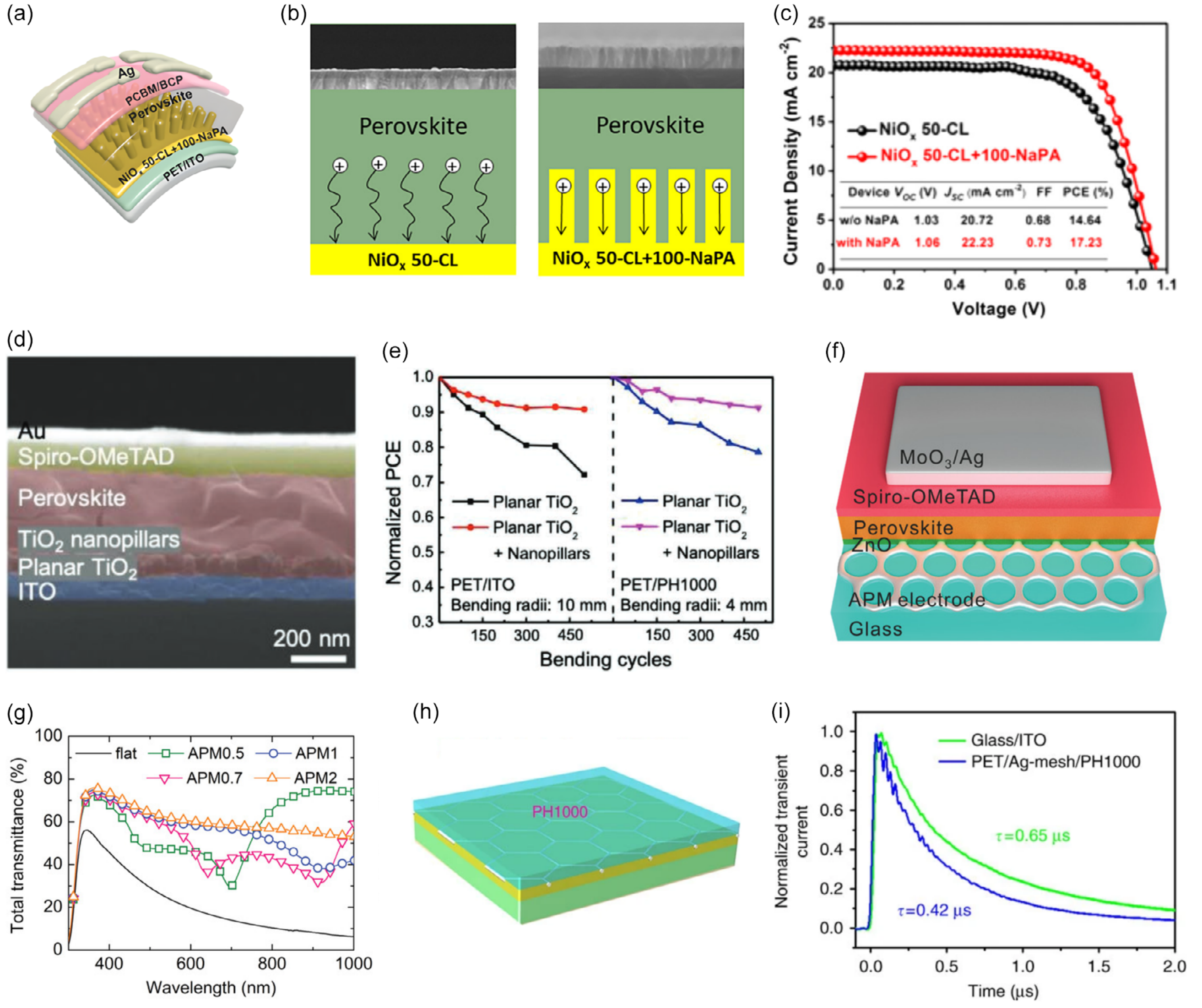

Device	V_{OC} (V)	J_{SC} (mA cm^{-2})	FF	PCE (%)
w/o NaPA	1.03	20.72	0.68	14.64
with NaPA	1.06	22.23	0.73	17.23

Figure 11. Performance and stability improvements of flexible PSCs via advanced photonic schemes. a) Schematic of PET/ITO/NiO$_x$ "50-CL + 100-NaPA"/perovskite ($FAyMA_{1-y}PbI_{3-x}Cl_x$)/$PC_{61}BM$/BCP/Ag solar cell. b) Schematic of photogenerated hole transport in the PSCs hybridized with diverse HTLs of different heights of NaPA: "50-CL" (left) and "50-CL + 100-NaPA" (right). On top, SEM images(cross section) of the NiO$_x$ nanostructures are shown. c) J–V curve of the champion PSCs hybridized with "50-CL" (in black) and "50-CL + 100-NaPA" (in red), with respective photovoltaic characteristics (V_{OC},J_{SC}, FF, and PCE) in the inset table. Reprinted with permission.[354] Copyright 2019, American Chemical Society. d) Schematic illustration of the full device configuration to emphasize the photonic TiO_2 ETL, comprising a planar TiO_2 integrated with nanopillars. e) Normalized PCEs of the photonic ETL-based flexible devices measured after bending cycles for bending radii of 10 mm or 4 mm. Reprinted with permission.[180] Copyright 2021, John Wiley and Sons. f) Schematic PSC architecture, emphasizing the APMAPM perforated with hexagonal-close-packed nanoholes. g) Total transmission for flat Ag film and various APM electrodes coated with 40 nm-thick ZnO. Reprinted with permission.[181] Copyright 2019, John Wiley and Sons. h) Schematic of the proposed hybrid electrode (PET/Ag-mesh/PH1000). i) Transient photocurrent measurement of the proposed PSCs fabricated on the hybrid electrode (PET/Ag-mesh/PH1000, dark blue line) and on a conventional glass/ITO substrate (green line). Reprinted with permission.[182] Copyright 2016, Springer Nature.

emergent technologies, such as all-perovskite or perovskite–dyes tandems.[12] Yet, the fabrication of 2T-PSTSCs presents important constraints, mainly requiring the integration of the top perovskite subcell to fulfill three key objectives: preserving the optoelectronic quality of the bottom c-Si subcell and recombination layer; fabricating conformal perovskite subcells to maximize both antireflection and light-scattering effects for UV–vis–NIR and NIR photons, respectively; and generating a high current matching the c-Si bottom sub-cell with a V_{OC} close to the bandgap limit.[39,41,183,184] To that end, it is crucial to optimize the thickness and bandgap of the perovskite film in the top subcell. A bandgap of 1.73 eV is the optimum compromise to maximize the absorption of high-energy photons by the top cell, while allowing the bottom cell to capture lower-energy photons.[39] Lower or higher perovskite bandgaps are more prone to lead to a mismatch in current between the subcells, reducing the overall efficiency of the tandem.[183] For that, the perovskite film thickness must also be carefully optimized. Thin films can potentially enhance charge extraction and minimize recombination losses but may not absorb enough high-energy photons resulting in lower photocurrent.[184] Additionally, thin films are more susceptible to defects, which can affect device stability. Conversely, thicker films improve light absorption and photocurrent generation but can lead to higher recombination losses, current imbalance, and increased optical losses, thereby limiting efficiency.[41] In this section, the authors highlight the most reliable methods, architectures, and photonic strategies to optimize the efficiency of 2T-PSTSCs, with relevance to both terrestrial and space applications.

State-of-the-art monolithic 2T-PSTSCs have only been demonstrated on rigid, small-area substrates (≈1 cm^2, 33.9% PCE, under standard test conditions),[22] which pose challenges for space applications.[141,183] Several innovative approaches have been implemented to tackle these hurdles. First, to ensure compatibility with the bottom subcell, 2T-PSTSCs usually rely on low-temperature (<200 °C) perovskite deposition methods to prevent degradation of the bottom silicon heterojunction cells, which are chosen by its high V_{OC} and excellent NIR photon absorption.[185] Second, both the thickness and bandgap of the perovskite layer have been simultaneously adjusted to match the current between subcells (18–19 mA cm^{-2}).[41] Finally, further efforts have been brought forth to master the development of fully textured monolithic 2 T-PSTSCs, as discussed below.

The initial designs of 2 T-PSTSCs integrated front-side polished c-Si bottom cells to ensure the compatibility with commonly spin-coated perovskite layers, as shown in **Table 3**.[41] An early example, as reported in the pioneering work by Bush et al.[40] integrates cesium formamidinium (CsFA) lead halide perovskite on a c-Si heterojunction tandem cell (layers set in **Figure 12**a), achieving 23.6% of efficiency with rear-sided textured Si absorber. Despite this, the nonconformal layers led to major reflection losses and poor LT of the NIR photons, which are weakly absorbed by the c-Si bottom absorber, resulting in a J_{SC} of 18.7 mA cm^{-2}. These reflection losses amounted to

Table 3. Summary of the optoelectronic performance of PSTSCs endowed with distinct LT approaches considered in this review. The power-to-weight ratio only accounts for the weight of the solar cells, with detailed calculations and data available in the Supporting Information.

#	Ref/Year	LT strategy	Perovskite deposition method	Silicon wafer thickness [μm]	Power-to-weight ratio [W g^{-1}]	Improved optical mechanisms	V_{OC} [V]	FF	$J_{SC,top}$ [mA cm^{-2}]	$J_{SC,bot}$ [mA cm^{-2}]	$J_{SC,tandem}$ [m cm^{-2}]	PCE [%]
1	[40]/2017	Rear Si Textures	Spin coating	280	0.36	Light scattering	1.65	0.79	18.9	18.5	18.1	23.6
2	[186]/2018	Front Textured PDMS + Rear Si Textures	Spin coating	250	0.43	Antireflection	1.77	0.77	18.4	18.5	18.4	25.0
3	[187]/2018	Front LM foil + Front and Rear Si Textures	Coevaporation + Spin coating	260	0.40	Antireflection + Light scattering	1.97	0.79	20.2	18.9	18.5	25.5
4	[41]/2018	Front + Rear Si Textures	Coevaporation + Spin coating	260	0.39	Antireflection + Light scattering	1.79	0.73	20.1	20.3	40.4	25.2
5	[394]/2019	TCA + Front Si Textures	Spin coating	515	–	Antireflection + Light scattering	1.59	0.76	15.7	15.1	15.1	18.3
6	[395]/2019	Front Si Textures	Co evaporation + Spin coating	–	36.2 mW[a)]	Antireflection + Light scattering	1.74	0.75	20.0	19.7	19.5	25.4
7	[396]/2019	Inverted Textured PDMS	Two-step spin coating	–	–	Antireflection + Light scattering	1.75	0.74	17.4	16.7	16.8	21.9
8	[185]/2019	Rear Si Textured	Spin coating	260	0.43	Antireflection	1.78	0.78	20.7	17.9	17.8	24.8
9	[193]/2020	Front and Rear Si Textures	Spin coating + Coevaporation	265	0.46	Antireflection	1.73	0.73	19.8	19.8	19.8	25.1
10	[203]/2020	Front PDMS + Rear Si Textures	Blade coating	250	26.2 mW[a)]	Antireflection	1.82	0.75	19.3	19.4	19.2	26.2
11	[204]/2022	Front Si Sinusoidal Nanotextures + Rear Si Textures	Spin coating	270	0.47	Antireflection + Light scattering	1.90	0.81	20.5	19.8	19.8	29.8
12	[209]/2022	Front Black Si	Spin coating	270	0.44	Antireflection + Light scattering	1.80	0.82	20.2	19.4	19.3	28.5
13	[210]/2023	Front + Rear Si Nanotextures	Spin coating	270	–	Antireflection + Light scattering	1.70	0.69	18.0	18.2	18.8	22.1
14	[211]/2023	Front + Rear Si Nanotextures	Spin coating	265	0.47	Antireflection	1.85	0.78	20.2	19.7	19.7	27.4

[a)] Maximum Power Point; TCA-Transparent Conductive Adhesive.

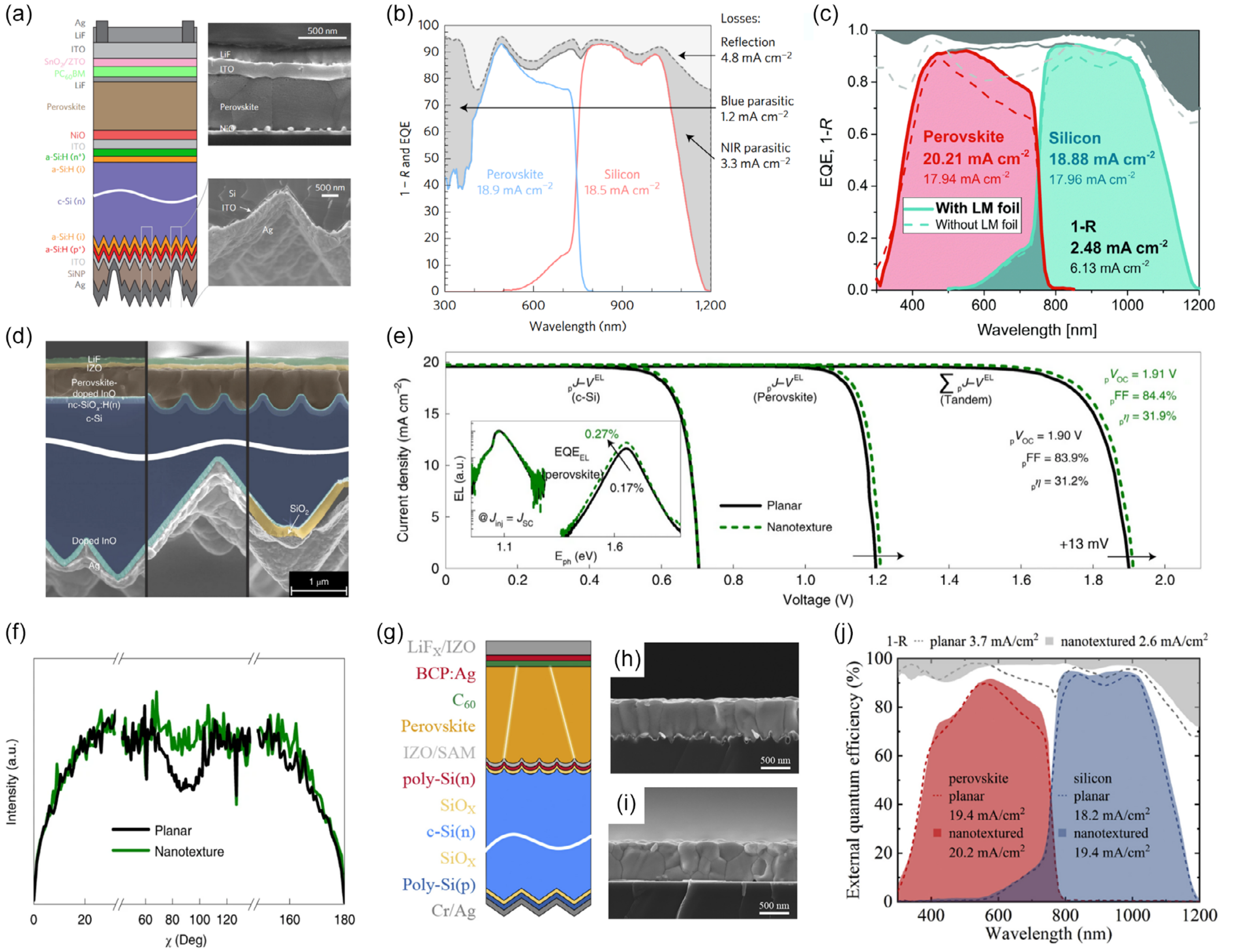

Figure 12. LT-enhanced PSTSCs. a) Schematic of the conventional planar perovskite/textured silicon tandem solar cell (left), cross-sectional SEM image of the Si-patterned rear side of the Si subcell before Ag rear mirror deposition (bottom right) and cross-sectional SEM image of the perovskite top subcell (top right). b) Total absorptance (*1*−*R*, where *R* represents reflectance; dashed gray line) is depicted alongside the EQE of the perovskite top subcell (solid blue line) and the silicon bottom cell (solid red line). The cumulative EQEs are represented by the solid gray line. Shaded areas in light and dark gray respectively denote reflection and parasitic absorption losses, with associated values provided. Reprinted with permission.[40] Copyright 2017, Springer Nature. c) EQE spectra of the fabricated tandems without and with the LM foil. The convoluted J_{SC} values as well as the current lost due to reflection are indicated. The red spectrum denotes perovskite EQE, blue denotes silicon EQE, and gray reflection losses. Reprinted with permission,[189] Copyright 2018, Royal Society of Chemistry. d) SEM cross sections of the front and rear side of planar (left), nanotextured (center), and nanotextured + rear DBR (right) PSTSCs. e) Subcell-selective electroluminescence measurements reveal the pseudo-*J*–*V* curve of planar and textured PSTSCs, distinguishing between the individual c-Si and perovskite subcells. The inset displays the electroluminescence spectra at $J = J_{SC}$. f) Averaged azimuthal (χ) intensity profiles of the (100) reflection of perovskite, determined from depth-resolved grazing-incidence wide-angle X-Ray scattering measurements over 39 incidence angles ranging from 0.1° to 2°. Reprinted with permission.[220] Copyright 2022, Springer Nature. g) Schematic of the nanotextured perovskite/silicon tandem solar cell architecture with front planar surface. h) Cross-sectional SEM images of the perovskite films grown on the nanotextured and i) on planar surfaces (*n*-Si/*n*-TOPCon/IZO/MeO-2PACz). j) EQE curves of the planar and nanotextured perovskite/silicon tandems. Total absorbance curves (gray shaded area) are also plotted for the optimal tandems. Reprinted with permission.[211] Copyright 2022, Elsevier.

4.8 mA cm^{-2} of the 9.3 mA cm^{-2} parasitic losses (as seen in the EQE spectra of Figure 12b). To reduce front-reflection losses, Bush et al.[186] later added a polydimethylsiloxane (PDMS) stamp with random pyramidal texture to improve index matching between air and the top layer, reducing reflection losses to 3.20 mA cm^{-2}. Jošt et al.[187] proposed an alternative approach by adding a 100 μm-thick LM foil to a $Cs_{0.05}(MA_{0.17}FA_{0.83})Pb_{1.1}(I_{0.83}Br_{0.17})_3$-Si tandem cell, reducing reflection losses and front TCO parasitic absorption up to 1.18 mA cm^{-2} (Figure 12c). This strategy improved efficiency from 23.4% to 25.5%, with a J_{SC} of 18.5 mA cm^{-2}. However, reflection losses of 2.48 mA cm^{-2} remained, underscoring the need for more effective LT strategies to improve performance and cost-effectiveness of 2 T-PSTSCs. Proper LT strategies are crucial to maximize the power output of the perovskite top cell, as concluded from the previous subsection.[39,141,188–192] More recently, further efforts have focused in mastering the development of fully textured monolithic 2T-PSTSCs. That is the case of the work of Sahli et al.[41] that developed fully textured monolithic PSTSCs with a certified PCE of 25.2% and 19.5 mA cm^{-2} of J_{SC}. By transitioning from a polished front-side to a double-textured c-Si layer, the authors reduced the overall reflectance and minimized current loss to 1.64 mA cm^{-2}. For the first time, the conformability of the layers deposited over the front silicon micropyramids was ensured through a combination of gentle physical coevaporation of PbI_2 and CsBr and standard spin-coating methods of the remaining precursors onto the coevaporated layer. The perovskite absorber is formed via annealing of the deposited layers in a controlled humidity environment. This approach was then followed by Aydin et al.[193] that proposed a fully textured 2T-PSTSCs with 19.8 mA cm^{-2} of J_{SC} and 25.1% of PCE. The devices showed <2% of average reflection in the 290–1100 nm range, enabling such a high J_{SC}. While thermal evaporation shows promise, the complexity of the fabrication method that requires multiple precursor sources and significant capital costs remains challenging for marketability. Moreover, solution-processed perovskite cells still outperform vacuum-deposited counterparts.[194] To circumvent this issue, Ju et al.[195] and Nguyen et al.[196] focused on reducing the front-Si texture size to 2 μm and on increasing the perovskite charge-carrier diffusion length. This approach, combined with high-throughput solution-processing methods, such as spray coating,[197,198] slot die coating,[199,200] and blade coating,[201,202] provides an efficient path forward. The work of Chen et al.[203] demonstrated the feasibility of these methods, achieving a PCE of 26.2% and a J_{SC} of 19.2 mA cm^{-2} by blade coating a $Cs_{0.1}MA_{0.9}Pb(I_{0.9}Br_{0.1})_3$ perovskite on submicrometer double-sided textured silicon wafers in ambient atmosphere (speed of 1.5 m min^{-1}). Adding front textured-PDMS mitigated front reflection losses to 2.3 mA cm^{-2}, illustrating a successful approach for highly efficient 2 T-PSTSCs. The proposed devices showed 19.2 mA cm^{-2} of J_{SC} and 26.2% of PCE.

The benefits derived from the adoption of advanced optical schemes go beyond the above-described LT enhancements. Tockhorn et al.[204] fabricated gentle sinusoidal nanotextures on the c-Si top surface of monolithic PSTSCs using NSL, a high-resolution technique involving self-assembled colloidal masks to fabricate periodic nanostructures (Figure 12d). Integrating a SiO_2 rear dielectric buffer layer further reduced rear parasitic absorption losses. In addition to increasing light absorption, these nanostructures were found to enhance perovskite crystal growth, slightly improving PCE by 1% (from 29.5 to 29.8%, see Figure 12e). Analyzing the difference in the azimuthal intensity profiles of the (100) reflection of perovskite layer onto planar and nanotextured substrates shown in Figure 12f, at scattering angles of 70°–90°, it is suspected that the nanotextures induce a different (yet beneficial) orientation of the perovskite crystallites, potentially facilitating the carriers diffusion. This is still a controversial topic. Some reports defend a correlation improvement of the optoelectronic properties of the perovskite layer due to improved perovskite crystallites orientation,[205–208] while other reports claim there is no clear correlation.[152] More recently, Ying et al.[209] proposed a more substantiated correlation between nanostructuring the substrate to align perovskite crystallite orientation and the improvement of carriers diffusion. To support their claims, they fabricated a coupled front-sided-nanostructured black silicon (b-Si) with a tunnel oxide-passivated contact (TOPCon), as represented in Figure 12g. On the nanotextured surface, single-perovskite grains formed consistently along the thickness of the film (Figure 12h). Contrastingly, similar thickness film on planar substrates produced perovskite grains with reduced average size (Figure 12i). Further characterization revealed enhanced quality in the perovskite absorber fabricated on the nanotextured surface. The nanostructured surface exhibited a lower contact angle for the perovskite precursor compared to the planar counterpart. This optimal low-polar and high-dispersion nanotextured surface resulted in excellent film coverage and improved quality of the spin-cast wide-bandgap perovskite film. Furthermore, the small lateral size of the nanotextures facilitated the predominantly vertical growth of the perovskite grains. Such nanostructures significantly suppress the reflectance and reduce the current loss to 2.6 mA cm^{-2}, as shown in Figure 12j. Ultimately, the tandem cells showed 19.3 mA cm^{-2} of J_{SC} and 28.5% of PCE, values comparable to or even superior to fully textured architectures. It is worth mentioning the following work of Li et al.[210] and the work of De Bastiani et al.[211] that report LT schemes similar to those proposed by Ying et al.[209] respectively showing 18.8 mA cm^{-2} of J_{SC} and 22.1% of PCE, and 19.7 mA cm^{-2} of J_{SC} and 27.4% of PCE.

4.1. Optical-Tailored Interlayers of PSTSCs

Maximizing the PCE of tandem solar cells relies heavily on optimizing the interlayer between subcells. This optimization involves integrating effective LT schemes, especially tailored to capture NIR photons within the bottom absorber.

In the context of 2 T-PSTSCs, a notable instance is the work of Mazarella et al.[212] that introduced an alternative route to leverage the benefits of wet chemical perovskite processing while mitigating the optical constraints linked to front side planar Si wafers. This method integrated a nanocrystalline silicon oxide (nc-SiO_x:H) interlayer into a 2 T-PSTSC, as represented in **Figure 13**a, and started by studying its refractive index up to $n = 3$ (Figure 13b). The increase of the refractive index reduced reflection losses, resulting in a significant enhancement of the output current of the silicon bottom cell and consequently the tandem. By increasing the thickness of the interlayer to induce optimal wave interference effects up to ≈110 nm, and further tuning its refractive index to 2.6, the tandem achieved a 12% boost in J_{SC}, equivalent to an absolute gain of 1.4 mA cm^{-2}. The best-performing tandem device delivered a certified PCE of 25.2%, with a total current density of 38.7 mA cm^{-2}. Here, it is worth mentioning once more the work of Sahli et al.[41] which reports a fully textured PSTSC that either couples a nanocrystalline hydrogenated silicon (nc-Si:H) or an ITO interlayer. The tandems that featured the nc-Si:H interlayer showed a V_{OC} of 1.78 mV, whether those that featured a conventional ITO interlayer yielded a maximum V_{OC} of 0.70 mV (Figure 13c). The higher V_{OC} was given by the lower difference in surface tension between the nc-Si:H and the overlaying layer (spiro-TTB, HTL) when compared to that for ITO, which enabled a subsequent conformal deposition of the HTL. More recently, Han et al.[213]

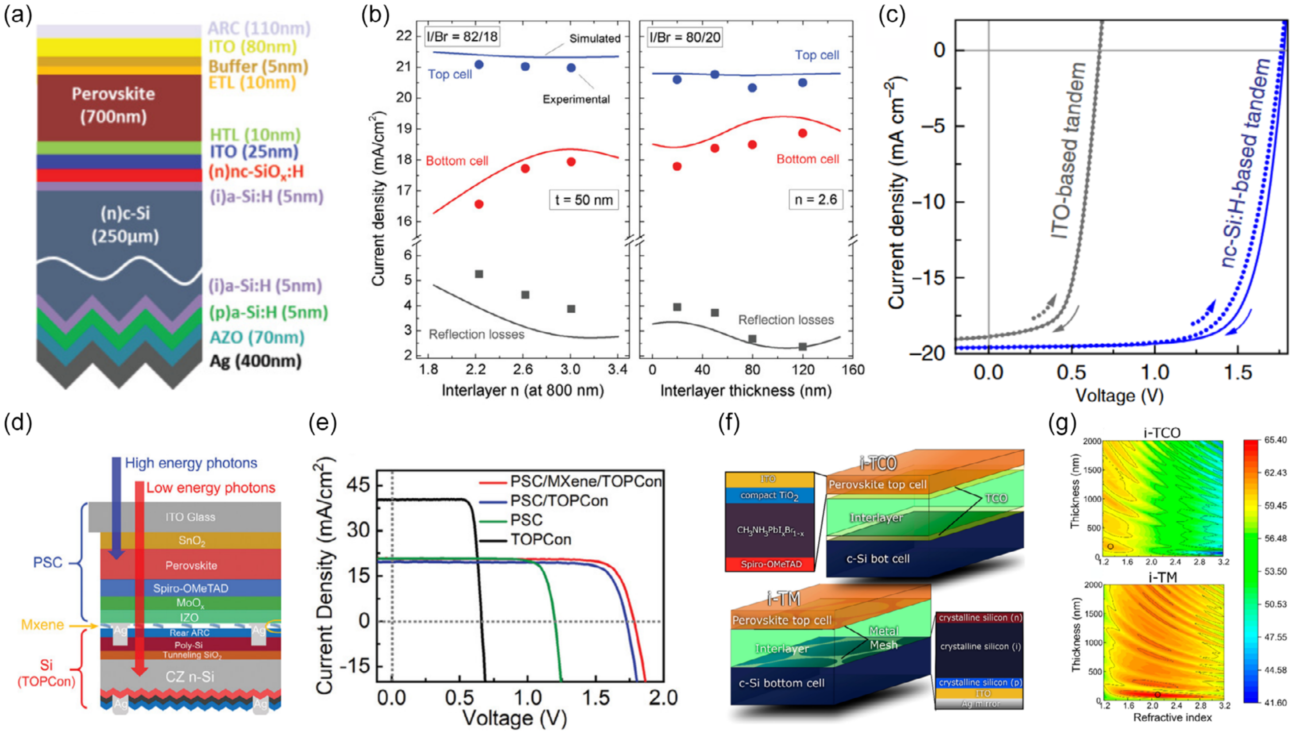

Figure 13. Optical tailored interlayers of state-of-the-art PSTSCs. a) This panel displays a cross section of the simulated monolithic planar perovskite/SHJ tandem cell. b) In the subpanel on the left, experimental data (circles) and simulated results (full lines) for the J_{SC} of the top and bottom subcells, along with reflection losses out of the cell, are depicted as a function of the interlayer refractive index (*n*) with a thickness of 50 nm. The perovskite absorber layer utilized in these experiments was $Cs_{0.05}(FA_{0.83}MA_{0.17})_{0.95}Pb(I_{0.82}Br_{0.18})_3$. In the subpanel on the right, experimental data (symbols) and simulated results (line) for the J_{SC} of the top and bottom cells, as well as reflection losses of the cell, are presented as a function of the interlayer thickness with an *n* value of 2.6 at 800 nm. The perovskite absorber layer used in these experiments was $Cs_{0.05}(FA_{0.83}MA_{0.17})_{0.95}Pb(I_{0.8}Br_{0.2})_3$. Reprinted with permission.[214] Copyright 2019, John Wiley and Sons. c) *J–V* characteristics of fully textured perovskite/SHJ tandem devices that couple either an ITO or nc-Si:H recombination junction. Reprinted with permission.[41] Copyright 2018, Spinger Nature. d) Schematic configuration of MXene-contact two-terminal, mechanically stacked perovskite/textured silicon tandem solar cell. e) The *J–V* curves are depicted for the TOPCon solar cell (black), the semitransparent PSC (green), and the perovskite/silicon tandem solar cells with (red) and without a MXene contact (blue). Reprinted with permission.[215] Copyright 2024, John Wiley and Sons. f) Sketches of the two 4T tandems architectures considered cases in the study. g) Contour plots illustrate the J_{PH} as a function of the interlayer's refractive index and thickness for two cases: the intermediate TCO contacts (i-TCO, top) and the intermediate transparent metal contacts (i-TM, bottom). Reprinted with permission.[219] Copyright 2019, American Chemical Society.

mechanically interconnected semitransparent PSCs and TOPCon solar cells with MXene interlayer to design 2T-PSTSCs (**Figure 14**d). The MXene layer enhanced interfacial carrier transportation without minimally influencing light transmission, allowing the tandem to achieve a stable PCE of 29.7% and a J_{SC} of 20.7 mA cm^{-2}, which correspond to relative increases of ≈11% and ≈5% in regard to tandems without MXene interlayer (Figure 13e). The tandem also retained ≈92% of its initial PCE after 1000 h in ambient air conditions.

Contrastingly, the design of 3- or 4-terminal (3 and 4T) tandem solar cells demands a more nuanced approach, involving optimal contact positioning and precise voltage matching between subcells.[39,214,215] Recent optoelectronic models highlight a 30% reduction in parasitic absorption of low-energy photons by replacing the intermediate TCOs (iTCOs) with intermediate transparent microstructured metallic contacts (iTMMCs) in 4T-PSTSCs.[141,184,216,217] In the study by Chapa et al.[216] a comprehensive optoelectronic model clarified the optical mechanisms of this LT approach (Figure 13f). Theoretical emulation of a 17 μm-thick c-Si absorber, achieved by randomly texturizing the front and rear surfaces of a 1.5 μm c-thin Si layer, substantially increased light absorption, resulting in fivefold boost (15.3 mA cm^{-2} for the silicon sub-cell) compared to a 1.5 μm planar c-Si absorber. However, the overall PCE of the simulated tandems coupled with the iTMMCs (≈21.5%) still lags behind the state of the art (30.1%), probably due to unaddressed front UV-reflection losses.[41,204,218] The optimization algorithm favored a higher refractive index ($n_{iTM} \approx 2.1$, Figure 13g), aligning with the trend observed by Mazarella et al.[212] for better light in coupling toward the bottom c-Si subcell. Additionally, optimization of a planar intermediate transparent contact (TCO/interlayer/TCO) was also performed. This optimization revealed an "optical well" that enhanced the LT within the bottom absorber. The metal thin layer with a low refractive index in between TCO layers (e.g., silver, copper) confined longer-wavelength photons.[216] Despite theseadvancements, further theoretical studies and experimental validation are needed to compete with state-of-the-art efficiencies (33.9%)[219] of 2T solar cells that simply integrate a planar iTCO and capitalize on achievable optical benefits from optimized interlayers.[191,218,220]

5. Radiative Cooling for Thermal Management of PV Systems

Considering the pronounced thermal oscillations encountered in space environments (−200 to 130 °C),[51] our discussion now extends to the contemporary advancements in radiative cooling systems, indispensable for the normal operation of space PV systems. We focus on evaluating their radiative cooling efficacy and prospective optical and electrical advantages, albeit primarily examined within terrestrial contexts.

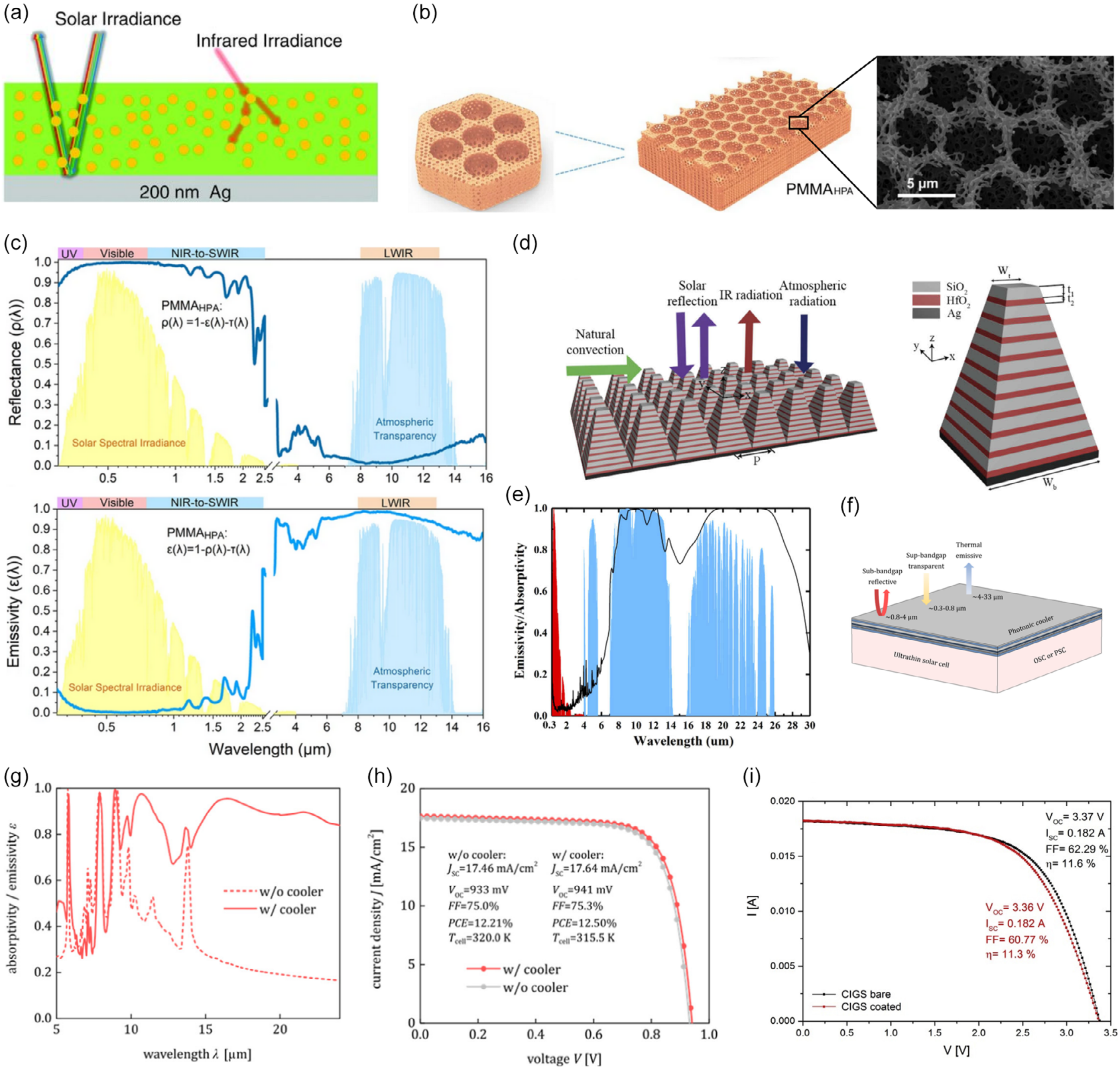

Figure 14. Photonic cooling effects of front add-on coatings for advanced thermal management. a) Schematic of the polymer-based hybrid metamaterial embedded with randomly distributed SiO_2 microspheres. Reprinted with permission.[228] Copyright 2017, The American Association for the Advancement of Science. b) $PMMA_{HPA}$ with a porous array and SEM images depict an ordered symmetrical micropore array comprising hierarchical randomized nanopores. c) The spectral reflectance (top) and emissivity (bottom) of the $PMMA_{HPA}$ film with an effective thickness of ≈160 μm, alongside the normalized ASTM G173 solar spectrum and the long-wave infrared radiation atmospheric transparency window. d) Schematic of the 3D pyramid multilayer metamaterial passive radiative model composed of all-dielectric pyramidal multilayer metamaterial structures of HfO_2 and SiO_2. e) Simulated emissivity/absorptivity of the PMM radiative cooler. Reprinted with permission.[229] Copyright 2019, Optica Publishing Group. f) Schematic illustrating the proposed organic–inorganic hybrid radiative cooling coating/scheme applied in the considered USCs. g) Absorptivity/emissivity, ε, spectra at $\theta = 0$, $\varphi = 0$ of the PSC without (dashed) and with a photonic cooler (full line). h) J–V curve of the PSC, and the corresponding photovoltaic characteristics (J_{SC}, V_{OC}, FF, and PCE) in the inset. i) I–V curve of a CIGS solar module before and after coating. Reprinted with permission.[231] Copyright 2020, Elsevier.

5.1. Photonic Frontal Add-Ons for Thin PV Cooling

Radiative heat transfer is a critical consideration in space environments, where heat conduction and convection are absent. In such conditions, radiative cooling becomes the primary mechanism of heat dissipation, emphasizing the importance of efficient thermal management of solar cells for space applications to ensure their normal operation.[56] Efficient terrestrial passive radiative cooling systems often employ thick window layers (>5 μm, to match mid-IR wavelengths) with randomly distributed micrometric elements.[221–225] Examples include 50 μm-thick metamaterials composed of 1 μm-thick SiO_2 microspheres randomly embedded in a polymethyl-pentene (TPX) matrix, combined with a Ag silver rear mirror (Figure 14a).[226] This configuration exhibits an average emissivity of 93% in the mid-IR-to-IR range and 96% reflectivity in the visible range, at ambient temperature. The combined structure delivers up to 93 W m^{-2} of cooling power.

To the best of our knowledge, the highest reported radiative cooling power has been achieved through 3D ordered structures, such as metal–dielectric–metal resonators, periodic arrays, gratings, pyramidal nanostructures, conical pillar arrays, multilayer, and dielectric resonators.[221–225] Among these, periodic structures offer precise control over the absorption and reflection of incident light, in contrast to random arrays. For instance, Wang et al.[225] demonstrated exceptional solar reflectivity (95%) and broadband emittance (98%) of mid-IR photons under ambient temperature using a polymethyl methacrylate (PMMA) structured film with micro-/nanopore periodic arrays (Figure 14b). The micrometric pitch (≈5 μm), defined by the SiO_2 spheres diameter (Figure 14c), provides an effective escaping path for higher-energy photons via index matching. Notable radiative cooling power has also been reported in a modeling work of Kong et al.[227] Here, an all-dielectric pyramidal multilayer metamaterial with ≈20 μm of height and ≈10 μm of width structures of HfO_2 and SiO_2 (Figure 14d) provided up to 156 W m^{-2} (daytime) and 199 W m^{-2} (nighttime) of cooling power (Figure 14e).

The impact of photonic coolers extends beyond optimal thermal management, with recent studies suggesting substantial thermal resistance improvements with relatively thin radiative coolers (<5 μm of thickness).[52,59,61] However, uncertainties persist regarding their overall efficacy in material-based USCs and their performance under the extreme thermal fluctuations in space. The groundbreaking study by Perrakis et al.[57] contributes to understanding the impact of thinner radiative coolers on PV devices. In this research, a comprehensive electrothermal model was applied to a 1.4 μm-thin stack of planar organic/inorganic foils (PDMS/SiO_2/TiO_2/SiN/HfO_2) integrated onto ultrathin flexible PSCs. The incorporation of the proposed photonic cooler (Figure 14f) resulted in a synergistic effect between sub-bandgap wavelength filtering (≈0.8–4 μm), incoupling of sub-bandgap photons, and thermal emission of low-energy photons (≈4–33 μm), as illustrated in the absorptivity spectra of Figure 14g. The analysis of the J–V curve in Figure 14h revealed a slightly higher PCE (≈2.4%) of the device coated with the photonic cooler regarding conventional solar devices with standard planar polymeric substrates/encapsulants. This improvement in PCE resulted from the reduced operating temperature (up to ≈7.2 K), leading to increased V_{OC} by lowering the concentration, thermalized carriers, and the selective AR properties of the coating, which increased J_{SC}.[56,57,228]

The optoelectronic advantages conferred by photonic coolers to thin-film solar cells for extraterrestrial environments, while preserving the mechanical flexibility of these thin devices, can be found in the work of Banik et al.[229] This research investigated how thin (1.5–3.5 μm) silicon-oxycarbonitride planar coatings influence the electrical parameters of CIGS (Figure 14i) without compromising the mechanical flexibility of solar sails for space missions. It was found that a single-layer coating increased emissivity from 0.3 to 0.72 with minimal spectral losses. In parallel, simulation results demonstrated a significant 30% of reduction of the maximum temperature (from 100 to 30 °C) of the cells when subjected to the thermal shield of the 3.2 μm coating on cells in LEO. With an emissivity of 0.87 in the atmospheric window of 8–13 μm, the proposed coating emerges as a promising radiative cooler for extraterrestrial solar cells. Besides capitalizing on the low cost of the coating employed, empirical evidence demonstrated a marginal increase of 2.7% in the PCE of the CIGS solar cells, given the improved index matching (thus broadening the antireflection effect). These promising findings serve as key insights for future research, emphasizing the continued necessity of studying radiative coolers for upcoming space missions.

6. Photonics for Solar Spectrum Tailoring

The concept of "solar spectrum modification" encompasses three distinct strategies employed to alter the incident solar spectrum for enhanced utilization by PV devices:[230] DS,[43–50,231–260] UC,[247,257,261–276] and DC.[260,266,274,277] The following subsections provide benchmarks for DS and the application of UC and DC strategies.

6.1. Solar Spectrum Downshifting

The luminescent DS (LDS) effect is defined by the reemission of high-energy photons as lower-energy photons, as represented in **Figure 15**a. This phenomenon proves to be particularly advantageous for space PV, given the need to address the high portion of UV photons present in the AM0 irradiance spectrum. UV photons are usually lost through reflection, parasitic absorption, or thermalization of hot carriers within solar cells. Therefore, LDS offers a promising avenue to make use of this otherwise lost energy by converting UV photons to visible photons, aligning them closer to the quantum efficiency peak of PV devices. Common materials reported for LDS include organic dyes,[235,236,239,247,278] rare-earth materials,[44,45,48,237–239,245,247,257] and quantum dots (QDs).[47,49,231–234,240,243,248–256,260] While the poor stability of organic dyes and the low absorption coefficient of rare-earth elements pose challenges, QDs stand out due to their long-term stability and tunable absorption and emission spectrum.[279] Hence, QDs are a focal point in this review on the topic of mediating the LDS effect.

The analysis presented next provides a comprehensive outlook of LDS approaches adopted for multiple absorbers: CIGS, CdTe, GaAs, MAPI, a-Si:H, c-Si, and mc-Si. Figure 15b,c presents the

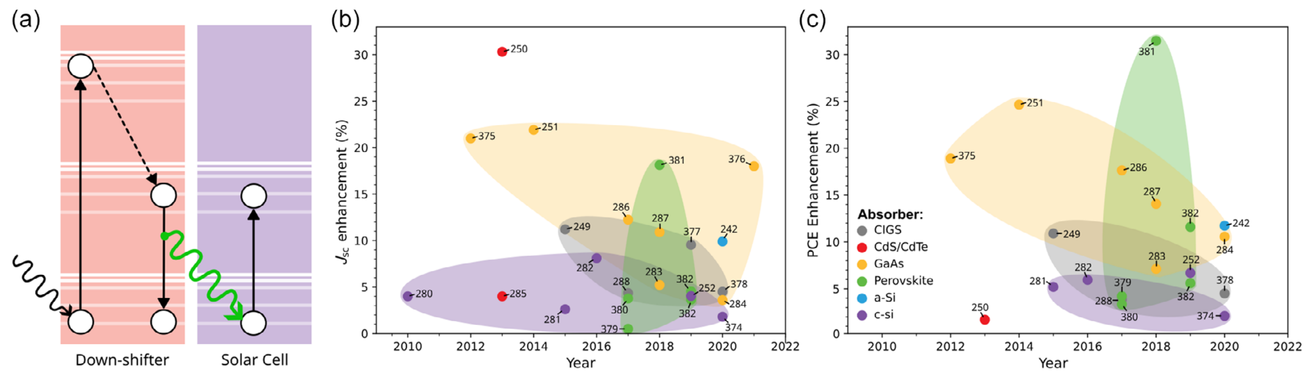

Figure 15. Overview of distinct solar cell technologies improved with spectral DS photonic schemes, reported by key contributions referenced in the plotted labels. a) Schematic energy diagrams illustrating the mechanism of LDS material assisting in PV generation. b) J_{SC} and c) PCE enhancement of solar cells coupled with LDS approaches as a function of respective publication year. All reported values are indicated in the Supporting Information.[249–252,254,280–288,374–382] The colored clusters englobe the different considered absorbers: CIGS (gray), CdS/CdTe (red), GaAs (yellow), perovskite (MAPI, green), a-Si:H (blue), c-Si (purple), and microcrystalline silicon (mc-Si, dark blue).

evolution of J_{SC} and PCE enhancements, respectively, for single-junction solar cells incorporating the LDS mechanism via QDs over the past decade. The primary focus has traditionally been on c-Si and GaAs technologies, driven by their commercial dominance. However, recent attention has shifted toward integrating LDS schemes with PSCs due to the ease of perovskite deposition methods, which are usually compatible with LDS fabrication techniques. **Table 4** provides a summary of solar cells coupling LDS schemes, presenting their J_{SC} and PCE enhancements under standard AM1.5 G irradiation.

The most common approach to couple QDs as LDS schemes on solar cells is to embed them in polymeric matrices. That is the case of the work Cheng et al.[280] that used the sol–gel method to embedded CdS-QDs in silica films on the front side of a c-Si solar cell, to improve its efficiency. With the integration of the LDS front layer, UV photons were downshifted to 500 nm visible photons. Ultimately, it improved the J_{SC} of the pristine cells by ≈4%. In another work, Xuan et al.[281] prepared CdSe/CdS/ZnS core/shell/shell QDs (**Figure 16**a) with a quantum yield of 25.2% and a concentration of 0.6 mg L^{-1} via microwave irradiation. These QDs were embedded into a SiO_2 matrix, which was then placed onto a standard c-Si cell. The incorporation of the QDs resulted in a large Stokes shift (from 390 nm to 575 nm), as depicted respectively in the absorption and photoluminescence spectra of Figure 16b,c. Consequently, the optically improved c-Si cells benefited from a 5.2% PCE enhancement. In another example, Ahmed et al.[282] employed plasmonic LDS (pLDS) composite layers comprising CdSe/ZnS core/shell QDs and Ag NPs embedded in a PMMA matrix onto c-Si cells. This combination resulted in relative enhancements of 7.8% and 6.0% respectively of J_{SC} and PCE against bare c-Si counterparts, due to DS effect combined with plasmonic resonances within the absorber. The additional absorption enhancement given by the Ag NPs is not only translated in the absorption–emission spectra, but also in the I–V curve (in terms of J_{SC} enhancement), as shown in Figure 16d. Meng et al.[252] later embedded $MAPbBr_3$ QDs in a PAN matrix, forming a composite LDS layer that was placed on the front side of c-Si cells. The LDS layer exhibited high transparency (>80%) at $\lambda > 500$ nm, remarkable quantum yield (>95%), and a refractive index of 1.56, minimizing UV reflectance. Absorption and emission peaks were respectively observed at 397 and 551 nm, increasing the J_{SC} by 4.0% (Figure 16e) and the PCE by 6.7%. Contrastingly, gallium-arsenide (GaAs) solar cells can also benefit from LDS. One example is the work of Cho et al.[283] that demonstrated GaAs solar cells coated with front $CsPbBr_3/SiO_2$ core/shell QDs embedded in a PDMS matrix. This front composite film improved the J_{SC} by 5.2% and the PCE by 7.1%. About one-third of the total J_{SC} increase was attributed to the DS effect and the rest due to broad antireflection effects. More recently, Huang et al.[284] followed a similar approach, achieving increases in J_{SC} and PCE of 3.6% and 10.6%, respectively, through a combination of broad antireflection effects and DS from 380 nm photons to 525 nm photons.

Cadmium-sulfide/cadmium-telluride (CdS/CdTe) solar cells can also be enhanced with QDs, as demonstrated in the pioneering work of Hodgson et al.[250] Here, the authors encapsulated CdS QDs in a PMMA matrix, which was then integrated over thin-film CdS/CdTe solar cells. The J_{SC} increased by 30.3%, for high concentration of QDs (≈192 μg mm^{-3}), compared to uncoated devices, due to DS and pronounced light-scattering effects toward the absorber. Later, Hodgson et al.[285] embedded commercial QDs in a PMMA matrix as front LDS layers for CdS/CdTe solar cells, resulting in a 2.8% increase in J_{SC} increase attributed to LDS and an additional 1.2% increase from strong light scattering.

QDs may also be directly deposited on top of solar cells. Han et al.[251] used a traditional GaAs-based solar cell coated with 530 nm CdSe/ZnS core–shell QDs (Figure 16f) to achieve a 24.7% efficiency gain. Notably, only 6.6% of the photogenerated current improvement was attributed to the LDS effect (Figure 16g), emphasizing the importance of the antireflection properties provided by the front LDS layers (n_{LDS}: ≈2.4) in establishing a gradual index matching between the air (n: ≈1) and the absorber (n_{GaAs}: ≈3.8). Shu et al.[286] used a different approach, drop casting colloidal commercial QDs onto trenched GaAs solar cells to bring the LDS effect closer to the cells' p–n junction. This method resulted in a 12.2% increase in J_{SC} and a 17.6% improvement in PCE, given the pronounced DS compared to

Table 4. Benchmark of the champion LDS integration results reported via the use of QD@matrix LSD materials coated on different PV devices with distinct absorber materials. The J_{SC} (ΔJ_{SC}) and PCE (ΔPCE) relative enhancements, determined with respect to the counterparts without integrated QDs, are presented in the last columns. The power-to-weight ratio accounts for the weight of the solar cells made of wafer-based c-Si absorbers. For the thin-film cell (made of a-si, CdS/CdTe, GaAs, CIGS, MAPI absorbers), the weight of a standard 125 µm thick polyimide substrate is considered to account for the same mechanical support needed to handle such nonwafer-based devices. Detailed calculations and data are available in the Supporting Information.

#	Ref/ Year	Absorber	Position	Method	QD material-matrix	Mechanism	Size [nm]	Absorption peaks	Emission peaks	ΔJ_{SC} [%]	ΔPCE [%]	Power-to-weight ratio [W g^{-1}]
1	[280]/ 2010	c-Si	Embedded	Sol–gel process	$CdS–SiO_2$	DS	–	280 nm	500 nm	4.0		–
2	[281]/ 2015	c-Si	Embedded	Microwave irradiation	$CdSe/CdS/ZnS-SiO_2$	DS	3.9	445 nm	600 nm	2.6	5.2	–
3	[282]/ 2016	c-Si	Embedded	Commercial + Dip coating	CdSe/ZnS + Ag NPs*-PMMA	DS	45	UV region	500 nm	8.1	6.0	–
4	[252]/ 2019	c-Si	Embedded	Dissolution + Spin coating	$CH_3NH_3PbBr_3$-PAN	DS + antireflection	–	397 nm	551 nm	4.0	6.7	0.34
5	[374]/ 2020	c-Si	Embedded	Hot-injection + Drop coating	$CuInS_2/ZnS/ZnS$-EVA	DS + scattering	2.1	370 nm	570 nm	1.8 (I_{SC})	2.1	0.23
6	[254]/ 2020	a-Si	Embedded	Spin coating	$Cd_xZn_{1-x}Se_yS_{1-y}/ZnS$-PDMS	DS + antireflection	10	365 nm	531 nm	9.7 (I_{SC})	1.1	0.09
7	[375]/ 2012	GaAs	On top	Spin coating	CdS	DS + antireflection	5	UV region	460 nm	21.0	18.9	0.12
8	[251]/ 2014	GaAs	On top	Commercial + Drop coating	CdSe/ZnS	DS + antireflection	6	UV region	530 nm	21.9	24.7	0.91
9	[286]/ 2017	GaAs	On top	Commercial + Drop coating	CdS/ZnS	DS	–	UV region	–	12.2	17.6	–
10	[287]/ 2018	GaAs	On top	Commercial + Drop coating	$CsPbBr_3$	DS + antireflection	–	UV region	–	10.9	14.0	–
11	[283]/ 2018	GaAs	Embedded	Drop coating	$CsPbBr_3/SiO_2$-PDMS	DS + antireflection	–	UV region	–	5.2	7.1	0.94
12	[284]/ 2020	GaAs	Embedded	Drop coating	$CsPbBr_3/SiO_2$-PDMS	DS + antireflection	–	380 nm	525 nm	3.6	10.6	0.93
13	[376]/ 2021	GaAs	On top	Spin coating	$FaPbBr_3$	DS + antireflection + light scattering + passivation	7	UV region	530 nm	18.0	–	–
14	[250]/ 2013	CdS/CdTe	Embedded	Drop coating	CdS–PMMA	DS + scattering	–	UV region	535 nm	30.3	1.7	–
15	[285]/ 2013	CdS/CdTe	Embedded	Drop coating	Commercial-PMMA	DS	–	460 nm	525 nm	4.0 (I_{SC})		–
16	[249]/ 2015	CIGS	On top (intermediate)	Pulsed spray deposition	CdSe/ZnS	DS	–	470 nm	526 nm	12.2	10.9	0.46
17	[288]/ 2017	CIGS	On top	Drop coating	$CdSe/CdZnS–MgF_2$	DS	4.6	300–630 nm	609 nm	4.4	3.9	0.79
18	[377]/ 2019	CIGS	Embedded	Immersion method	CdSe–PMMA	DS + antireflection	–	461 nm	555 nm	9.5		0.51
19	[378]/ 2020	CIGS	On top	Spin coating	$CsPbBr_3$	DS + antireflection	10	300–520 nm	532 nm	4.5	4.5	0.63
20	[379]/ 2017	$MAPbI_3$	On top	Hot injection + Spin coating	ZnSe	DS	3	389 nm	460 nm	0.5	4.2	1.00
21	[380]/ 2017	$MAPbI_3$	On top	Hot injection	$CsPbCl_3$:0.1Mn	DS	8	300–400 nm	590 nm	3.8	3.3	–
22	[381]/ 2018	$MAPbI_{3(1-x)}Cl_{3x}$	Embedded	Hydrothermal method	$CuInS_2$	DS	5	320 nm	775 nm	18.1	31.5	0.04
23	[382]/ 2019	$MAPbI_3$	Embedded	–	$CsPbBr_3$	DS + UV stability	8	365 nm	530 nm	3.6	11.6	0.06
24	[382]/ 2019	$MAPbI_3$	Embedded	–	$CsPbBr_3@SiO_2$	DS	8	365 nm	530 nm	4.5	5.6	–

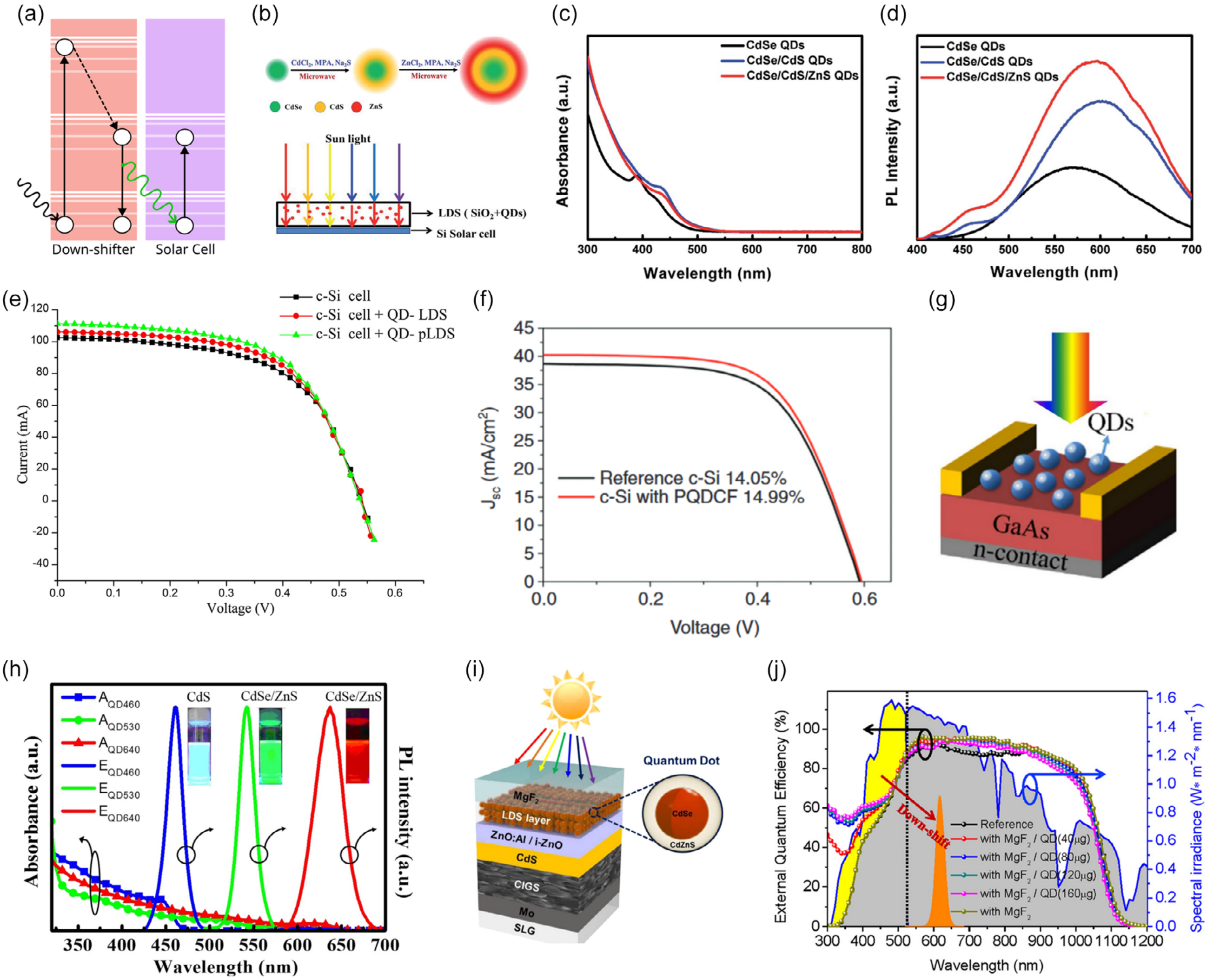

Figure 16. Analysis of PV performance of distinct solar cells employing coatings embedded with QDs for LDS effect. a) Schematic representation of the CdSe/CdS/ZnS core/shell/shell QDs (top) and CdSe/CdS/ZnS QDs/SiO_2 thin film as LDS layer for the considered Si solar cell (bottom). b) UV–vis absorption spectra and c) photoluminescence spectra of CdSe, CdSe/CdS, and CdSe/CdS/ZnS QDs. Adapted with permission.[283] Copyright 2015, The Royal Society of Chemistry. d) *I–V* curves of c-Si solar cell with no LDS layer (black), with QD-LDS layer (red) and with pLDS composite layer (green). Reprinted with permission.[284] Copyright 2016, Elsevier. e) *J–V* curves of c-Si and mc-Si SCs coated with and without perovskite QDs composite film. Reprinted from,[254] Copyright 2020, with permission from De Gruyter. f) QD-sensitized single-junction GaAs solar cell. g) UV–vis absorbance and photoluminescence (blue, green and red) spectra of the fabricated QDs. Reprinted with permission.[253] Copyright 2014, Springer Nature. h) Schematic design depicting a CIGS solar cell integrating the deposition of CdSe/CdZnS QDs onto the window layer. i) EQE of the CIGS cell with varying quantities of QDs, depicted alongside the AM1.5 G spectral irradiance spectrum. The enhancement in EQE attributed to the downshifting mechanism at short wavelengths is highlighted in yellow. Reprinted with permission.[375] Copyright 2017, American Chemical Society.

uncoated devices. However, the trench structure caused significant sidewall current leakage, leading to devices with a J_{SC} of merely 5.8 mA cm^{-2}. That is also the case of the design proposed by Chen et al.[287] which deposited commercial perovskite QDs on ITO whiskers to increase the quantity of adsorbed and nonaggregated QDs. The ultimate PCE of the ITO-structured devices (maximum PCE of 4.2%) was lower than that of the uncoated reference cell (5.9%). In turn, the PCE of the reference cells without ITO-structured electrodes (QDs directly dispensed on top surface) achieved a PCE of 6.7%, which is higher than both ITO-structured and pristine cells. Nonetheless, the ITO-structured devices showed up to 10.9% of increase in J_{SC} and a 14.0% improvement in PCE compared to uncoated devices, demonstrating the efficacy of LDS combined with broad antireflection effects. Later, Jeong et al.[288] enhanced CIGS solar cells by depositing MgF_2 ARC onto an LDS layer of CdSe/CdZnS core/shell QDs (Figure 16h). This combination enabled the LDS of UV photons to 630 nm photons and provided antireflection benefits from the ARC/QDs stack (Figure 16i), leading to respective increases in J_{SC} and PCE of 4.4% and 3.9% compared to uncoated devices.

Micro- or nanoscale patterns can further enhance the optical benefits of front LDS layers by improving chemical stability, adhesive properties, and mechanical resistance of PV devices.[244,289] Simulation plays a key role in optimizing complex patterning geometries and estimating optoelectronic gains of PV devices, as demonstrated in the work of Alexandre et al.[259] In this study, the author emulated a solar spectrum resulting from an LDS layer, serving as an encapsulant for optically improved PSCs (**Figure 17**a,b). Despite an inferior UV photocarrier generation in both the ETL (TiO_2) and perovskite layer compared to the planar counterpart (with optimized front ARC), a marginal increase of ≈2% in the photocurrent was attained with the thinnest perovskite absorber layer (250 nm). This is of particular interest for PSCs, which are highly susceptible to UV-induced photodegradation.[289–291] Ghymn et al.[240] fabricated GaAs solar cells with a front moth-eye antireflection LDS layer comprising CdZnS/ZnS core/shell-type QDs embedded in a polydimethylsiloxane (PDMS) matrix (Figure 17e,f). By capitalizing on the low optical absorption of GaAs at low wavelengths, this structure provided both antireflection effects through index matching (Figure 17g) and DS of UV photons, resulting in ≈3.2% of efficiency improvement (up to 28.7% of PCE) due to enhanced charge carrier generation and collection, as seen by the J_{SC} improvement depicted in Figure 17h.[251]

6.2. Up and Down Photon Conversion

A distinct approach to spectrum conversion involves the processes of UC and DC, each based on opposite physical phenomena (see **Figure 18**a,b for comparison). UC absorbs two below-bandgap-energy photons ($E_{ph} < E_g$, typically NIR photons) to generate a higher-energy photon ($E_{ph} > E_g$, typically UV–vis photons), thus facilitating photovoltaic conversion (Figure 18a). On the other hand, DC converts high-energy photons into two lower-energy photons (Figure 18b).[292] Both strategies expand the usability of the solar spectrum, applicable to terrestrial and extraterrestrial scenarios. UC is relevant for the abundant infrared range (>700 nm), which constitutes up to 52% of solar radiation reaching Earth's surface. Similarly, DC benefits from the higher availability of UV photons in the AM0 irradiance spectrum compared to AM1.5 G. Unlike DS, where the quantum efficiency may be limited, DC exhibits a quantum efficiency ≥1, as it generates two above-bandgap lower-energy photons from a

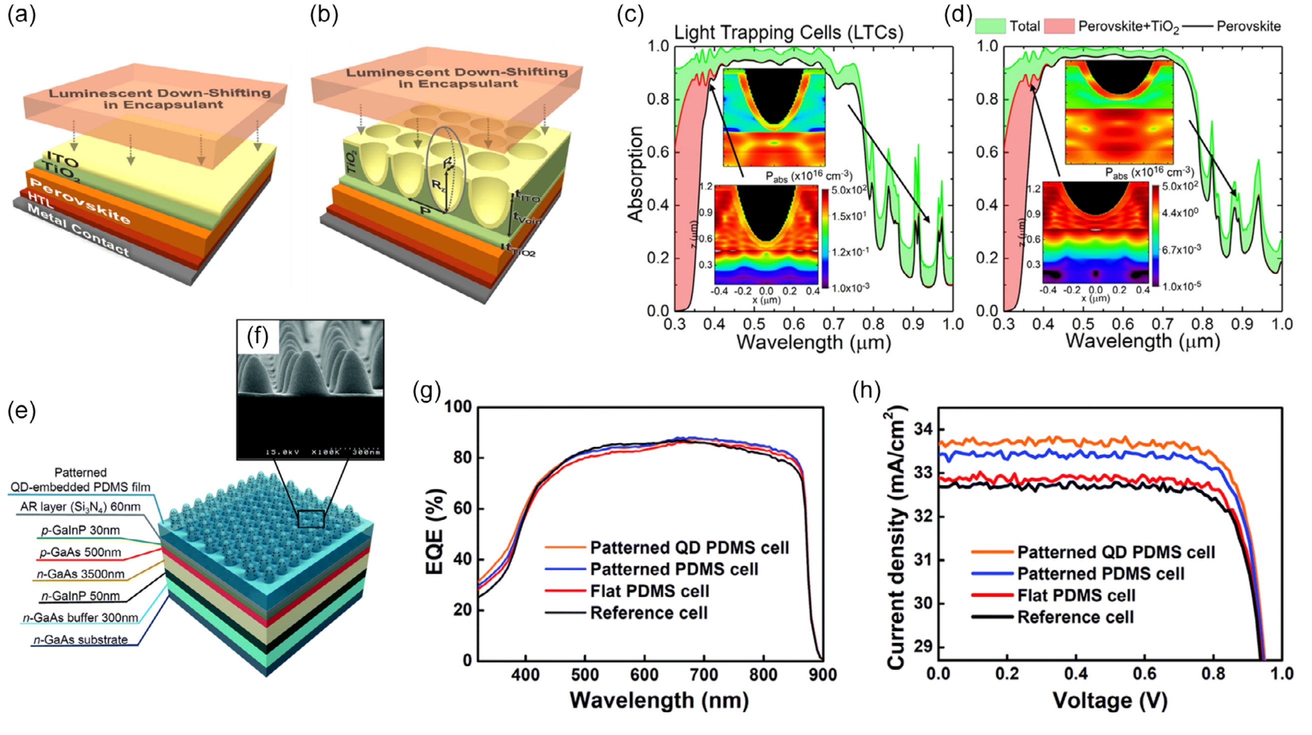

Figure 17. Dual LT and spectral-tailoring optical improvements with front photonic plus LDS encapsulants. a) Schematic depicting the planar cell structure used as a reference, comprising the following layers: metal contact (Ag), hole transport layer (Spiro-OMeTAD), absorber (MAPI perovskite), electron transport layer (TiO_2), and transparent conductive oxide (ITO). b) ETL-structured PSC, whose ETL is conformally covered with the ITO layer. Absorption profiles determined for the photonic-enhanced cells with perovskite thickness of c) 250 and d) 500 nm, respectively. The perovskite layer absorption profile corresponds to the black line, the perovskite + TiO_2 absorption in red, and the total absorption of the cell in green. The inset plots illustrate the absorbed power density (P_{abs}) across the cross section of the cell, calculated at specific wavelengths indicated by the arrows: 350 nm (left) and 900 nm (right). Reprinted with permission.[261] Copyright 2019, American Chemical Society. e) Schematic illustrating the structure of GaAs cells covered by patterned QD-embedded PDMS films. f) SEM image of patterned QD-embedded PDMS films. g) EQE spectra and h) *J–V* curve of GaAs cells covered with flat (red) and patterned (dark blue) PDMS and patterned QD-embedded PDMS films (orange), compared to the *J–V* curve of the planar counterpart (no PDMS coating). Reprinted with permission.[242] Copyright 2015, The Royal Society of Chemistry.

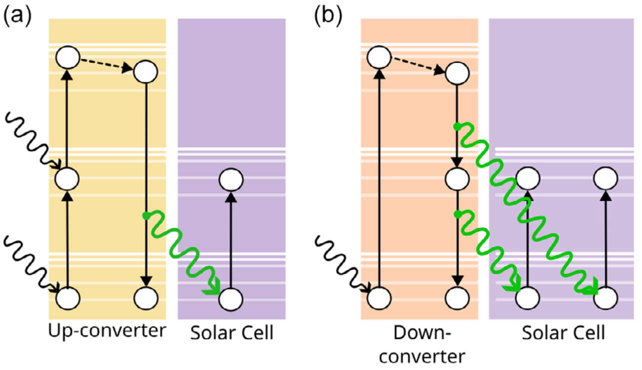

Figure 18. Illustration of UC and DC phenomena assisting photogeneration in PV. Energy diagram schematics of the mechanisms of a) UC and b) DC materials.

higher-energy photon. Such characteristic underscores its potential as an efficiency enhancer.[12] Our review concentrates on the UC and DC (or the combination of both) literature published in the past four years, building upon the insights provided in the review of Chen et al.[12]

A common strategy to leverage UC or DC involves designing a front up- or down-converter that can be integrated into the full device architecture or placed in direct contact with the solar device. Trivalent lanthanide-based rare-earth elements are regarded as the optimal strategy for both UC and DC given their unique optical properties, such as high quantum yields, long-lived excited states, large Stokes shift, and sharp emission lines.[12] An example of solar devices supported by an external upconverter is the pioneering work of Chen et al.[267] where standard MAPI PSCs were combined with an independent front upconverter composed of a $LiYF_4:Yb^{3+}$, Er^{3+} single crystal. The addition of this independent front converter improved the PCE by 7.9% (**Figure 19**a) due to the strong UC of 980 and 1540 nm NIR photons to UV–vis photons (depicted in Figure 19b). Another example is the work of Sheng et al.[263] which introduced a rubrene (Rub) and dibenzotetraphenylperiflanthene (DBP) triplet–triplet annihilation (TTA) UC layer, fabricated via a one-step antisolvent process, into MAPI PSCs. The devices with the UC layer showed a maximum PCE of 20.2%, representing a 16.4% increase compared to the PSCs without the UC layer. The UC effect of converting NIR into visible photons increased the J_{SC} by 11.6%, as seen in the EQE spectrum of Figure 19c. Furthermore, the optimal Rub:DBP UC layer promoted the beneficial vertical growth of the MAPI nuclei, as evidenced by the 3.6% increase in V_{OC}. Lastly, the Rub:DBP unencapsulated devices maintained 80% of their pristine PCE after 14 days at 25 °C and 50–70% of humidity.

More recently, Ambapuram et al.[293] integrated a $NaYF_4:Yb^{3+}/Er^{3+}$ layer onto a $CdPbI_2Br$ PSC, which served as both an upconverter and light scatterer. This layer exhibits three distinct

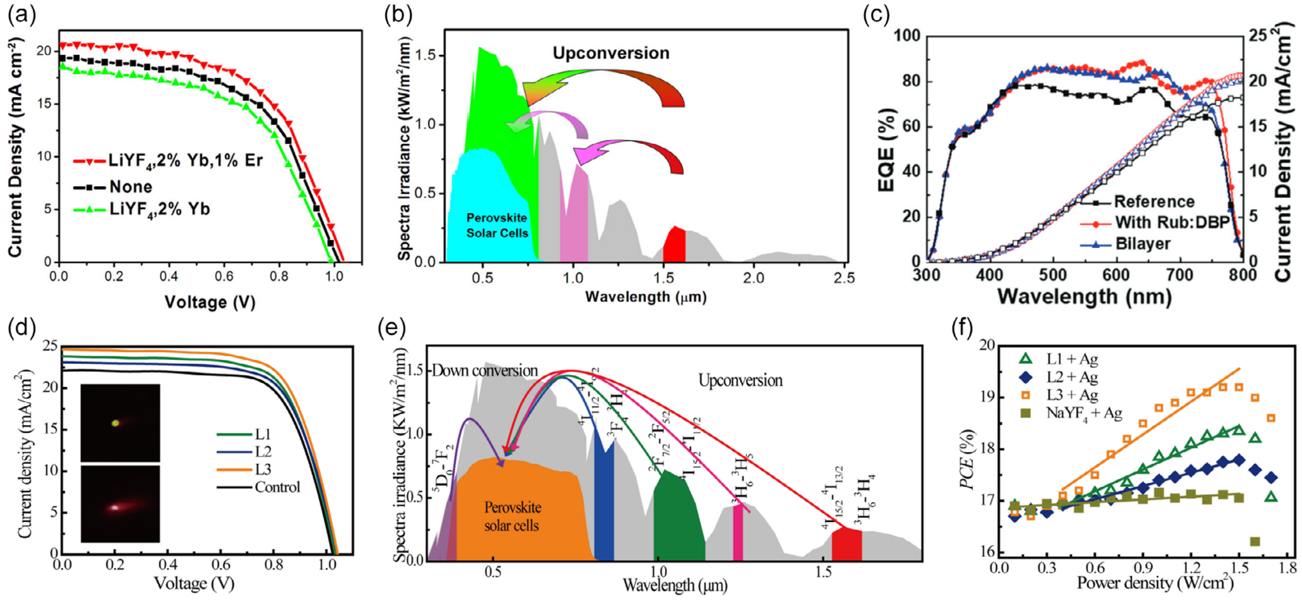

Figure 19. Optoelectronic performance of state-of-the-art PSCs coated with up- or downconverters. a) *J–V* curves of the PSCs: $LiYF_4$:2% Yb^{3+}, 1% Er^{3+} crystals (red), $LiYF_4$:2% Yb^{3+} crystals (green), and no crystal (black) measured under simulated solar illumination with 0.73 W cm^{-2} of intensity. b) Schematic of the AM 1.5G spectrum showing the fraction (highlighted in cyan) absorbed by the perovskite solar cell and the potential spectral regions aimed for UC (pink and red regions). Reprinted with permission.[269] Copyright 2016, American Chemical Society. c) EQE spectra and integrated J_{SC} of reference and PSCs coupled with rubrene (Rub) and dibenzotetraphenylperiflanthene (DBP) TTA UC layer fabricated via one-step (red) and spin-coating (bilayer, dark blue) procedures, respectively, compared to the pristine counterpart (black). Reprinted with permission.[265] Copyright 2021, The Royal Society of Chemistry. d) *J–V* curves of four optimized MAPI PSCs with (colored lines) and without (black control line) UCL layer under 1.5 W cm^{-2}. Emission images of L1 and L3 under xenon lamp are shown in the inset. L1 denotes $NaYF_4:Yb^{3+}$, Er^{3+}, L2 for $NaYF_4:Yb^{3+}$, Tm^{3+}, and L3 for $NaYF_4:Yb^{3+}$, $Er^{3+}/NaYF_4:Yb^{3+}$, Tm^{3+} composite layers. e) AM 1.5G spectrum highlighting the fraction absorbed by PSCs and the spectral regions that aimed for UC and DC phenomena. f) PCEs changing as a function of power density for L1-3 and reference ($NaYF_4$ crystal) samples with Ag rear mirror. Reprinted with permission.[268] Copyright 2018, Elsevier.

emission peaks in the regions of 400–420 nm, 510–560 nm, and 640–675 nm (corresponding to the blue, green, and red regions of the solar spectrum) due to the absorption of 980 nm NIR photons. Consequently, the J_{SC} and PCE increased by 24.9% and 40.0%, respectively, resulting in a final J_{SC} of 24.2 mA cm^{-2} and a PCE of 16.5%. Building on these developments, the work of Li et al.[266] advanced the field by enhancing both the optical and electrical performance of PSCs through the coupling of UC and DC layers. In their design, standard MAPI PSCs were coupled with a front DC (Eu(TTA)$_2$(Phen)MAA) and a rear UC (NaYF$_4$:Yb^{3+}, Er^{3+}/NaYF$_4$:Yb^{3+}, Tm^{3+}/Ag composite) layer. The resulting devices achieved a J_{SC} of 27.1 mA cm^{-2} and a PCE of 19.5% (Figure 19d,f, respectively). The enhancements were attributed to several factors: 1) the harvesting and conversion of UV and NIR photons to visible light via DC and UC (Figure 19e); 2) plasmonic scattering and rear reflection from the rear composite layer; 3) front antireflection properties; and 4) improved long-term UV stability. Moreover, the front encapsulation with the DC layer preserved ≈80% of the original PCE after 500 h of UV irradiation. Ultimately, the integration of the rear composite UC and the front DC layers contributed to efficiency increases of ≈19.3% and ≈1.6%, respectively.

Recently, rare-earth UC doping agents have also been integrated into the ETL, HTL, or the perovskite absorber of PSCs. For the first case, Wang et al.[265] codoped TiO$_2$ nanorod (NR) arrays with 13% Er^{3+} and 6% of Yb^{3+}, resulting in a larger conduction band difference between Er-Yb:TiO$_2$ NRs and the perovskite absorber. This configuration led to faster electron transfer and reduced recombination, significantly increasing the V_{OC} (**Figure 20**a) and enhancing the J_{SC} by 20.8% due to the

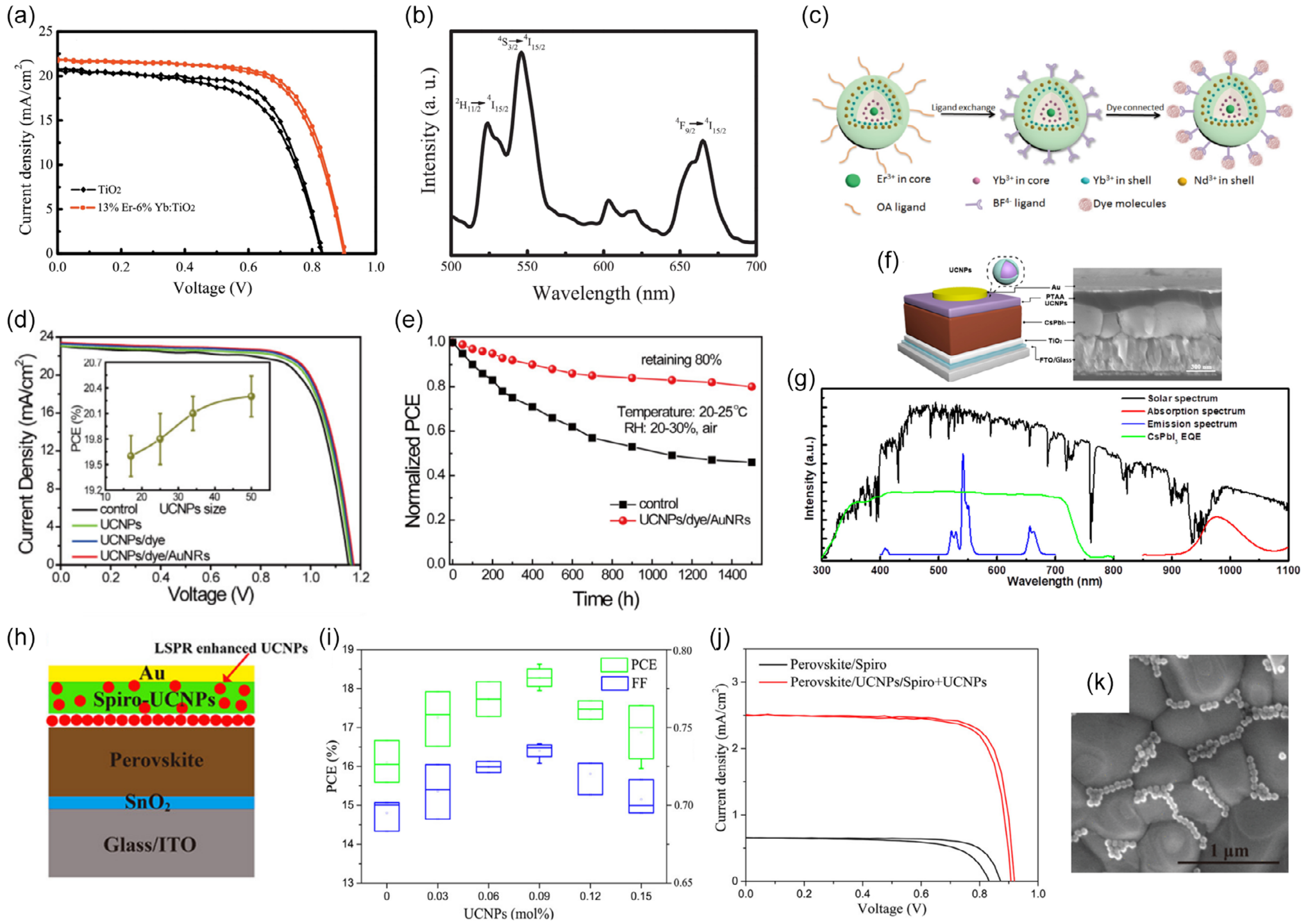

Figure 20. Optoelectronic performance and stability of state-of-the-art PSCs embedded with UC or DC agents. a) *I–V* curves of the optimal performance solar cells coupled with pristine TiO$_2$% and 13% Er-6%Yb:TiO$_2$ NRs. b) UC luminesce spectrum of 13% Er-6%Yb:TiO$_2$ NRs under an excitation source of 980 nm. Reprinted with permission.[267] Copyright 2017, Elsevier. c) Schematic diagram of the ligand exchange and IR-783 dye connected on UC NPs. d) *J–V* curves of PSCs comparing a control film with films incorporating UC NPs, UC NPs/IR-783 dye, and UC NPs/IR-783 dye/Au NRs composites under AM 1.5G irradiation. e) Stability of devices for a control film and a film incorporating a UC NPs/IR-783 dye/AuNRs composite film under air environment, relative humidity of 20–30%, and temperature of 20–25 °C. Reprinted with permission.[266] Copyright 2020, American Chemical Society. f) Schematic structure (left) and cross-sectional SEM image (right) of the proposed device. g) Solar (AM1.5G irradiance, in black), absorption (red), and emission (dark blue) spectra of UC NPs and EQE curve (green) of γ-CsPbI3 PSC. Reprinted with permission.[264] Copyright 2019, American Chemical Society. h) Schematic illustration of the PSCs endowed with local surface plasmon resonance (LSPR)-enhanced UC NPs. i) FF and PCE of the PSCs with different amounts of the LSPR-enhanced UC NPs in Spiro. j) *J–V* curves of the PSCs with and without UC NPs under a 980 nm laser of excitation source. k) Top-view SEM images of perovskite film with UC NPs in the grain boundaries. Reprinted with permission.[263] Copyright 2021, American Chemical Society.

NIR-to-vis UC at the Er-Yb:TiO_2 NRs (Figure 20b). Regarding device stability, a particularly interesting study by Bi et al.[264] involved coupling IR-783 dye-sensitized core/shell/shell $NaYF_4$:Yb^{3+}/Er^{3+}@$NaYF_4$:Yb^{3+}/Nd^{3+} UC NPs with the SnO_2 layer of PSCs (Figure 20c). The authors reported an increase of 5.7% in PCE (Figure 20d, inset), with the devices maintaining 80% of their original efficiency after 1500 h in ambient conditions. In contrast, the efficiency of the undoped devices dropped 50% from their initial value (Figure 20e).

While most efforts focus on ETL doping, UC agents integrated into the HTL can also positively impact the performance of PSCs, as demonstrated by Liang et al.[262] Optimized γ-$CsPbI_3$ PSCs with $NaLuF_4$:Yb,Er@$NaLuF_4$ UC NPs (Figure 20f) demonstrated up to ≈1.9% and ≈2.3% of respective enhancements in J_{SC} and PCE. The UC contribution to the overall device performance was minimal. The UC NPs primarily served as scattering centers, maximizing the PCE of the UC-boosted PSCs (Figure 20g) up to 15.9%. Later, Xu et al.[261] reported the simultaneous doping of the HTL and the perovskite absorber with $NaCsWO_3$@$NaYF_4$@$NaYF_4$:Yb,Er NPs (Figure 20h), resulting in ≈18.0% PCE improvement (Figure 20i) relative to the control device. As calculated from the J–V curve of Figure 20j, the PSC showed a maximum PCE of 18.9%. This improvement was attributed to the combination of UC of NIR-to-vis photons, evidenced by a ≈6% increase in J_{SC} (23.7 mA cm^{-2}), and filling of holes/gaps filling with UC NPs (Figure 20k), reflected in a ≈4% increase in V_{OC} (1.05 V).

7. Summary and Future Perspectives

This review comprehensively examines the latest advances and potential applications of photonic schemes in solar power generation for both terrestrial and extraterrestrial contexts across diverse solar cell technologies. Particular attention was given to dielectric-based wavelength-scale optical structures, as these are among the preferred means to boost the optoelectronic response of various photovoltaic technologies, as posed by recent research trends indicated in this review. Feasible and cost-effective photonic solutions were presented to address several critical technical challenges in solar cells, including: 1) incomplete absorption of the solar spectrum, particularly in thinner devices; 2) lack of flexibility of conventionally thick devices; 3) optoelectronic trade-off between random texturing and periodic structuring for LT; 4) low illumination adaptability particularly of multijunction tandems; 5) radiation and thermal endurance of space PVs; and 6) lack of spectrum tailoring strategies for various absorbers suboptimal bandgaps. Below, we outline the critical research principles aimed at addressing these challenges.

The discussed literature trends reveal a preference for standard random texturing processes (e.g., wet or dry etching) over periodic structuring methods (e.g., NSL) to enhance photon absorption in thick c-Si absorbers. This preference stems from the higher cost-effectiveness of the former and observed inferior optical performance in cells employing the latter approaches. Nevertheless, there is a need for further analytical or empirical modeling studies to anticipate the optimal absorption profile of PV absorbers integrated with front wavelength-sized structures, enabling a more rigorous comparison with the absorption profiles afforded by textured absorbers. Among texturing-based approaches, black silicon, which comprises c-Si nanotextures fabricated via dry etching methods, shows promise. This LT approach seeks to harness the advantages of photonic nanostructures, particularly their size, to enhance light–matter interactions, along with texturing-based processes that confer more pronounced antireflection properties due better index matching. However, this approach may face electrical restrictions, potentially exacerbated by the higher surface, that exceed the restrictions imposed by micrometric textures. Alternatively, wave optical coated structures emerge as a most promising LT approach to further enhance the PV efficiency of virtually all solar cell technologies, optimizing optical absorption while preserving electrical performance. Nonetheless, additional research endeavors are necessary for such optical schemes to rival industrially established methods. Among the photonic fabrication methods discussed, NSL has demonstrated reliability and precision in structuring photonic-effective materials like TiO_2 or other metal oxides, which are particularly favorable for LT.

Such discussion can be extended to thin-film PV technologies, where examining LM strategies underscores the crucial role of photonic schemes in optimizing physical thickness, to enable optically dense thin devices. Notably, thin Si solar cells are increasingly favored for adopting sophisticated LT approaches, a trend accentuated with decreasing absorber thickness, contrary to the thicker (>100 μm) wafer-based cells. Yet, despite the growing complexity of the adopted LT approaches, there remains a noticeable gap between effective LT observed in experimental studies and the theoretical-ideal predictions made by optical (Lambertian) models for thin/ultrathin devices. This gap is primarily attributed to front reflection losses and parasitic absorption in the selective contact layers. While texturing-based LT schemes, usually fabricated via dry etching techniques, have shown promising results in achieving J_{SC} values closest to those of Lambertian models, for thin Si cells, they also introduce heightened defect density, exacerbating charge recombination. Addressing the optoelectronic balance imposed by these texturing-based processes is crucial. Photonic-structured coatings made of high-refractive-index materials on the front surface may offer a unique pathway to circumvent such challenges. Yet, even more significant reflection losses are verified in the latest reports that follow such an approach. This is attributed to the relatively low aspect ratio and refractive index mismatch of the designed structures when compared to conventional textures. High-resolution techniques (e.g., NIL) are already capable of producing high-aspect-ratio features but onto "easily moldable" low-refractive-index materials, such as common photoresist (n: ≈1.5). An intuitive approach would be to couple these techniques with traditional deep RIE of the high-refractive-index materials. As for the refractive index mismatch, future developments could be carried out to mirror the best-performing ARC approaches of stacking multiple materials with graduated refractive index, for example, Si_3N_4, TiO_2, and GaP.

To mitigate parasitic losses in the contact layers, particularly in the rear mirror, integrating rear diffusive Bragg reflectors presents a promising approach. However, research findings on this topic vary; some studies demonstrate clear benefits while others do not. Rear diffusive Bragg reflectors hold potential for reducing rear parasitic absorption, but further investigation is necessary to substantiate their effective integration into test devices. It is worth mentioning that numerical methods should play a major role in future research, as they open novel investigative pathways (e.g., simple and effective LT schemes) while minimizing material and processing costs. These methods can help establish upper boundaries for achievable J_{SC} values and elucidate the optical phenomena in play.

This review also addresses perovskite PV, which holds significant potential and has recently garnered interest for space applications. The distinctive absorption profile of perovskite absorbers has led much of the research to focus on mitigating inherent electrical losses. Still, LT schemes, such as the wavelength-sized structures discussed in this review, can significantly impact the electrical domain of photonic-enhanced PSCs beyond their known optical benefits, depending on their position within the cell's architecture. When integrated into the selective contacts (HTL/ETL), these structures facilitate charge collection by increasing the contact area of these layers, thus improving the device efficiency. Conversely, when placed on the cell's front as structured transparent electrodes or encapsulant layers, these schemes can offer additional benefits, such as improved resistance to UV (and higher-energy) photons, which is vital for enhancing the stability of perovskite absorbers under the extreme conditions of space. Hence, advanced photonic management can enhance both the efficiency and radiation resilience of PSCs. Moreover, their inherent mechanical flexibility and lightweight characteristics make them ideal for large-area roll-out space PV installations. However, in case that the LT structures are the first ones interacting with the incident light, the implementation of LT structures onto perovskite PV remains an issue. Two main approaches are envisioned. To avoid structuring the perovskite absorber, the PSC layers deposition may be performed onto an underlying texture, for instance. To that end, it is advised to structure the first layer that interacts with light, that is, the front contact for adequate index matching. On the other hand, transferring methods offer pathways to enhance the performance and stability of perovskite cells, bridging the gap between experimental designs and practical applications, as addressed in this review. Among these methods, roll-to-roll lamination techniques avoid temperature, UV exposure, and solvents, thus being compatible with perovskite materials. With this, it is possible to couple advanced LT onto PSCs.

Coupling well-established PV technologies like silicon PVs with radiation-resistant perovskites, particularly FA-based variants, holds even higher promise for space applications owing to the potentially higher efficiencies of tandem designs. However, as referred above, challenges related to processing sensitive layers need to be addressed. While black silicon or fully textured architectures appear reliable for high power generation, prioritizing gentle photonic fabrication techniques, such as structuring-based methods, is vital for sustainability. These techniques will not only facilitate device thinning without compromising electrical performance but also support the growth of the LEO PV market. Additionally, photonic features could be combined with hydrophilic capping layers, which possess low-polar and high-dispersion properties, resulting in excellent film coverage and improved quality of the perovskite film. In terms of fabrication, high-throughput methods such as spray coating, slot die coating, and blade coating are preferred if they assure high-quality perovskite absorbers conformal to the underlying layers. To address front reflection losses, employing front wavelength-sized structures with low refractive index (e.g., PDMS front-pyramids) has proven to be a reliable pathway that does not significantly affect the sensitive perovskite cell layers.

In view of the extreme thermal and ultrahigh-vacuum conditions of space, comprehensive device modeling that simultaneously evaluates thermal plus radiation resistance and optoelectronic performance is key to design optimal space-deployable solar cells while minimizing the experimental costs associated with multiparameter testing. Effective thermal management, facilitated by thin (to avoid parasitic absorption) radiative cooling coatings, allows to dissipate heat from PV systems in space. Although research on this topic is limited, some investigations have proposed novel radiative cooling coatings under simulated space conditions. Further research should prioritize assessing the thermal management capabilities of radiative cooling coatings for emerging solar cell architectures, such as PSTSCs. On the other hand, modeling efforts should explore complex radiative cooling schemes for space applications, such as the 3D-ordered structures composed of radiation-resistant and thermally stable materials identified in this review (SiO_2/TiO_2/SiN/HfO_2) as effective platforms for radiative cooling. In fact, these photonic coolers already showed a synergistic effect between sub-bandgap wavelength filtering, incoupling of sub-bandgap photons (LT), and thermal emission of low-energy photons (thermal management). It is important to experimentally validate these schemes under simulated or actual space conditions, in view of translating theoretical findings into practical extraterrestrial applications. Among the aforementioned materials, wavelength-sized structures composed of high-index materials with optimized IR emission profiles (e.g., TiO_2) appear to be particularly promising for maintaining device stability under harsh conditions. They present promising capabilities for thermal management while their high absorption coefficients in the infrared spectrum enable efficient absorption and emission of infrared radiation. Moreover, these structures offer potential benefits to PV devices, such as the aforementioned antireflection and light-scattering effects, enhancing their performance via LT.

Finally, this review discusses the potential of spectrum modification strategies for PV applications, highlighting the integration of spectral-shifting materials composed of QDs into various solar cell technologies. For space applications, optimizing these spectral modification strategies presents unique research opportunities. While PSCs have recently emerged as the primary platform for QD incorporation, other technologies like c-Si and CIGS solar cells also benefit from this approach. In particular, developing QDs and spectral-shifting materials that can withstand high levels of radiation and extreme temperature fluctuations will be essential for reliable performance in space. Further research should focus on integrating UC and DC strategies with radiation-resistant materials and developing encapsulation methods that protect sensitive layers in extraterrestrial environments. Combining these advancements could offer a comprehensive approach to maximizing solar energy utilization across the UV-to-NIR spectrum, thus driving further improvements in the efficiency and stability of photovoltaic devices for both terrestrial and space missions. For instance, embedding QDs in a polymeric matrix on the front side of devices allows interaction with

UV photons, leading to DS toward the visible and consequently enhancing optical absorption. Nonetheless, further research is needed to clearly discern the mechanisms behind this enhancement, including LDS, light scattering, or plasmonic effects contributions. QDs made of CdSe, CdS, and ZnS are preferred due to fabrication ease, size tuning, and high quantum yield. Shelling QDs with a SiO_2 layer can enhance stability of the perovskite absorber while maintaining fluorescence. Utilizing UC and DC mechanisms in the hole and ETLs of PSCs can mitigate reflection losses and improve UV stability. Additionally, researchers may capitalize on ions with *f–d* transitions (e.g., Eu^{3+}) to address weak absorption and narrow excitation bands. The integration of UC and DC strategies offers a comprehensive approach to utilize the entire solar spectrum efficiently, from UV-to-NIR photons. Further research should focus on combining these strategies for maximum solar energy utilization, thus driving further advances in the efficiency and stability of space photovoltaic devices.

Each photonic strategy reviewed here offers unique benefits for optimizing the optoelectronic performance of PV devices in both terrestrial and extraterrestrial environments. Structuring methods, leveraging high throughput and soft lithography techniques, have demonstrated versatility and, in some cases, higher optoelectronic characteristics when compared to traditional texturing techniques (e.g., random texturization by chemical etching). However, the selection of a photonic approach should be tailored to its intended application. For instance, photonic coolers are specifically designed for effective radiative cooling in space, while micro- or nanopyramidal textures and wavelength-sized structures (sometimes used simultaneously) are employed to mitigate reflection losses and enhance light scattering toward the absorber. Mechanisms of DS and DC facilitate the absorption of high-energy UV photons, whereas UC is effective for low-energy NIR photons. Additionally, each photonic approach may provide unforeseen benefits, such as improved stability, enhanced quality of perovskite grain growth, and increased flexibility.

In summary, this review serves as a primer for comprehending the advancements and future trajectories of optical strategies in both terrestrial and extraterrestrial contexts. It contributes to the envisaged synergetic combination of different schemes, with the overarching goal of optimizing solar power generation in the next generation of photonic-enhanced photovoltaics.

Supporting Information

Supporting Information is available from the Wiley Online Library or from the author.

Acknowledgements

This work received funding from FCT (Fundação para a Ciência e Tecnologia, I.P.) under the projects LA/P/0037/2020, UIDP/50025/2020 and UIDB/50025/2020 of the Associate Laboratory Institute of Nanostructures, Nanomodelling and Nanofabrication—i3N and by the projects SpaceFlex (2022.01610.PTDC) and FlexSolar (PTDC/CTM-REF/1008/2020), as well as by M-ECO2 (Industrial cluster for advanced biofuel production, Ref. C644930471-00000041) cofinanced by PRR - Recovery and Resilience Plan of the European Union (Next Generation EU). The work was also supported by the European project X-STREAM (Horizon EU, ERC CoG, no. 101124803) and SYNERGY (H2020-WIDESPREAD-2020-5, CSA, grant no. 952169). I.S. and M.A. also acknowledge funding by FCT, I.P. through the grants 2023.03929.BD and SFRH/BD/148078/2019, respectively. Views and opinions expressed are those of the authors only and do not necessarily reflect those of the European Union or the European Research Council. Neither the European Union nor the granting authority can be held responsible for them.

Conflict of Interest

The authors declare no conflict of interest.

Author Contributions

Ivan M. Santos: investigation: (lead); validation (lead); writing—original draft (lead); writing—review & editing (equal). **Miguel Alexandre**: conceptualization (equal); data curation (equal); formal analysis (equal); software (equal); writing—review & editing (equal). **António T. Vicente**: formal analysis (equal); methodology (equal); validation (supporting); writing—original draft (supporting); writing—review & editing (equal). **Cristina Teixeira**: investigation (equal); methodology (supporting); validation (supporting); writing—original draft (supporting); writing—review & editing (supporting). **Eva Almeida**: data curation (supporting); methodology (supporting); software (supporting); writing—original draft (equal). **Elvira Fortunato**: funding acquisition (supporting); investigation (supporting); project administration (supporting); supervision (supporting). **Rodrigo Martins**: resources (lead); supervision (lead). **Hugo Águas**: funding acquisition (supporting); investigation (supporting); project administration (supporting); writing—review & editing (supporting). **Manuel J. Mendes**: conceptualization (equal); funding acquisition (lead); project administration (equal); resources (equal); supervision (equal); writing—review & editing (equal).

Keywords

light management, novel solar cell concepts, photonics, photovoltaics for space applications

Received: September 15, 2024
Revised: November 20, 2024
Published online: March 9, 2025

---

[1] Fraunhofer ISE, Photovoltaics Report **2023**, https://www.ise.fraunhofer.de/content/dam/ise/de/documents/publications/studies/Photovoltaics-Report.pdf.
[2] Spring 2023 – Solar Industry Update **2023**.
[3] W. Shockley, H. J. Queisser, *J. Appl. Phys.* **1961**, *32*, 510.
[4] S. Eyderman, S. John, M. Hafez, S. S. Al-Ameer, T. S. Al-Harby, Y. Al-Hadeethi, D. M. Bouwes, *J. Appl. Phys.* **2015**, *118*, 023103.
[5] M. J. Mendes, O. Sanchez-Sobrado, S. Haque, T. Mateus, H. Águas, E. Fortunato, R. Martins, in *Solar Cells and Light Management*, Elsevier, Amsterdam **2020**, pp. 315–354.
[6] M. J. Mendes, A. Araújo, A. Vicente, H. Águas, I. Ferreira, E. Fortunato, R. Martins, *Nano Energy* **2016**, *26*, 286.
[7] M. J. Mendes, S. Haque, O. Sanchez-Sobrado, A. Araújo, H. Águas, E. Fortunato, R. Martins, *iScience* **2018**, *3*, 238.
[8] T. M. Brenner, D. A. Egger, L. Kronik, G. Hodes, D. Cahen, *Nat. Rev. Mater.* **2016**, *1*, 15007.
[9] P. Kowalczewski, L. C. Andreani, *Sol. Energy Mater. Sol. Cells* **2015**, *143*, 260.

[10] I. M. Santos, M. Alexandre, V. D. Mihailetchi, J. A. Silva, T. Mateus, A. Mouquinho, J. Boane, A. T. Vicente, D. Nunes, U. D. Menda, H. Águas, E. Fortunato, R. Martins, M. J. Mendes, *Adv. Opt. Mater.* **2023**, *11*, 2300276.

[11] J. Zhang, W. Zhang, H.-M. Cheng, S. R. P. Silva, *Mater. Today* **2020**, *39*, 66.

[12] C. Chen, S. Zheng, H. Song, *Chem. Soc. Rev.* **2021**, *50*, 7250.

[13] T. Markvart, *J. Mater. Sci. Mater. Electron.* **1990**, *1*, 1.

[14] N. J. Mohr, J. J. Schermer, M. A. J. Huijbregts, A. Meijer, L. Reijnders, *Prog. Photovolt. Res. Appl.* **2007**, *15*, 163.

[15] M. A. Green, S. P. Bremner *Nat. Mater.* **2017**, *16*, 23.

[16] M. R. Reddy, *Sol. Energy Mater. Sol. Cells* **2003**, *77*, 175.

[17] I. Cardinaletti, T. Vangerven, S. Nagels, R. Cornelissen, D. Schreurs, J. Hruby, J. Vodnik, D. Devisscher, J. Kesters, J. D'Haen, A. Franquet, V. Spampinato, T. Conard, W. Maes, W. Deferme, J. V. Manca, *Sol. Energy Mater. Sol. Cells* **2018**, *182*, 121.

[18] L. K. Reb, M. Böhmer, B. Predeschly, S. Grott, C. L. Weindl, G. I. Ivandekic, R. Guo, C. Dreißigacker, R. Gernhäuser, A. Meyer, P. Müller-Buschbaum, *Joule* **2020**, *4*, 1880.

[19] C. T. Sah, High Efficiency Crystalline Silicon Solar Cells **1986**, https://ntrs.nasa.gov/citations/19870011978 (accessed: February 2024).

[20] A. Martí, G. L. Araújo, *Sol. Energy Mater. Sol. Cells* **1996**, *43*, 203.

[21] J. F. Geisz, R. M. France, K. L. Schulte, M. A. Steiner, A. G. Norman, H. L. Guthrey, M. R. Young, T. Song, T. Moriarty, *Nat. Energy* **2020**, *5*, 326.

[22] Best Research-Cell Efficiency Chart, https://www.nrel.gov/pv/cell-efficiency.html (accessed September 2024).

[23] A. W. Y. Ho-Baillie, H. G. J. Sullivan, T. A. Bannerman, H. P. Talathi, J. Bing, S. Tang, A. Xu, D. Bhattacharyya, I. H. Cairns, D. R. Mckenzie, *Adv. Mater. Technol.* **2022**, *7*, 2101059.

[24] I. F. Akyildiz, A. Kak, *IEEE Netw.* **2019**, *33*, 212.

[25] J. Keller, K. Kiselman, O. Donzel-Gargand, N. M. Martin, M. Babucci, O. Lundberg, E. Wallin, L. Stolt, M. Edoff, *Nat. Energy* **2024**, *9*, 467.

[26] A. S. R. Bati, Y. L. Zhong, P. L. Burn, M. K. Nazeeruddin, P. E. Shaw, M. Batmunkh, *Commun. Mater.* **2023**, *4*, 2.

[27] A. R. Kirmani, B. K. Durant, J. Grandidier, N. M. Haegel, M. D. Kelzenberg, Y. M. Lao, M. D. Mcgehee, L. Mcmillon-Brown, D. P. Ostrowski, T. J. Peshek, B. Rout, I. R. Sellers, M. Steger, D. Walker, D. M. Wilt, K. T. Vansant, J. M. Luther, *Joule* **2022**, *6*, 1015.

[28] State-of-the-Art of Small Spacecraft Technology – NASA, https://www.nasa.gov/smallsat-institute/sst-soa/ (accessed: January 2024).

[29] Impact Story: Roll-Out Solar Arrays – NASA, https://www.nasa.gov/directorates/stmd/impact-story-roll-out-solar-arrays/ (accessed: September 2024).

[30] Y. G. Tu, G. N. Xu, X. Y. Yang, Y. F. Zhang, Z. J. Li, R. Su, D. Y. Luo, W. Q. Yang, Y. Miao, R. Cai, L. H. Jiang, X. W. Du, Y. C. Yang, Q. S. Liu, Y. Gao, S. Zhao, W. Huang, Q. H. Gong, R. Zhu, *Sci. China Phys. Mech. Astron.* **2019**, *62*, 974221.

[31] J.-S. Huang, M. D. Kelzenberg, P. Espinet-González, C. Mann, D. Walker, A. Naqavi, N. Vaidya, E. Warmann, H. A. Atwater, in *2017 IEEE 44th Photovoltaic Specialist Conf. (PVSC)*, IEEE, Piscataway, NJ **2017**, pp. 1248–1252.

[32] Y. Miyazawa, M. Ikegami, H.-W. Chen, T. Ohshima, M. Imaizumi, K. Hirose, T. Miyasaka, *iScience* **2018**, *2*, 148.

[33] F. Lang, M. Jošt, J. Bundesmann, A. Denker, S. Albrecht, G. Landi, H.-C. Neitzert, J. Rappich, N. H. Nickel, *Energy Environ. Sci.* **2019**, *12*, 1634.

[34] F. Lang, M. Jošt, K. Frohna, E. Köhnen, A. Al-Ashouri, A. R. Bowman, T. Bertram, A. B. Morales-Vilches, D. Koushik, E. M. Tennyson, K. Galkowski, G. Landi, M. Creatore, B. Stannowski, C. A. Kaufmann, J. Bundesmann, J. Rappich, B. Rech, A. Denker, S. Albrecht, H.-C. Neitzert, N. H. Nickel, S. D. Stranks, *Joule* **2020**, *4*, 1054.

[35] T. H. Schloemer, T. S. Gehan, J. A. Christians, D. G. Mitchell, A. Dixon, Z. Li, K. Zhu, J. J. Berry, J. M. Luther, A. Sellinger, *ACS Energy Lett.* **2019**, *4*, 473.

[36] J. A. Christians, P. Schulz, J. S. Tinkham, T. H. Schloemer, S. P. Harvey, B. J. Tremolet De Villers, A. Sellinger, J. J. Berry, J. M. Luther, *Nat. Energy* **2018**, *3*, 68.

[37] M. De Bastiani, V. Larini, R. Montecucco, G. Grancini, *Energy Environ. Sci.* **2023**, *16*, 421.

[38] Z. Li, Y. Zhao, X. Wang, Y. Sun, Z. Zhao, Y. Li, H. Zhou, Q. Chen, *Joule* **2018**, *2*, 1559.

[39] C. O. Ramírez Quiroz, Y. Shen, M. Salvador, K. Forberich, N. Schrenker, G. D. Spyropoulos, T. Heumüller, B. Wilkinson, T. Kirchartz, E. Spiecker, P. J. Verlinden, X. Zhang, M. A. Green, A. Ho-Baillie, C. J. Brabec, *J. Mater. Chem. A* **2018**, *6*, 3583.

[40] K. A. Bush, A. F. Palmstrom, Z. J. Yu, M. Boccard, R. Cheacharoen, J. P. Mailoa, D. P. Mcmeekin, R. L. Z. Hoye, C. D. Bailie, T. Leijtens, I. M. Peters, M. C. Minichetti, N. Rolston, R. Prasanna, S. Sofia, D. Harwood, W. Ma, F. Moghadam, H. J. Snaith, T. Buonassisi, Z. C. Holman, S. F. Bent, M. D. Mcgehee, *Nat. Energy* **2017**, *2*, 17009.

[41] F. Sahli, J. Werner, B. A. Kamino, M. Bräuninger, R. Monnard, B. Paviet-Salomon, L. Barraud, L. Ding, J. J. Diaz Leon, D. Sacchetto, G. Cattaneo, M. Despeisse, M. Boccard, S. Nicolay, Q. Jeangros, B. Niesen, C. Ballif, *Nat. Mater.* **2018**, *17*, 820.

[42] T. Sumita, M. Imaizumi, S. Matsuda, T. Ohshima, A. Ohi, H. Itoh, *Nucl. Instrum. Methods Phys. Res. Sect. B* **2003**, *206*, 448.

[43] Z. Jiang, L. He, Z. Yang, H. Qiu, X. Chen, X. Yu, W. Li, *Nat. Commun.* **2023**, *14*, 827.

[44] A. L. Pellegrino, C. Tudisco, F. Lo Presti, E. Milan, A. Speghini, G. G. Condorelli, G. Malandrino, *Nano Energy* **2023**, *116*.

[45] H. Wu, J. Zhang, C. Jiang, Z. Zhai, *Infrared Phys. Technol.* **2023**, *133*.

[46] X. Li, F. Xie, S. Rafique, H. Wang, L. Deng, Z. Shi, Y. Wang, X. Zhang, K. Liu, Y. Wang, Y. Pan, F. Liu, C. Li, T. Hu, J. Wang, A. Yu, J. Tang, Y. Zhan, *Nano Energy* **2023**, *114*.

[47] Q. Wang, R. Fu, T. Sun, M. Liu, S. Sun, H. Jiang, Y. Zhang, D. Liu, Y. Chen, H. Zhong, *Sol. Energy Mater. Sol. Cells* **2023**, *259*.

[48] S. Gu, Z. Lu, S. Zou, C. Wu, C. Peng, M. Ni, Z. Chen, H. Huang, H. Sun, H. Wang, X. Zhang, X. Su, *Sol. RRL* **2023**, *7*, 2300215.

[49] N. Liu, H. Xue, Y. Ji, J. Wang, *J. Alloys Compd.* **2018**, *747*, 696.

[50] E. Klampaftis, D. Ross, K. R. Mcintosh, B. S. Richards, *Sol. Energy Mater. Sol. Cells* **2009**, *93*, 1182.

[51] Y. Tu, J. Wu, G. Xu, X. Yang, R. Cai, Q. Gong, R. Zhu, W. Huang, *Adv. Mater.* **2021**, *33*, 2006545.

[52] G. Perrakis, A. C. Tasolamprou, G. Kenanakis, E. N. Economou, S. Tzortzakis, M. Kafesaki, *Sci. Rep.* **2021**, *11*, 11552.

[53] M. Lee, G. Kim, Y. Jung, K. R. Pyun, J. Lee, B.-W. Kim, S. H. Ko, *Light Sci. Appl.* **2023**, *12*, 134.

[54] E. Rephaeli, A. Raman, S. Fan, *Nano Lett.* **2013**, *13*, 1457.

[55] K. Koshelev, G. Favraud, A. Bogdanov, Y. Kivshar, A. Fratalocchi, *Nanophotonics* **2019**, *8*, 725.

[56] M. Zeyghami, D. Y. Goswami, E. Stefanakos, *Sol. Energy Mater. Sol. Cells* **2018**, *178*, 115.

[57] G. Perrakis, A. C. Tasolamprou, G. Kenanakis, E. N. Economou, S. Tzortzakis, M. Kafesaki, *ACS Photonics* **2022**, *9*, 1327.

[58] D. Wang, Y.-H. Ye, Y. Zhu, in *Tenth International Conference on Information Optics and Photonics* (Ed: Y. Yang), SPIE, Beijing, China **2018**, p. 179.

[59] P. Gupta, Y. Kim, J. Im, G. Kang, A. M. Urbas, K. Kim, *ACS Appl. Energy Mater.* **2021**, *4*, 9304.

[60] L. Zhou, J. Zhao, H. Huang, F. Nan, G. Zhou, Q. Ou, *ACS Photonics* **2021**, *8*, 3301.

[61] J.-W. Cho, S.-J. Park, S.-J. Park, Y.-B. Kim, K.-Y. Kim, D. Bae, S.-K. Kim, *ACS Photonics* **2020**, *7*, 2748.

[62] D. D. Smith, G. Reich, M. Baldrias, M. Reich, N. Boitnott, G. Bunea, in *2016 IEEE 43rd Photovoltaic Specialists Conf. (PVSC)*, IEEE, Portland, OR **2016**, pp. 3351–3355.
[63] K. Yoshikawa, H. Kawasaki, W. Yoshida, T. Irie, K. Konishi, K. Nakano, T. Uto, D. Adachi, M. Kanematsu, H. Uzu, K. Yamamoto, *Nat. Energy* **2017**, *2*, 17032.
[64] H. Lin, M. Yang, X. Ru, G. Wang, S. Yin, F. Peng, C. Hong, M. Qu, J. Lu, L. Fang, C. Han, P. Procel, O. Isabella, P. Gao, Z. Li, X. Xu, *Nat. Energy* **2023**, *8*, 789.
[65] T. E. Scheul, E. Khorani, T. Rahman, M. D. B. Charlton, S. A. Boden, *Prog. Photovolt. Res. Appl.* **2020**, *28*, 1248.
[66] M. L. Addonizio, A. Antonaia, L. Fusco, *Appl. Surf. Sci.* **2019**, *467–468*, 143.
[67] D. Zhiqiang, L. Meicheng, T. M. Chonto, *Nanoscale Res. Lett.* **2018**, *13*, 192.
[68] A. Ingenito, O. Isabella, M. Zeman, *ACS Photonics* **2014**, *1*, 270.
[69] R. Islam, K. Saraswat, *Sci. Rep.* **2018**, *8*, 8863.
[70] M. Garín, T. P. Pasanen, G. López, V. Vähänissi, K. Chen, I. Martín, H. Savin, *Small* **2023**, *19*, 2302250.
[71] M. J. Kerr, A. Cuevas, P. Campbell, *Prog. Photovolt. Res. Appl.* **2003**, *11*, 97.
[72] A. Richter, M. Hermle, S. W. Glunz, *IEEE J. Photovolt.* **2013**, *3*, 1184.
[73] P. Procel, A. Ingenito, R. De Rose, S. Pierro, F. Crupi, M. Lanuzza, G. Cocorullo, O. Isabella, M. Zeman, *Prog. Photovolt. Res. Appl.* **2017**, *25*, 452.
[74] M. D. Lammert, R. J. Schwartz, *IEEE Trans. Electron Devices* **1977**, *24*, 337.
[75] R. M. Swanson, *Sol. Cells* **1986**, *17*, 85.
[76] I. Massiot, A. Cattoni, S. Collin, *Nat. Energy* **2020**, *5*, 959.
[77] K. Masuko, M. Shigematsu, T. Hashiguchi, D. Fujishima, M. Kai, N. Yoshimura, T. Yamaguchi, Y. Ichihashi, T. Mishima, N. Matsubara, T. Yamanishi, T. Takahama, M. Taguchi, E. Maruyama, S. Okamoto, *IEEE J. Photovolt.* **2014**, *4*, 1433.
[78] D. Adachi, J. L. Hernández, K. Yamamoto, *Appl. Phys. Lett.* **2015**, *107*, 233506.
[79] S. Zhong, B. Liu, Y. Xia, J. Liu, J. Liu, Z. Shen, Z. Xu, C. Li, *Sol. Energy Mater. Sol. Cells* **2013**, *108*, 200.
[80] S. Jeong, M. D. Mcgehee, Y. Cui, *Nat. Commun.* **2013**, *4*, 2950.
[81] H. Savin, P. Repo, G. Von Gastrow, P. Ortega, E. Calle, M. Garín, R. Alcubilla, *Nat. Nanotechnol.* **2015**, *10*, 624.
[82] M. Otto, M. Kroll, T. Käsebier, R. Salzer, A. Tünnermann, R. B. Wehrspohn, *Appl. Phys. Lett.* **2012**, *100*, 191603.
[83] O. Sanchez-Sobrado, M. J. Mendes, T. Mateus, J. Costa, D. Nunes, H. Aguas, E. Fortunato, R. Martins, *Sol. Energy* **2020**, *196*, 92.
[84] S. Haque, M. Alexandre, C. Baretzky, D. Rossi, F. De Rossi, A. T. Vicente, F. Brunetti, H. Águas, R. A. S. Ferreira, E. Fortunato, M. Auf Der Maur, U. Würfel, R. Martins, M. J. Mendes, *ACS Photonics* **2022**, *9*, 2408.
[85] O. L. Muskens, J. G. Rivas, R. E. Algra, E. P. A. M. Bakkers, A. Lagendijk, *Nano Lett.* **2008**, *8*, 2638.
[86] L. Hu, G. Chen, *Nano Lett.* **2007**, *7*, 3249.
[87] K. Peng, Y. Xu, Y. Wu, Y. Yan, S.-T. Lee, J. Zhu, *Small* **2005**, *1*, 1062.
[88] C. Kim, J. Lee, S. Lim, C. Jeong, *Sol. Energy* **2015**, *116*, 265.
[89] B.-R. Huang, S.-C. Hung, C.-H. Hsu, C.-W. Tu, W.-L. Yang, *Mater. Res. Bull.* **2016**, *80*, 209.
[90] I. R. Putra, J.-Y. Li, C.-Y. Chen, *Appl. Surf. Sci.* **2019**, *478*, 725.
[91] S. G. Bailey, R. Raffaelle, K. Emery, *Prog. Photovolt. Res. Appl.* **2002**, *10*, 399.
[92] R. Surampudi, J. Blosiu, P. Stella, J. Elliott, J. Castillo, T. Yi, J. Lyons, M. Piszczor, J. Mcnatt, C. Taylor, S. Liu, E. Plichta, P. M. Beauchamp, J. A. Cutts, *Strategic Mission and Advanced Concepts of NASA*, NASA, Washington, DC **2017**.
[93] P. Iles, *Sol. Energy Mater. Sol. Cells* **2001**, *68*, 1.
[94] R. Verduci, V. Romano, G. Brunetti, N. Yaghoobi Nia, A. Di Carlo, G. D'angelo, C. Ciminelli, *Adv. Energy Mater.* **2022**, *12*, 2200125.
[95] A. Rehman, S. H. Lee, S. H. Lee, *J. Korean Phys. Soc.* **2016**, *68*, 593.
[96] J. Lindmayer, J. F. Allison, *Sol. Cells* **1990**, *29*, 151.
[97] R. Ardnt, *Springer* **1974**, *4*, 41.
[98] T. Matsutani, T. Saga, H. Ueyama, Y. Hagihara, T. Hirano, A. Suzuki, *Jpn. J. Appl. Phys.* **1982**, *21*, 23.
[99] A. Suzuki, *Sol. Energy Mater. Sol. Cells* **1998**, *50*, 289.
[100] A. W. Jianhua Zhao, P. P. Altermatt, S. R. Wenham, M. A. Green, in *Proc. of 1994 IEEE 1st World Conf. on Photovoltaic Energy Conversion - WCPEC (A Joint Conf. of PVSC, PVSEC and PSEC)*, IEEE, Piscataway, NJ **1994**, Vol. *2*, pp. 1477–1480.
[101] M. A. Green, *Prog. Photovolt. Res. Appl.* **2009**, *17*, 183.
[102] M. Yamaguchi, S. J. Taylor, S. Matsuda, O. Kawasaki, *Appl. Phys. Lett.* **1996**, *68*, 3141.
[103] T. Hisamatsu, O. Kawasaki, S. Matsuda, T. Nakao, Y. Wakow, *Sol. Energy Mater. Sol. Cells* **1998**, *50*, 331.
[104] S. Z. Karazhanov, *Sol. Energy Mater. Sol. Cells* **2001**, *69*, 53.
[105] S. Z. Karazhanov, *Appl. Phys. Lett.* **2000**, *76*, 2689.
[106] A. Hamache, N. Sengouga, A. Meftah, *Energy Procedia* **2014**, *50*, 139.
[107] H. Presting, J. Konle, D. Behammer, A. Gruhle, P. Uebele, G. Strobl, in *Conf. Record of the Twenty-Eighth IEEE Photovoltaic Specialists Conf. - 2000 (Cat. No.0°CH37036) 1293–1296*, IEEE, Piscataway, NJ **2000**.
[108] Y. Tonomura, M. Hagino, H. Washio, M. Kaneiwa, T. Saga, O. Anzawa, K. Aoyama, K. Shinozaki, S. Matsuda, *Sol. Energy Mater. Sol. Cells* **2001**, *66*, 551.
[109] Y. Lu, Q. Shao, H. Yue, F. Yang, *IEEE Access* **2019**, *7*, 93473.
[110] W. Riedler, K. Torkar, F. Rüdenauer, M. Fehringer, A. Pedersen, R. Schmidt, R. J. L. Grard, H. Arends, B. T. Narheim, J. Troim, R. Torbert, R. C. Olsen, E. Whipple, R. Goldstein, N. Valavanoglou, H. U. A. Zhao, *Space Sci. Rev.* **1997**, *79*, 271.
[111] A. Bermudez-Garcia, P. Voarino, O. Raccurt, *Appl. Energy* **2021**, *290*, 116757.
[112] X. Tan, Y. Tu, C. Deng, A. Czarnowski, W. Yan, M. Ye, Y. Yi, *Opt. Commun.* **2018**, *426*, 584.
[113] A. Mavrokefalos, S. E. Han, S. Yerci, M. S. Branham, G. Chen, *Nano Lett.* **2012**, *12*, 2792.
[114] V. Depauw, Y. Qiu, K. Van Nieuwenhuysen, I. Gordon, J. Poortmans, *Prog. Photovolt. Res. Appl.* **2011**, *19*, 844.
[115] J. He, P. Gao, M. Liao, X. Yang, Z. Ying, S. Zhou, J. Ye, Y. Cui, *ACS Nano* **2015**, *9*, 6522.
[116] F. Duerinckx, I. Kuzma-Filipek, K. Van Nieuwenhuysen, G. Beaucarne, J. Poortmans, *Prog. Photovolt. Res. Appl.* **2008**, *16*, 399.
[117] Y. Li, H. Sai, T. Matsui, Z. Xu, V. Nguyen, Y. Kurokawa, N. Usami, *Sol. RRL* **2022**, *6*.
[118] A. Rosell, I. Martin, M. Garin, G. Lopez, R. Alcubilla, *IEEE J. Photovolt.* **2020**, *10*, 351.
[119] M. A. Green, *Prog. Photovolt. Res. Appl.* **2002**, *10*, 235.
[120] J. R. Srour, G. J. Vendura, D. H. Lo, C. M. C. Toporow, M. Dooley, R. P. Nakano, E. E. King, *IEEE Trans. Nucl. Sci.* **1998**, *45*, 2624.
[121] M. Menichelli, M. Bizzarri, M. Boscardin, L. Calcagnile, M. Caprai, A. P. Caricato, G. A. P. Cirrone, M. Crivellari, I. Cupparo, G. Cuttone, S. Dunand, L. Fanò, B. Gianfelici, O. Hammad, M. Ionica, K. Kanxheri, M. Large, G. Maruccio, A. G. Monteduro, F. Moscatelli, A. Morozzi, A. Papi, D. Passeri, M. Pedio, M. Petasecca, G. Petringa, F. Peverini, G. Quarta, S. Rizzato, A. Rossi, et al., *Nucl. Instrum. Methods Phys. Res. Sect. Accel. Spectrometers Detect. Assoc. Equip.* **2023**, *1052*, 168308.
[122] Z. Zhang, B. Bai, X. Li, Y. Liu, C. Sun, Y. Zhang, *IEEE Antennas Wirel. Propag. Lett.* **2020**, *19*, 2320.
[123] P. G. Linares, E. Antolín, A. Martí, *Sol. Energy Mater. Sol. Cells* **2019**, *194*, 54.

[124] S. Bhattacharya, I. Baydoun, M. Lin, S. John, *Phys. Rev. Appl.* **2019**, *11*, 014005.
[125] A. Polman, M. Knight, E. C. Garnett, B. Ehrler, W. C. Sinke, *Science* **2016**, *352*, aad4424.
[126] P. Balaji, W. J. Dauksher, S. G. Bowden, A. Augusto, in *2019 IEEE 46th Photovoltaic Specialists Conf. (PVSC)*, IEEE, Piscataway, NJ **2019**, pp. 1089–1092.
[127] M. M. Hilali, S. Saha, E. Onyegam, R. Rao, L. Mathew, S. K. Banerjee, *Appl. Opt.* **2014**, *53*, 6140.
[128] R. Cariou, M. Labrune, P. Roca I Cabarrocas, *Sol. Energy Mater. Sol. Cells* **2011**, *95*, 2260.
[129] A. Gaucher, A. Cattoni, C. Dupuis, W. Chen, R. Cariou, M. Foldyna, Loï. Lalouat, E. Drouard, C. Seassal, P. Roca I Cabarrocas, S. Collin, *Nano Lett.* **2016**, *16*, 5358.
[130] M. Xue, K. N. Nazif, Z. Lyu, J. Jiang, C.-Y. Lu, N. Lee, K. Zang, Y. Chen, T. Zheng, T. I. Kamins, M. L. Brongersma, K. C. Saraswat, J. S. Harris, *Nano Energy* **2020**, *70*.
[131] V. Depauw, C. Trompoukis, I. Massiot, W. Chen, A. Dmitriev, P. R. Cabarrocas, I. Gordon, J. Poortmans, *Nano Futur.* **2017**, *1*, 021001.
[132] O. Isabella, S. Dobrovolskiy, G. Kroon, M. Zeman, *J. Non-Cryst. Solids* **2012**, *358*, 2295.
[133] S. Eyderman, S. John, A. Deinega, *J. Appl. Phys.* **2013**, *113*, 154315.
[134] S. Zhou, Z. Yang, P. Gao, X. Li, X. Yang, D. Wang, J. He, Z. Ying, J. Ye, *Nanoscale Res. Lett.* **2016**, *11*, 194.
[135] E. R. Martins, J. Li, Y. K. Liu, V. Depauw, Z. Chen, J. Zhou, T. F. Krauss, *Nat. Commun.* **2013**, *4*, 2665.
[136] B. K. Durant, H. Afshari, S. Singh, B. Rout, G. E. Eperon, I. R. Sellers, *ACS Energy Lett.* **2021**, *6*, 2362.
[137] W. Delmas, S. Erickson, J. Arteaga, M. Woodall, M. Scheibner, T. S. Krause, K. Crowley, K. T. Vansant, J. M. Luther, J. N. Williams, J. Mcnatt, T. J. Peshek, L. Mcmillon-Brown, S. Ghosh, *Adv. Energy Mater.* **2023**, *13*, 2203920.
[138] D. Yu, P. Wang, F. Cao, Y. Gu, J. Liu, Z. Han, B. Huang, Y. Zou, X. Xu, H. Zeng, *Nat. Commun.* **2020**, *11*, 3395.
[139] News Release: Thin, Lightweight Layer Provides Radiation Barrier for Perovskites in Space, Protection From Elements on Earth, https://www.nrel.gov/news/press/2023/news-release-thin-lightweight-layer-provides-radiation-barrier-for-perovskites-in-space-protection-from-elements-on-earth.html (accessed: March 2024).
[140] J. Yang, Q. Bao, L. Shen, L. Ding, *Nano Energy* **2020**, *76*, 105019.
[141] A. Al-Ashouri, E. Köhnen, B. Li, A. Magomedov, H. Hempel, P. Caprioglio, J. A. Márquez, A. B. Morales Vilches, E. Kasparavicius, J. A. Smith, N. Phung, D. Menzel, M. Grischek, L. Kegelmann, D. Skroblin, C. Gollwitzer, T. Malinauskas, M. Jošt, G. Matič, B. Rech, R. Schlatmann, M. Topič, L. Korte, A. Abate, B. Stannowski, D. Neher, M. Stolterfoht, T. Unold, V. Getautis, S. Albrecht, *Science* **2020**, *370*, 1300.
[142] J. Zheng, H. Wei, Z. Ying, X. Yang, J. Sheng, Z. Yang, Y. Zheng, J. Ye, *Adv. Energy Mater.* **2023**, *13*.
[143] W. Raja, M. De Bastiani, T. G. Allen, E. Aydin, A. Razzaq, A. Rehman, E. Ugur, A. Babayigit, A. S. Subbiah, F. H. Isikgor, S. De Wolf, *Nanophotonics* **2021**, *10*, 2023.
[144] S. Haque, M. J. Mendes, O. Sanchez-Sobrado, H. Águas, E. Fortunato, R. Martins, *Nano Energy* **2019**, *59*, 91.
[145] O. Sanchez-Sobrado, M. J. Mendes, S. Haque, T. Mateus, H. Aguas, E. Fortunato, R. Martins, *J. Mater. Chem. C* **2019**, *7*, 6456.
[146] A. Peer, R. Biswas, J.-M. Park, R. Shinar, J. Shinar, *Opt. Express* **2017**, *25*, 10704.
[147] S. M. Kang, S. Jang, J.-K. Lee, J. Yoon, D.-E. Yoo, J.-W. Lee, M. Choi, N.-G. Park, *Small* **2016**, *12*, 2443.
[148] S.-J. Ha, J. H. Heo, S. H. Im, J. H. Moon, *J. Mater. Chem. A* **2017**, *5*, 1972.
[149] T. K. Nguyen, P. T. Dang, K. Q. Le, *J. Opt.* **2016**, *18*, 125901.
[150] U. W. Paetzold, W. Qiu, F. Finger, J. Poortmans, D. Cheyns, *Appl. Phys. Lett.* **2015**, *106*, 173101.
[151] J. Wei, R.-P. Xu, Y.-Q. Li, C. Li, J.-D. Chen, X.-D. Zhao, Z.-Z. Xie, C.-S. Lee, W.-J. Zhang, J.-X. Tang, *Adv. Energy Mater.* **2017**, *7*, 1700492.
[152] B. Dudem, J. H. Heo, J. W. Leem, J. S. Yu, S. H. Im, *J. Mater. Chem. A* **2016**, *4*, 7573.
[153] Y. Luo, S. Liu, N. Barange, L. Wang, F. So, *Small* **2016**, *12*, 6346.
[154] J. Hao, H. Hao, J. Li, L. Shi, T. Zhong, C. Zhang, J. Dong, J. Xing, H. Liu, Z. Zhang, *Nanomaterials* **2018**, *8*, 815.
[155] R. T. Ginting, S. Kaur, D.-K. Lim, J.-M. Kim, J. H. Lee, S. H. Lee, J.-W. Kang, *ACS Appl. Mater. Interfaces* **2017**, *9*, 36111.
[156] M. Long, Z. Chen, T. Zhang, Y. Xiao, X. Zeng, J. Chen, K. Yan, J. Xu, *Nanoscale* **2016**, *8*, 6290.
[157] M. Vasilopoulou, W. Jose da Silva, A. Soultati, H. P. Kim, B. S. Kim, Y. Reo, A. E. Ximim Gavim, J. Conforto, F. K. Schneider, M. Felippi, L. C. Palilis, D. Davazoglou, P. Argitis, T. Stergiopoulos, A. Fakharuddin, J. Jang, N. Gasparini, M. K. Nazeeruddin, Y.-Y. Noh, A. Rashid bin Mohd Yusoff, *Cell Rep. Phys. Sci.* **2022**, *3*.
[158] D. I. Kim, J. W. Lee, R. H. Jeong, J.-H. Yu, J. W. Yang, S.-H. Nam, J.-H. Boo, *Appl. Surf. Sci.* **2019**, *487*, 409.
[159] A. Jangjoy, S. Matloub, *Sol. Energy* **2022**, *242*, 10.
[160] A. Jangjoy, S. Matloub, *Opt. Express* **2023**, *31*, 19102.
[161] M. I. Hossain, M. Shahiduzzaman, A. M. Saleque, M. R. Huqe, W. Qarony, S. Ahmed, M. Akhtaruzzaman, D. Knipp, Y. H. Tsang, T. Taima, J. A. Zapien, *Sol. RRL* **2021**, *5*.
[162] U. Mehmood, A. Al-Ahmed, M. Afzaal, F. A. Al-Sulaiman, M. Daud, *Renew. Sustain. Energy Rev.* **2017**, *78*, 1.
[163] H. Uratani, K. Yamashita, *J. Phys. Chem. Lett.* **2017**, *8*, 742.
[164] M. M. Tavakoli, K.-H. Tsui, Q. Zhang, J. He, Y. Yao, D. Li, Z. Fan, *ACS Nano* **2015**, *9*, 10287.
[165] L. Jiang, W. Chen, J. Zheng, L. Zhu, L. Mo, Z. Li, L. Hu, T. Hayat, A. Alsaedi, C. Zhang, S. Dai, *ACS Appl. Mater. Interfaces* **2017**, *9*, 26958.
[166] J. Jin, H. Li, C. Chen, B. Zhang, W. Bi, Z. Song, L. Xu, B. Dong, H. Song, Q. Dai, *Energy Mater.* **2018**, *1*, 2096.
[167] A. Tooghi, D. Fathi, M. Eskandari, *Sci. Rep.* **2020**, *10*. b) A. Tooghi, D. Fathi, M. Eskandari, *Sci. Rep.* **2020**, *10*.
[168] W. Qarony, M. I. Hossain, R. Dewan, S. Fischer, V. B. Meyer-Rochow, A. Salleo, D. Knipp, Y. H. Tsang, *Adv. Theory Simul.* **2018**, *1*, 1800030.
[169] R. Tian, S. Zhou, Y. Meng, C. Liu, Z. Ge, *Adv. Mater.* **2024**, 2311473.
[170] M. Mujahid, C. Chen, W. Hu, Z.-K. Wang, Y. Duan, *Sol. RRL* **2020**, *4*, 1900556.
[171] H. Liang, W. Yang, J. Xia, H. Gu, X. Meng, G. Yang, Y. Fu, B. Wang, H. Cai, Y. Chen, S. Yang, C. Liang, *Adv. Sci.* **2023**, *10*, 2304733.
[172] X. Li, P. Li, Z. Wu, D. Luo, H.-Y. Yu, Z.-H. Lu, *Mater. Rep. Energy* **2021**, *1*, 100001.
[173] A. Balilonda, Z. Li, Y. Fu, F. Zabihi, S. Yang, X. Huang, X. Tao, W. Chen, *J. Mater. Chem. C* **2022**, *10*, 6957.
[174] X. Zhang, X. Liu, Y. Huang, B. Sun, Z. Liu, G. Liao, T. Shi, *Front. Mech. Eng.* **2023**, *18*, 33.
[175] Y. Ma, Z. Lu, X. Su, G. Zou, Q. Zhao, *Adv. Energy Sustain. Res.* **2023**, *4*.
[176] D. Wang, W. Cheng, C. Wang, M. Zhou, W. Tian, L. Li, *Laser Photonics Rev.* **2023**, *17*, 2200641.
[177] S. Cong, G. Zou, Y. Lou, H. Yang, Y. Su, J. Zhao, C. Zhang, P. Ma, Z. Lu, H. Fan, Z. Huang, *Nano Lett.* **2019**, *19*, 3676.
[178] Z. Wu, P. Li, J. Zhao, T. Xiao, H. Hu, P. Sun, Z. Wu, J. Hao, C. Sun, H. Zhang, Z. Huang, Z. Zheng, *Adv. Mater. Interfaces* **2021**, *8*, 2001512.
[179] Q. Sun, J.-D. Chen, J.-W. Zheng, T.-Y. Qu, T.-Y. Jin, Y.-Q. Li, J.-X. Tang, *Adv. Opt. Mater.* **2019**, *7*, 1900847.

[180] Y. Li, L. Meng, Y. Yang, G. Xu, Z. Hong, Q. Chen, J. You, G. Li, Y. Yang, Y. Li, *Nat. Commun.* **2016**, *7*, 10214.
[181] P. Li, Z. Wu, H. Hu, Y. Zhang, T. Xiao, X. Lu, Z. Ren, G. Li, Z. Wu, J. Hao, H.-l. Zhang, Z. Zheng, *ACS Appl. Mater. Interfaces* **2020**, *12*, 26050.
[182] S. W. Jin, Y. H. Lee, K. M. Yeom, J. Yun, H. Park, Y. R. Jeong, S. Y. Hong, G. Lee, S. Y. Oh, J. H. Lee, J. H. Noh, J. S. Ha, *ACS Appl. Mater. Interfaces* **2018**, *10*, 30706.
[183] M. H. Futscher, B. Ehrler, *ACS Energy Lett.* **2016**, *1*, 863.
[184] S. Akhil, S. Akash, A. Pasha, B. Kulkarni, M. Jalalah, M. Alsaiari, F. A. Harraz, R. G. Balakrishna, *Mater. Des.* **2021**, *211*, 110138.
[185] E. Köhnen, M. Jošt, A. B. Morales-Vilches, P. Tockhorn, A. Al-Ashouri, B. Macco, L. Kegelmann, L. Korte, B. Rech, R. Schlatmann, B. Stannowski, S. Albrecht, *Sustainable Energy Fuels* **2019**, *3*, 1995.
[186] K. A. Bush, S. Manzoor, K. Frohna, Z. J. Yu, J. A. Raiford, A. F. Palmstrom, H.-P. Wang, R. Prasanna, S. F. Bent, Z. C. Holman, M. D. Mcgehee, *ACS Energy Lett.* **2018**, *3*, 2173.
[187] M. Jošt, E. Köhnen, A. B. Morales-Vilches, B. Lipovšek, K. Jäger, B. Macco, A. Al-Ashouri, J. Krč, L. Korte, B. Rech, R. Schlatmann, M. Topič, B. Stannowski, S. Albrecht, *Energy Environ. Sci.* **2018**, *11*, 3511.
[188] X. Hu, X. Meng, L. Zhang, Y. Zhang, Z. Cai, Z. Huang, M. Su, Y. Wang, M. Li, F. Li, X. Yao, F. Wang, W. Ma, Y. Chen, Y. Song, *Joule* **2019**, *3*, 2205.
[189] D. Zhao, C. Wang, Z. Song, Y. Yu, C. Chen, X. Zhao, K. Zhu, Y. Yan, *ACS Energy Lett.* **2018**, *3*, 305.
[190] D. Yang, R. Yang, S. Priya, S. F. Liu, *Angew. Chem.* **2019**, *131*, 4512.
[191] D. A. Jacobs, M. Langenhorst, F. Sahli, B. S. Richards, T. P. White, C. Ballif, K. R. Catchpole, U. W. Paetzold, *J. Phys. Chem. Lett.* **2019**, *10*, 3159.
[192] L. Duan, D. Walter, N. Chang, J. Bullock, D. Kang, S. P. Phang, K. Weber, T. White, D. Macdonald, K. Catchpole, H. Shen, *Nat. Rev. Mater.* **2023**, *8*, 261.
[193] E. Aydin, T. G. Allen, M. De Bastiani, L. Xu, J. Ávila, M. Salvador, E. Van Kerschaver, S. De Wolf, *Nat. Energy* **2020**, *5*, 851.
[194] J. Ávila, C. Momblona, P. P. Boix, M. Sessolo, H. J. Bolink, *Joule* **2017**, *1*, 431.
[195] M. Ju, K. Mallem, S. Dutta, N. Balaji, D. Oh, E.-C. Cho, Y. H. Cho, Y. Kim, J. Yi, *Mater. Sci. Semicond. Process.* **2018**, *85*, 68.
[196] C. T. Nguyen, K. Koyama, H. T. C. Tu, K. Ohdaira, H. Matsumura, *J. Mater. Res.* **2018**, *33*, 1515.
[197] D. K. Mohamad, J. Griffin, C. Bracher, A. T. Barrows, D. G. Lidzey, *Adv. Energy Mater.* **2016**, *6*, 1600994.
[198] J. H. Heo, M. H. Lee, M. H. Jang, S. H. Im, *J. Mater. Chem. A* **2016**, *4*, 17636.
[199] C. Zuo, D. Vak, D. Angmo, L. Ding, M. Gao, *Nano Energy* **2018**, *46*, 185.
[200] K. Hwang, Y.-S. Jung, Y.-J. Heo, F. H. Scholes, S. E. Watkins, J. Subbiah, D. J. Jones, D.-Y. Kim, D. Vak, *Adv. Mater.* **2015**, *27*, 1241.
[201] Y. Deng, X. Zheng, Y. Bai, Q. Wang, J. Zhao, J. Huang, *Nat. Energy* **2018**, *3*, 560.
[202] W.-Q. Wu, Z. Yang, P. N. Rudd, Y. Shao, X. Dai, H. Wei, J. Zhao, Y. Fang, Q. Wang, Y. Liu, Y. Deng, X. Xiao, Y. Feng, J. Huang, *Sci. Adv.* **2019**, *5*, eaav8925.
[203] B. Chen, Z. J. Yu, S. Manzoor, S. Wang, W. Weigand, Z. Yu, G. Yang, Z. Ni, X. Dai, Z. C. Holman, J. Huang, *Joule* **2020**, *4*, 850.
[204] P. Tockhorn, J. Sutter, A. Cruz, P. Wagner, K. Jäger, D. Yoo, F. Lang, M. Grischek, B. Li, J. Li, O. Shargaieva, E. Unger, A. Al-Ashouri, E. Köhnen, M. Stolterfoht, D. Neher, R. Schlatmann, B. Rech, B. Stannowski, S. Albrecht, C. Becker, *Nat. Nanotechnol.* **2022**, *17*, 1214.
[205] K. D. G. I. Jayawardena, S. M. Silva, R. K. Misra, *J. Mater. Chem. C* **2020**, *8*, 10641.
[206] G. Zheng, C. Zhu, J. Ma, X. Zhang, G. Tang, R. Li, Y. Chen, L. Li, J. Hu, J. Hong, Q. Chen, X. Gao, H. Zhou, *Nat. Commun.* **2018**, *9*, 2793.
[207] D. H. Kim, J. Park, Z. Li, M. Yang, J.-S. Park, I. J. Park, J. Y. Kim, J. J. Berry, G. Rumbles, K. Zhu, *Adv. Mater.* **2017**, *29*, 1606831.
[208] L. A. Muscarella, E. M. Hutter, S. Sanchez, C. D. Dieleman, T. J. Savenije, A. Hagfeldt, M. Saliba, B. Ehrler, *J. Phys. Chem. Lett.* **2019**, *10*, 6010.
[209] Z. Ying, Z. Yang, J. Zheng, H. Wei, L. Chen, C. Xiao, J. Sun, C. Shou, G. Qin, J. Sheng, Y. Zeng, B. Yan, X. Yang, J. Ye, *Joule* **2022**, *6*, 2644.
[210] Y. Li, H. Sai, C. Mcdonald, Z. Xu, Y. Kurokawa, N. Usami, T. Matsui, *Adv. Mater. Interfaces* **2023**, *10*, 2300504.
[211] M. De Bastiani, R. Jalmood, J. Liu, C. Ossig, A. Vlk, K. Vegso, M. Babics, F. H. Isikgor, A. S. Selvin, R. Azmi, E. Ugur, S. Banerjee, A. J. Mirabelli, E. Aydin, T. G. Allen, A. Ur Rehman, E. Van Kerschaver, P. Siffalovic, M. E. Stuckelberger, M. Ledinsky, S. De Wolf, *Adv. Funct. Mater.* **2023**, *33*, 2205557.
[212] L. Mazzarella, Y.-H. Lin, S. Kirner, A. B. Morales-Vilches, L. Korte, S. Albrecht, E. Crossland, B. Stannowski, C. Case, H. J. Snaith, R. Schlatmann, *Adv. Energy Mater.* **2019**, *9*, 1803241.
[213] T. Han, W. Zhu, T. Wang, M. Yang, Y. Zhou, H. Xi, P. Zhong, D. Chen, J. Zhang, C. Zhang, Y. Hao, *Adv. Funct. Mater.* **2024**, *34*, 2311679.
[214] A. Singha, A. Paul, S. Koul, V. Sharma, S. Mallick, K. R. Balasubramaniam, D. Kabra, *Sol. RRL* **2023**, *7*, 2300117.
[215] H. Jung, G. Kim, G. S. Jang, J. Lim, M. Kim, C. S. Moon, X. Hao, N. J. Jeon, J. S. Yun, H. H. Park, J. Seo, *ACS Appl. Mater. Interfaces* **2021**, *13*, 30497.
[216] M. Chapa, M. F. Alexandre, M. J. Mendes, H. Águas, E. Fortunato, R. Martins, *ACS Appl. Energy Mater.* **2019**, *2*, 3979.
[217] X. Zhang, Q. Huang, J. Hu, R. J. Knize, Y. Lu, *Opt. Express* **2014**, *22*, A1400.
[218] J. Werner, B. Niesen, C. Ballif, *Adv. Mater. Interfaces* **2018**, *5*, 1700731.
[219] Longi Claims 33.9% Efficiency for Perovskite-Silicon Tandem Solar Cell. PV Magazine International, https://www.pv-magazine.com/2023/11/03/longi-claims-33-9-efficiency-for-perovskite-silicon-tandem-solar-cell/ (accessed: September 2024).
[220] C. U. Kim, E. D. Jung, Y. W. Noh, S. K. Seo, Y. Choi, H. Park, M. H. Song, K. J. Choi, *EcoMat* **2021**, *3*, e12084.
[221] L. Zhou, J. Rada, H. Zhang, H. Song, S. Mirniaharikandi, B. S. Ooi, Q. Gan, *Adv. Sci.* **2021**, *8*, 2102502.
[222] J. Mandal, Y. Fu, A. C. Overvig, M. Jia, K. Sun, N. N. Shi, H. Zhou, X. Xiao, N. Yu, Y. Yang, *Science* **2018**, *362*, 315.
[223] J. Mandal, M. Jia, A. Overvig, Y. Fu, E. Che, N. Yu, Y. Yang, *Joule* **2019**, *3*, 3088.
[224] X. Wang, X. Liu, Z. Li, H. Zhang, Z. Yang, H. Zhou, T. Fan, *Adv. Funct. Mater.* **2020**, *30*, 1907562.
[225] T. Wang, Y. Wu, L. Shi, X. Hu, M. Chen, L. Wu, *Nat. Commun.* **2021**, *12*, 365.
[226] Y. Zhai, Y. Ma, S. N. David, D. Zhao, R. Lou, G. Tan, R. Yang, X. Yin, *Science* **2017**, *355*, 1062.
[227] A. Kong, B. Cai, P. Shi, X. Yuan, *Opt. Express* **2019**, *27*, 30102.
[228] F. Bu, D. Yan, G. Tan, H. Sun, J. An, *Appl. Energy* **2022**, *312*, 118733.
[229] U. Banik, K. Sasaki, N. Reininghaus, K. Gehrke, M. Vehse, M. Sznajder, T. Sproewitz, C. Agert, *Sol. Energy Mater. Sol. Cells* **2020**, *209*, 110456.
[230] P. K. Tawalare, *AIP Adv.* **2021**, *11*.
[231] R. Lesyuk, V. Lesnyak, A. Herguth, D. Popovych, Y. Bobitski, C. Klinke, N. Gaponik, *J. Mater. Chem. C* **2017**, *5*, 11790.
[232] R. Lesyuk, V. Marinov, E. K. Hobbie, A. Elbaradei, I. Tarnavchyk, Y. Bobitski, *Sol. Energy Mater. Sol. Cells* **2016**, *151*, 52.

[233] A. J. Chatten, K. W. J. Barnham, B. F. Buxton, N. J. Ekins-Daukes, M. A. Malik, *Sol. Energy Mater. Sol. Cells* **2003**, *75*, 363.

[234] A. J. Chatten, K. W. J. Barnham, B. F. Buxton, N. J. Ekins-Daukes, M. A. Malik, *Semiconductors* **2004**, *38*, 909.

[235] B. Lipovšek, A. Solodovnyk, K. Forberich, E. Stern, J. Krč, C. J. Brabec, M. Topič, *Opt. Express* **2015**, *23*, A882.

[236] K. R. Mcintosh, G. Lau, J. N. Cotsell, K. Hanton, D. L. Bätzner, F. Bettiol, B. S. Richards, *Prog. Photovolt. Res. Appl.* **2009**, *17*, 191.

[237] J. W. E. Wiegman, E. Van Der Kolk, *Sol. Energy Mater. Sol. Cells* **2012**, *103*, 41.

[238] S. F. H. Correia, P. P. Lima, P. S. André, M. R. S. Ferreira, L. A. D. Carlos, *Sol. Energy Mater. Sol. Cells* **2015**, *138*, 51.

[239] S. F. H. Correia, P. P. Lima, E. Pecoraro, S. J. L. Ribeiro, P. S. André, R. A. S. Ferreira, L. D. Carlos, *Prog. Photovolt. Res. Appl.* **2016**, *24*, 1178.

[240] Y. H. Ghymn, K. Jung, M. Shin, H. Ko, *Nanoscale* **2015**, *7*, 18642.

[241] W. G. J. H. M. Van Sark, A. Meijerink, R. E. I. Schropp, J. A. M. Van Roosmalen, E. H. Lysen, *Sol. Energy Mater. Sol. Cells* **2005**, *87*, 395.

[242] B. C. Rowan, L. R. Wilson, B. S. Richards, *IEEE J. Sel. Top. Quantum Electron.* **2008**, *14*, 1312.

[243] G. I. Koleilat, L. Levina, H. Shukla, S. H. Myrskog, S. Hinds, A. G. Pattantyus-Abraham, E. H. Sargent, *ACS Nano* **2008**, *2*, 833.

[244] S.-H. Cho, Y.-J. Shin, S.-M. Jeong, S.-H. Kwon, S.-Y. Bae, *Jpn. J. Appl. Phys.* **2023**, *62*.

[245] S. F. H. Correia, V. D. Zea Bermudez, S. J. L. Ribeiro, P. S. André, R. A. S. Ferreira, L. D. Carlos, *J. Mater. Chem. A* **2014**, *2*, 5580.

[246] A. Pinheiro, A. Ruivo, J. Rocha, M. Ferro, J. V. Pinto, J. Deuermeier, T. Mateus, A. Santa, M. J. Mendes, R. Martins, S. Gago, C. A. T. Laia, H. Águas, *Nanomaterials* **2023**, *13*, 210.

[247] A. Menéndez-Velázquez, S. Torres-García, A. B. García-Delgado, D. Morales, M. Medina-Alayón, P. Acosta-Mora, J. del-Castillo, P. Esparza, M. E. Borges, A. C. Yanes, J. Méndez-Ramos, *Opt. Mater.* **2023**, *142*, https://doi.org/10.1016/j.optmat.2023.114005.

[248] J. Qi, H. Xiong, G. Wang, H. Xie, W. Jia, Q. Zhang, Y. Li, H. Wang, *J. Power Sources* **2018**, *376*, 46.

[249] Y.-K. Liao, M. Brossard, D.-H. Hsieh, T.-N. Lin, M. D. B. Charlton, S.-J. Cheng, C.-H. Chen, J.-L. Shen, L.-T. Cheng, T.-P. Hsieh, F.-I. Lai, S.-Y. Kuo, H.-C. Kuo, P. G. Savvidis, P. G. Lagoudakis, *Adv. Energy Mater.* **2015**, *5*, 1401280.

[250] S. D. Hodgson, W. S. M. Brooks, A. J. Clayton, G. Kartopu, V. Barrioz, S. J. C. Irvine, *Nano Energy* **2014**, *4*, 1.

[251] H.-V. Han, C.-C. Lin, Y.-L. Tsai, H.-C. Chen, K.-J. Chen, Y.-L. Yeh, W.-Y. Lin, H.-C. Kuo, P. Yu, *Sci. Rep.* **2014**, *4*.

[252] L. Meng, X.-G. Wu, S. Ma, L. Shi, M. Zhang, L. Wang, Y. Chen, Q. Chen, H. Zhong, *Nanophotonics* **2020**, *9*, 93.

[253] A. Z. Kainarbay, T. N. Nurakhmetov, D. K. Daurenbekov, A. A. Eliseev, T. Y. Sachkova, Z. M. Salikhodzha, A. M. Zhunusbekov, *Optik* **2018**, *169*, 41.

[254] L. Meng, L. Shi, Y. Ge, J. Tang, Y. Chen, H. Zhong, *Sol. Energy Mater. Sol. Cells* **2021**, *220*, 110856.

[255] A. S. Sadhu, Y.-M. Huang, L.-Y. Chen, H.-C. Kuo, C.-C. Lin, *Nanomaterials* **2022**, *12*.

[256] Y. Zhou, J. Yang, X. Luo, Y. Li, Q. Qiu, T. Xie, *Int. J. Mol. Sci.* **2022**, *23*, https://doi.org/10.3390/ijms23169482.

[257] L. Francés-Soriano, E. Zaballos-García, J. Pérez-Prieto, *Adv. Opt. Mater.*, 2300337.

[258] N. K. Kalluvettukuzhy, M. R. Maciejczyk, I. Underwood, N. Robertson, *J. Mater. Chem. A* **2023**, *11*, 13195.

[259] M. Alexandre, M. Chapa, S. Haque, M. J. Mendes, H. Águas, E. Fortunato, R. Martins, *ACS Appl. Energy Mater.* **2019**, *2*, 2930.

[260] H.-C. Chen, C.-C. Lin, H.-W. Han, Y.-L. Tsai, C.-H. Chang, H.-W. Wang, M.-A. Tsai, H.-C. Kuo, P. Yu, *Opt. Express* **2011**, *19*, A1141.

[261] F. Xu, Y. Sun, H. Gao, S. Jin, Z. Zhang, H. Zhang, G. Pan, M. Kang, X. Ma, Y. Mao, *ACS Appl. Mater. Interfaces* **2021**, *13*, 2674.

[262] L. Liang, M. Liu, Z. Jin, Q. Wang, H. Wang, H. Bian, F. Shi, S. Liu, *Nano Lett.* **2019**, *19*, 1796.

[263] W. Sheng, J. Yang, X. Li, G. Liu, Z. Lin, J. Long, S. Xiao, L. Tan, Y. Chen, *Energy Environ. Sci.* **2021**, *14*, 3532.

[264] W. Bi, Y. Wu, C. Chen, D. Zhou, Z. Song, D. Li, G. Chen, Q. Dai, Y. Zhu, H. Song, *ACS Appl. Mater. Interfaces* **2020**, *12*, 24737.

[265] X. Wang, Z. Zhang, J. Qin, W. Shi, Y. Liu, H. Gao, Y. Mao, *Electrochim. Acta* **2017**, *245*, 839.

[266] H. Li, C. Chen, J. Jin, W. Bi, B. Zhang, X. Chen, L. Xu, D. Liu, Q. Dai, H. Song, *Nano Energy* **2018**, *50*, 699.

[267] X. Chen, W. Xu, H. Song, C. Chen, H. Xia, Y. Zhu, D. Zhou, S. Cui, Q. Dai, J. Zhang, *ACS Appl. Mater. Interfaces* **2016**, *8*, 9071.

[268] K. Nehra, A. Dalal, A. Hooda, S. Bhagwan, R. K. Saini, B. Mari, S. Kumar, D. Singh, *J. Mol. Struct.* **2022**, *1249*, 131531.

[269] Y. Chen, W. Zheng, S. Murcia-López, F. Lv, J. R. Morante, L. Vayssieres, C. Burda, *J. Mater. Chem. C* **2021**, *9*, 3726.

[270] A. Gupta, S. Ghosh, M. K. Thakur, J. Zhou, K. (Ken) Ostrikov, D. Jin, S. Chattopadhyay, *Prog. Mater. Sci.* **2021**, *121*, 100838.

[271] A. Ghazy, M. Safdar, M. Lastusaari, H. Savin, M. Karppinen, *Sol. Energy Mater. Sol. Cells* **2021**, *230*, 111234.

[272] J. Sun, X. Yang, S. Sun, L. Zhao, S. Wang, Y. Li, *Inorg. Chem. Commun.* **2022**, *143*, 109731.

[273] B. Liu, Y. Wang, Y. Wu, B. Dong, H. Song, *J. Mater. Sci. Technol.* **2023**, *140*, 33.

[274] N. Shah, A. A. Shah, P. K. Leung, S. Khan, K. Sun, X. Zhu, Q. Liao, *Processes* **2023**, *11*, 1852.

[275] H.-J. Yin, Z.-G. Xiao, Y. Feng, C.-J. Yao, *Materials* **2023**, *16*.

[276] L. Yuliantini, N. M. Nursam, L. M. Pranoto, L. M. Shobih, J. Hidayat, R. R. Sova, R. R. Isnaeni, E. S. Rahayu, M. Djamal, P. Yasaka, K. Boonin, J. Kaewkhao, *J. Alloys Compd.* **2023**, *954*, 170163.

[277] R. M. Gunji, E. V. A. Santos, C. D. S. Bordon, J. A. M. Garcia, L. A. Gómez-Malagón, L. R. P. Kassab, *J. Lumin.* **2020**, *226*, 117497.

[278] R. Rondão, A. R. Frias, S. F. H. Correia, L. Fu, V. De Zea Bermudez, P. S. André, R. A. S. Ferreira, L. D. Carlos, *ACS Appl. Mater. Interfaces* **2017**, *9*, 12540.

[279] H. K. Sung, Y. K. Lee, W. H. Kim, S.-J. Lee, S.-J. Sung, D.-J. Kim, Y. S. Han, *Molecules* **2020**, *25*, 1502.

[280] Z. Cheng, F. Su, L. Pan, M. Cao, Z. Sun, *J. Alloys Compd.* **2010**, *494*, L7.

[281] T.-T. Xuan, J.-Q. Liu, H.-L. Li, H.-C. Sun, L.-K. Pan, X.-H. Chen, Z. Sun, *RSC Adv.* **2015**, *5*, 7673.

[282] H. Ahmed, J. Doran, S. J. Mccormack, *Sol. Energy* **2016**, *126*, 146.

[283] Y.-Y. Cho, C.-C. Lin, Y.-M. Huang, S.-C. Hsu, S.-F. Kao, H.-Y. Shih, T.-Y. Lee, Y.-H. Liu, T.-M. Chen, C.-H. Kuo, in *2019 IEEE 46th Photovoltaic Specialists Conf. (PVSC)*, IEEE, Piscataway, NJ **2019**, pp. 2600–2602.

[284] Y.-M. Huang, C.-P. Huang, T.-Y. Lee, Y.-H. Liu, Y.-M. Chen, H.-C. Kuo, C.-C. Lin, in *2020 47th IEEE Photovoltaic Specialists Conf. (PVSC)*, IEEE, Piscataway, NJ **2020**, pp. 0881–0883.

[285] S. D. Hodgson, W. S. M. Brooks, A. J. Clayton, G. Kartopu, D. A. Lamb, V. Barrioz, S. J. C. Irvine, *Prog. Photovolt. Res. Appl.* **2015**, *23*, 150.

[286] C.-J. Shu, Y.-M. Huang, S.-C. Hsu, J.-K. Shu, J.-L. Tsai, P.-C. Yu, Y.-J. Hung, C.-C. Lin, in *2017 IEEE 44th Photovoltaic Specialist Conf. (PVSC)*, IEEE, Washington, DC **2017**, pp. 1606–1609.

[287] C.-H. Chen, C.-P. Yu, Y.-M. Huang, Y.-L. Chan, C.-P. Huang, S.-H. Chang, S.-C. Hsu, J.-J. Liou, T.-M. Chen, C.-C. Lin in *2018 IEEE 7th World Conf. on Photovoltaic Energy Conversion (WCPEC) (A Joint Conf. of 45th IEEE PVSC, 28th PVSEC & 34th EU PVSEC)*, IEEE, Piscataway, NJ **2018**, pp. 2865–2867.

[288] H.-J. Jeong, Y.-C. Kim, S. K. Lee, Y. Jeong, J.-W. Song, J.-H. Yun, J.-H. Jang, *ACS Appl. Mater. Interfaces* **2017**, *9*, 25404.
[289] M. I. Asghar, J. Zhang, H. Wang, P. D. Lund, *Renew. Sustain. Energy Rev.* **2017**, *77*, 131.
[290] T. Leijtens, G. E. Eperon, S. Pathak, A. Abate, M. M. Lee, H. J. Snaith, *Nat. Commun.* **2013**, *4*, 2885.
[291] S. Ito, S. Tanaka, K. Manabe, H. Nishino, *J. Phys. Chem. C* **2014**, *118*, 16995.
[292] S. Gardelis, A. G. Nassiopoulou, *Appl. Phys. Lett.* **2014**, *104*, 183902.
[293] M. Ambapuram, M. Mounika Parnapalli, G. Maddala, S. Kalvapalli, S. Pola, R. Mitty, *ChemPhotoChem* **2023**, *7*.
[294] A. Danel, S. Harrison, F. Gérenton, A. Moustafa, R. Varache, J. Veirman, C. Roux, in *35th Eur. Photovolt. Sol. Energy Conf. Exhib.* **2018**, p. 444, https://doi.org/10.4229/35THEUPVSEC20182018-2DO.1.2.
[295] A. W. Blakers, K. J. Weber, M. F. Stuckings, S. Armand, G. Matlakowski, A. J. Carr, M. J. Stocks, A. Cuevas, T. Brammer, *Prog. Photovolt. Res. Appl.* **1995**, *3*, 193.
[296] A. Wolf, B. Terheiden, R. Brendel, *Prog. Photovolt. Res. Appl.* **2007**, *15*, 199.
[297] M. Ali Shameli, L. Yousefi, *Opt. Laser Technol.* **2022**, *145*.
[298] S. M. Almenabawy, R. Prinja, N. P. Kherani, *Sol. Energy* **2023**, *256*, 88.
[299] S. M. Almenabawy, Y. Zhang, R. Prinja, G. Sharma, N. P. Kherani, in *2020 IEEE 47th Photovoltaic Specialists Conf. (PVSC)*, IEEE, Piscataway, NJ **2020**, pp. 2304–2307.
[300] C. Trompoukis, O. El Daif, V. Depauw, I. Gordon, J. Poortmans, *Appl. Phys. Lett.* **2012**, *101*, 103901.
[301] C. W. Teplin, S. Grover, A. Chitu, A. Limanov, M. Chahal, J. Im, D. Amkreutz, S. Gall, H. P. Yoon, V. Lasalvia, P. Stradins, K. M. Jones, A. G. Norman, D. L. Young, H. M. Branz, B. G. Lee, *Prog. Photovolt. Res. Appl.* **2015**, *23*, 909.
[302] M. A. Elrabiaey, M. Hussein, M. F. O. Hameed, S. S. A. Obayya, *Sci. Rep.* **2020**, *10*.
[303] F. Haase, R. Horbelt, B. Terheiden, H. Plagwitz, R. Brendel, in *2009 34th IEEE Photovoltaic Specialists Conf. (PVSC)*, IEEE, Piscataway, NJ **2009**, pp. 000244–000246.
[304] G. F. Zheng, W. Zhang, Z. Shi, M. Gross, A. B. Sproul, S. R. Wenham, M. A. Green, *Sol. Energy Mater. Sol. Cells* **1996**, *40*, 231.
[305] G. F. Zheng, S. R. Wenham, M. A. Green, *Prog. Photovolt. Res. Appl.* **1996**, *4*, 369.
[306] Z. Gao, G. Lin, Y. Chen, Y. Zheng, N. Sang, Y. Li, L. Chen, M. Li, *Sol. Energy* **2020**, *205*, 275.
[307] H. J. Kim, V. Depauw, F. Duerinckx, G. Beaucarne, J. Poortmans, in *IEEE 4th World Conf. on Photovoltaic Energy Conf.*, Vol. *1*, IEEE, Piscataway, NJ **2006**, pp. 984–987.
[308] H. M. Branz, C. W. Teplin, M. J. Romero, I. T. Martin, Q. Wang, K. Alberi, D. L. Young, P. Stradins, *Thin Solid Films* **2011**, *519*, 4545.
[309] H.-S. Lee, J. Suk, H. Kim, J. Kim, J. Song, D. S. Jeong, J.-K. Park, W. M. Kim, D.-K. Lee, K. J. Choi, B.-K. Ju, T. S. Lee, I. Kim, *Sci. Rep.* **2018**, *8*, 3504.
[310] H. Sivaramakrishnan Radhakrishnan, M. Xu, T. Bearda, M. Filipic, K. Van Nieuwenhuysen, V. Depauw, I. Gordon, M. Debucquoy, J. Szlufcik, J. Poortmans, *33rd Eur. Photovolt. Sol. Energy Conf. Exhib.* **2017**, p. 740, https://doi.org/10.4229/EUPVSEC20172017-2AV.3.14.
[311] H. Sai, T. Oku, Y. Sato, M. Tanabe, T. Matsui, K. Matsubara, *Prog. Photovolt. Res. Appl.* **2019**, *27*, 1061.
[312] I. Hwang, Y. Jeong, Y. Shiratori, J. Park, S. Miyajima, I. Yoon, K. Seo, *Cell Rep. Phys. Sci.* **2020**, *1*.
[313] I. Kim, D. S. Jeong, W. S. Lee, W. M. Kim, T.-S. Lee, D.-K. Lee, J.-H. Song, J.-K. Kim, K.-S. Lee, *Opt. Express* **2014**, *22*, A1431.
[314] I. Kuzma-Filipek, F. Dross, K. Baert, J. L. Hernandez, S. Singh, K. Van Nieuwenhuysen, J. Poortmans, *Prog. Photovolt. Res. Appl.* **2012**, *20*, 350.
[315] J. H. Petermann, D. Zielke, J. Schmidt, F. Haase, E. G. Rojas, R. Brendel, *Prog. Photovolt. Res. Appl.* **2012**, *20*, 1.
[316] J. He, M. A. Hossain, H. Lin, W. Wang, S. K. Karuturi, B. Hoex, J. Ye, P. Gao, J. Bullock, Y. Wan, *ACS Nano* **2019**, *13*, 6356.
[317] K. S. Do, T.-H. Baek, M. G. Kang, S. J. Choi, G. H. Kang, G. J. Yu, J. C. Lee, J.-M. Myoung, H.-E. Song, *Met. Mater. Int.* **2014**, *20*, 545.
[318] K. Van Nieuwenhuysen, M. R. Payo, I. Kuzma-Filipek, J. Van Hoeymissen, G. Beaucarne, J. Poortmans, *Thin Solid Films* **2010**, *518*, S80.
[319] K. X. Wang, Z. Yu, V. Liu, Y. Cui, S. Fan, *Nano Lett.* **2012**, *12*, 1616.
[320] L. Wang, A. Lochtefeld, J. Han, A. P. Gerger, M. Carroll, J. Ji, A. Lennon, H. Li, R. Opila, A. Barnett, *IEEE J. Photovolt.* **2014**, *4*, 1397.
[321] L. Zeng, P. Bermel, Y. Yi, B. A. Alamariu, K. A. Broderick, J. Liu, C. Hong, X. Duan, J. Joannopoulos, L. C. Kimerling, *Appl. Phys. Lett.* **2008**, *93*, 221105.
[322] N. Lee, M. Xue, J. Hong, J. van de Groep, M. L. Brongersma, *Adv. Mater.* **2023**, *35*.
[323] C. M. Lee, S. H. U. Shah, K.-J. Ko, D. H. Kim, T. W. Kim, H. W. Cho, Y. B. Kim, J. W. Lee, K. Heo, C. H. Kim, H. J. Lee, G. Lee, S. Roh, S. Park, S. G. Lee, T.-S. Bae, S. M. Yu, J. S. Jin, H. Moon, A. Islam, P. J. Jesuraj, M. Song, C.-S. Kim, S. Y. Ryu, *Sol. RRL* **2023**, *7*.
[324] N. Lu, Q. Lei, X. Xu, L. Yang, Z. Yang, Z. Liu, Y. Zeng, J. Ye, S. He, *Opt. Express* **2022**, *30*, 21309.
[325] M. Reuter, W. Brendle, O. Tobail, J. H. Werner, *Sol. Energy Mater. Sol. Cells* **2009**, *93*, 704.
[326] M. S. Branham, W.-C. Hsu, S. Yerci, J. Loomis, S. V. Boriskina, B. R. Hoard, S. E. Han, G. Chen, *Adv. Mater.* **2015**, *27*, 2182.
[327] M. Taguchi, A. Yano, S. Tohoda, K. Matsuyama, Y. Nakamura, T. Nishiwaki, K. Fujita, E. Maruyama, *IEEE J. Photovolt.* **2014**, *4*, 96.
[328] M. Xue, R. Islam, A. C. Meng, Z. Lyu, C.-Y. Lu, C. Tae, M. R. Braun, K. Zang, P. C. Mcintyre, T. I. Kamins, K. C. Saraswat, J. S. Harris, *ACS Appl. Mater. Interfaces* **2017**, *9*, 41863.
[329] I. Martín, G. López, M. Garin, P. Ortega, C. Voz, G. Jia, A. Gawlik, J. Plentz, *IEEE J. Photovolt.* **2021**, *11*, 1358.
[330] P. Kapur, M. Moslehi, A. Deshpande, V. Rana, J. Kramer, S. Seutter, H. Deshazer, S. Coutant, A. Calcaterra, S. Kommera, Y.-S. Su, D. Grupp, S. Tamilmani, D. Dutton, T. Stalcup, T. Du, T. Wingert, in *28th Eur. Photovolt. Sol. Energy Conf. Exhib.* **2013**, pp. 2228–2231, https://doi.org/10.4229/28THEUPVSEC2013-3DO.7.6.
[331] P. Kuang, S. Eyderman, M.-L. Hsieh, A. Post, S. John, S.-Y. Lin, *ACS Nano* **2016**, *10*, 6116.
[332] M. Z. Pakhuruddin, *AIP Conf. Proc.* **2020**.
[333] Q. Tang, H. Shen, H. Yao, K. Gao, Y. Jiang, Y. Li, Y. Liu, L. Zhang, Z. Ni, Q. Wei, *Renew. Energy* **2019**, *133*, 883.
[334] R. B. Bergmann, C. Berge, T. J. Rinke, J. Schmidt, J. H. Werner, *Sol. Energy Mater. Sol. Cells* **2002**, *74*, 213.
[335] R. Cariou, W. Chen, I. Cosme-Bolanos, J.-L. Maurice, M. Foldyna, V. Depauw, G. Patriarche, A. Gaucher, A. Cattoni, I. Massiot, S. Collin, E. Cadel, P. Pareige, P. Roca I Cabarrocas, *Prog. Photovolt. Res. Appl.* **2016**, *24*, 1075.
[336] R. Cariou, R. Ruggeri, P. Chatterjee, J.-L. Gentner, P. R. Cabarrocas, in *Thin Film Solar Technology IV*, Vol. *8470*, SPIE, Bellingham, WA **2012**, pp. 28–36.
[337] S. B. Mallick, M. Agrawal, P. Peumans, *Opt. Express* **2010**, *18*, 5691.
[338] S. Saha, M. M. Hilali, E. U. Onyegam, D. Sarkar, D. Jawarani, R. A. Rao, L. Mathew, R. S. Smith, D. Xu, U. K. Das, B. Sopori, S. K. Banerjee, *Appl. Phys. Lett.* **2013**, *102*, 163904.

[339] S. Wang, B. D. Weil, Y. Li, K. X. Wang, E. Garnett, S. Fan, Y. Cui, *Nano Lett.* **2013**, *13*, 4393.
[340] S. W. Glunz, *Sol. Energy Mater. Sol. Cells* **2006**, *90*, 3276.
[341] T. K. Chong, J. Wilson, S. Mokkapati, K. R. Catchpole, *J. Opt.* **2012**, *14*, 024012.
[342] N. Tavakoli, R. Spalding, A. Lambertz, P. Koppejan, G. Gkantzounis, C. Wan, R. Röhrich, E. Kontoleta, A. F. Koenderink, R. Sapienza, M. Florescu, E. Alarcon-Llado, *ACS Photonics* **2022**, *9*, 1206.
[343] W. Hadibrata, F. Es, S. Yerci, R. Turan, *Sol. Energy Mater. Sol. Cells* **2018**, *180*, 247.
[344] W.-C. Hsu, J. K. Tong, M. S. Branham, Y. Huang, S. Yerci, S. V. Boriskina, G. Chen, *Opt. Commun.* **2016**, *377*, 52.
[345] C. Wang, B. Ding, F. Bian, Y. Yang, S. M. Zaheer, T. Yu, Z. Li, H. Wang, Z. Xu, *Opt. Mater.* **2022**, *123*, https://doi.org/10.1016/j.optmat.2021.111943.
[346] X. Meng, E. Drouard, G. Gomard, R. Peretti, A. Fave, C. Seassal, *Opt. Express* **2012**, *20*, A560.
[347] Y. Li, S. Zhong, Y. Zhuang, L. Yang, F. Meng, W. Wang, Z. Li, W. Shen, *Adv. Electron. Mater.* **2019**, *5*, 1800858.
[348] Y. Shi, X. Wang, W. Liu, T. Yang, F. Yang, *Phys. Status Solidi A* **2015**, *212*, 312.
[349] H. Zheng, Y. Yu, R. Wu, S. Wu, S. Chen, K. Chen, *Appl. Opt.* **2020**, *59*, 10330.
[350] J. Feng, X. Wang, J. Li, H. Liang, W. Liang, E. Alvianto, C.-W. Qiu, R. Su, Y. Hou, *Nat. Commun.* **2023**, *14*, https://doi.org/10.1038/s41467-023-41149-1.
[351] I. Ullah, J. Guo, C. Wang, Z. Liu, X. Li, L. Jiang, J. Yuan, W. Ma, *J. Alloys Compd.* **2023**, *960*, https://doi.org/10.1016/j.jallcom.2023.170994.
[352] H. Liang, Z. Wen, F. Wang, Z. Cheng, *Energy Rep.* **2023**, *9*, 190.
[353] A. A. Zaky, S. Elewa, S. Alyahya, M. Al-Dhaifallah, H. Rezk, B. Yousif, *IEEE Access* **2023**, *11*, 36399.
[354] W. Wang, G. Yu, S. Attique, *Adv. Theory Simul.* **2023**, https://doi.org/10.1002/adts.202300135.
[355] Y. Zhu, L. Shu, S. Poddar, Q. Zhang, Z. Chen, Y. Ding, Z. Long, S. Ma, B. Ren, X. Qiu, Z. Fan, *Nano Lett.* **2022**, *22*, 9586.
[356] M. Batmunkh, T. J. Macdonald, W. J. Peveler, A. S. R. Bati, C. J. Carmalt, I. P. Parkin, J. G. Shapter, *ChemSusChem* **2017**, *10*, 3750.
[357] H. Kim, H. Kwak, I. Jung, M. S. Kim, J. Kim, H. J. Park, K.-T. Lee, *Opt. Express* **2021**, *29*, 35366.
[358] H. Zhang, M. Kramarenko, J. Osmond, J. Toudert, J. Martorell, *ACS Photonics* **2018**, *5*, 2243.
[359] M. I. Hossain, N. Yumnam, W. Qarony, A. Salleo, V. Wagner, D. Knipp, Y. H. Tsang, *Sol. Energy* **2020**, *198*, 570.
[360] P. Tockhorn, J. Sutter, R. Colom, L. Kegelmann, A. Al-Ashouri, M. Roß, K. Jäger, T. Unold, S. Burger, S. Albrecht, C. Becker, *ACS Photonics* **2020**, *7*, 2589.
[361] Y. Wang, Y. Lan, Q. Song, F. Vogelbacher, T. Xu, Y. Zhan, M. Li, W. E. I. Sha, Y. Song, *Adv. Mater.* **2021**, *33*, https://doi.org/10.1002/adma.202008091.
[362] M. I. Hossain, M. Shahiduzzaman, S. Ahmed, M. R. Huqe, W. Qarony, A. M. Saleque, M. Akhtaruzzaman, D. Knipp, Y. H. Tsang, T. Taima, J. A. Zapien, *Nano Energy* **2021**, *89*.
[363] M. H. Mohammadi, D. Fathi, M. Eskandari, *Energy Rep.* **2021**, *7*, 1404.
[364] A. Furasova, P. Voroshilov, M. Baranov, P. Tonkaev, A. Nikolaeva, K. Voronin, L. Vesce, S. Makarov, A. Di Carlo, *Nano Energy* **2021**, *89*.
[365] A. Maho, M. Lobet, N. Daem, P. Piron, G. Spronck, J. Loicq, R. Cloots, P. Colson, C. Henrist, J. Dewalque, *ACS Appl. Energy Mater.* **2021**, *4*, 1108.
[366] C. Cho, Y.-W. Jang, S. Lee, Y. Vaynzof, M. Choi, J. H. Noh, K. Leo, *Sci. Adv.* **2021**, *7*, eabj1363.
[367] K. Yao, H. Zhong, Z. Liu, M. Xiong, S. Leng, J. Zhang, Y.-X. Xu, W. Wang, L. Zhou, H. Huang, A. K.-Y. Jen, *ACS Nano* **2019**, *13*, 52 5397.
[368] K. Deng, Z. Liu, M. Wang, L. Li, *Adv. Funct. Mater.* **2019**, *29*.
[369] J. Huang, S. Xiang, J. Yu, C.-Z. Li, *Energy Environ. Sci.* **2019**, *12*, 929.
[370] R. Schmager, G. Gomard, B. S. Richards, U. W. Paetzold, *Sol. Energy Mater. Sol. Cells* **2019**, *192*, 65.
[371] K. Li, S. Zhang, Y. Ruan, D. Li, T. Zhang, H. Zhen, *Opt. Express* **2019**, *27*, A1004.
[372] Y. Wang, M. Li, X. Zhou, P. Li, X. Hu, Y. Song, *Nano Energy* **2018**, *51*, 556.
[373] D. Liu, L. Wang, Q. Cui, L. J. Guo, *Adv. Sci.* **2018**, *5*.
[374] Y. Nakamura, Y. Iso, T. Isobe, *ACS Appl. Nano Mater.* **2020**, *3*, 3417.
[375] C.-C. Lin, H.-C. Chen, Y. L. Tsai, H.-V. Han, H.-S. Shih, Y.-A. Chang, H.-C. Kuo, P. Yu, *Opt. Express* **2012**, *20*, A319.
[376] M. Rwaimi, C. G. Bailey, P. J. Shaw, T. M. Mercier, C. Krishnan, T. Rahman, P. G. Lagoudakis, R.-H. Horng, S. A. Boden, M. D. B. Charlton, *Sol. Energy Mater. Sol. Cells* **2022**, *234*, 111406.
[377] Y. Li, H. Lin, J. Zeng, J. Chen, H. Chen, *Sol. Energy* **2019**, *193*, 303.
[378] Y.-C. Kim, H.-J. Jeong, S.-T. Kim, Y. H. Song, B. Y. Kim, J. P. Kim, B. K. Kang, J.-H. Yun, J.-H. Jang, *Nanoscale* **2020**, *12*, 558.
[379] B. Wang, B. Li, T. Shen, M. Li, J. Tian, *J. Energy Chem.* **2018**, *27*, 736.
[380] Q. Wang, X. Zhang, Z. Jin, J. Zhang, Z. Gao, Y. Li, S. F. Liu, *ACS Energy Lett.* **2017**, *2*, 1479.
[381] F. Gao, H. Dai, H. Pan, Y. Chen, J. Wang, Z. Chen, *J. Colloid Interface Sci.* **2018**, *513*, 693.
[382] C. Chen, Y. Wu, L. Liu, Y. Gao, X. Chen, W. Bi, X. Chen, D. Liu, Q. Dai, H. Song, *Adv. Sci.* **2019**, *6*, 1802046.
[383] R. S. Davidsen, H. Li, A. To, X. Wang, A. Han, J. An, J. Colwell, C. Chan, A. Wenham, M. S. Schmidt, A. Boisen, O. Hansen, S. Wenham, A. Barnett, *Sol. Energy Mater. Sol. Cells* **2016**, *144*, 740.
[384] B. Radfar, F. Es, R. Turan, *Renew. Energy* **2000**, *145*, 2707.
[385] F. Wang, Y. Zhang, M. Yang, Y. Sui, Y. Sun, L. Yang, J. Yang, X. Zhang, *J. Alloys Compd.* **2018**, *752*, 53.
[386] C. Zhang, L. Chen, Y. Zhu, Z. Guan, *Nanoscale Res. Lett.* **2018**, *13*, 91.
[387] B. Radfar, F. Es, R. Turan, *Renew. Energy* **2020**, *145*, 2707.
[388] J. Zhou, Y. Tan, W. Liu, X. Cai, H. Huang, Y. Cao, *SN Appl. Sci.* **2020**, *2*, 799.
[389] K. P. Sreejith, A. K. Sharma, P. K. Basu, A. Kottantharayil, *Sol. Energy* **2021**, *230*, 874.
[390] D. Zhang, S. Jiang, K. Tao, R. Jia, H. Ge, X. Li, B. Wang, M. Li, Z. Ji, Z. Gao, Z. Jin, *Sol. Energy Mater. Sol. Cells* **2021**, *230*, 111200.
[391] D. Zhang, J. Chen, R. Jia, Z. Gao, K. Tao, L. Wang, H. Ge, X. Li, X. Li, *J. Energy Chem.* **2022**, *71*, 104.
[392] W. Chen, Y. Yu, W. Wang, P. Chen, Y. Ke, W. Liu, Y. Wan, *Sol. Energy* **2022**, *247*, 24.
[393] V. V. Kuruganti, O. Isabella, V. D. Mihailetchi, *Phys. Status Solidi A* **2024**, 2300820, https://doi.org/10.1002/pssa.202300820.
[394] I. Y. Choi, C. U. Kim, W. Park, H. Lee, M. H. Song, K. K. Hong, S. I. Seok, K. J. Choi, *Nano Energy* **2019**, *65*, 104044.
[395] G. Nogay, F. Sahli, J. Werner, R. Monnard, M. Boccard, M. Despeisse, F.-J. Haug, Q. Jeangros, A. Ingenito, C. Ballif, *ACS Energy Lett.* **2019**, *4*, 844.
[396] F. Hou, C. Han, O. Isabella, L. Yan, B. Shi, J. Chen, S. An, Z. Zhou, W. Huang, H. Ren, Q. Huang, G. Hou, X. Chen, Y. Li, Y. Ding, G. Wang, C. Wei, D. Zhang, M. Zeman, Y. Zhao, X. Zhang, *Nano Energy* **2019**, *56*, 234.

Ivan M. Santos is a Ph.D. student in the nanoscience and nanotechnology program in the Materials Science Department and holds an M.Sc. degree in materials engineering from Nova School of Science and Technology (2022). Ivan Santos was recognized as the top-ranked candidate in the micro and nanoengineering panel for Ph.D. scholarships (2023), received the first honorable mention from the Portuguese Order of Engineers (OE), and graduated as the best student of his class with a perfect thesis score. He was involved in several national and international research projects, and his research focuses on the fabrication and modeling of wave-optical light-trapping structures for photovoltaic systems.

Miguel Alexandre holds an M.Sc. degree (2018) in micro- and nanotechnology Engineering and a Ph.D. in quantum and optical simulation of semiconductors from Nova School of Science and Technology, Lisbon, Portugal. With key contributions to National and European research projects related to quantum-structured semiconductors, photonic-enhanced solar cells, building-integrated photovoltaics (BIPV), and solar fuels, he currently leads the modeling work packages of the ERC-funded project X-Stream and the European project JUMP INTO SPACE. With a portfolio of >15 peer-reviewed publications with >270 citations, his research interests include photonics and density functional theory for photovoltaics, leveraging advanced coding and computing.

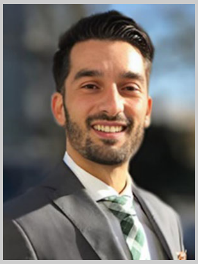

António T. Vicente is an assistant researcher specializing in sustainable materials and advanced fabrication for solar energy, coleading several national and international projects. He earned his B.Sc. and M.Sc. in biomedical engineering from NOVA University and a Ph.D. through the MIT-Portugal program, where he pioneered silicon thin-film solar cells on paper substrates. At CENIMAT i3N, he advanced optically variable inks and computational optimization using DoE, MVA, and simulations for security and solar energy applications. With over 10 years of research experience, António Vicente emphasizes sustainability in R&D, bridging novel materials and devices for green energy through multidisciplinary and translational approaches.

Cristina Teixeira holds a Ph.D. in chemical engineering from the Faculty of Engineering, University of Porto (FEUP). She completed her M.Sc. thesis and began her doctoral studies at LEPABE (FEUP), continuing her research at SAULE Technologies, a Polish company pioneering the market deployment of perovskite solar technology. Her work focuses on developing industrially viable perovskite solar cells (PSCs) and modules, promoting their scalability. Her expertise includes carbon-based electrodes, efficient, and stable PSCs for indoor and terrestrial applications and scalable, low-cost coating methods. She coinvented one patent, developed three trade secrets, published five first-author articles, and presented at 12 international congresses.

Eva Almeida is a Ph.D. student at the University of Amsterdam, specializing in 2D nanophotonics. She holds an M.Sc. in engineering in micro- and nanotechnologies from NOVA University of Lisbon (2023), where she worked on photonic-enhanced perovskite solar cells. Prior to her Ph.D., she was a research fellow at CENIMAT|i3N (2024), where she studied perovskite-on-silicon tandem solar cells. Her expertise includes computational simulation, device optimization, and photonic engineering for optoelectronics. Her current research focuses on developing high-efficiency metasurfaces for building-integrated photovoltaics (BIPV), designing nanophotonic structures that optimize both light capture and visual aesthetics.

Elvira Fortunato is a full professor at FCT-NOVA, former minister of Science (2022–2024), Technology, and Higher Education of Portugal and former Vice-Rector of NOVA University of Lisbon (2022). Elvira was elected as one of the 27 inspiring European Women and as a member of the European Science Academy. Elvira Fortunato is among the 20 hidden Inventors of Europe, given her work on transparent electronics and paper electronics. Her list of prizes and distinctions includes the Advanced Material Frontier Award (2022), Human Rights Award by the Portuguese Parliament (2021), PESSOA Prize (2021), and Horizon Impact Award (2020), among others.

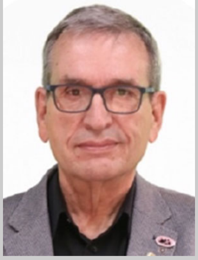

Rodrigo Martins is a full professor at FCT-NOVA with more than 1,350 peer-reviewed publications, over 40,600 citations, and an H-index of 100. He is the president of the European Academy of Sciences, director of the Materials Research Center (CENIMAT) and the Associated Laboratory i3N (Institute of Nanostructures, Nanomodeling, and Nanofabrication), and coordinator of the Emerging Printed Electronics Research Infrastructure (EMERGE). He is former president of the International Union of Materials Research Society (IUMRS), member of the Scientific Council of the European Research Council, member of the Advisory Council of DG Prosperity within the framework of the European Programme Horizon (2014–2016).

Hugo Águas associate professor at the Materials Science Department of FCT-NOVA and photovoltaics research group leader at CEMOP-UNINOVA. He received his Ph.D. in 2005 in optoelectronics engineering. He has coordinated six national projects and was responsible for several national and international projects, including the H2020 Project APOLO. He has a publication record of more than 190 publications recorded by WoK. With more than 3800 ciations in WoK and an H-index of 38, his current research interest list includes the fields of thin-film deposition and silicon materials for photovoltaic devices and optical sensors; nanomaterials processing; biosensors; microfluidics; and SERS.

Manuel J. Mendes has been involved in 40 projects in energy-related areas while working in USA (2005–08), Spain (2008–12), Italy (2012–14), and Portugal (2014-present). At CENIMAT-i3N he has been PI or institution responsible of 14 projects related with photonic-enhanced solar cells, quantum-structured semiconductors, building-integrated photovoltaics (BIPV), and solar fuels. In 2023, an ERC Consolidator Grant was awarded to his project X-STREAM. He has acted as reviewer for >40 journals, is author of >70 peer-reviewed publications, and coinventor of 2 US Patents. He was awarded with two Marie Curie experienced-research Fellowships as well as other 10 prestigious scientific honours.